

VISIBLE SPECTRUM BASED NON-CONTACT DETECTION AND
CHARACTERIZATION OF BLOOD WAVE SIGNAL DYNAMICS AND
APPLICATIONS IN STRESS DETECTION

by

Balvinder Kaur
A Dissertation
Submitted to
Graduate Faculty
of
George Mason University
in Partial Fulfillment of
The Requirements for the Degree
of
Doctor of Philosophy
Electrical and Computer Engineering

Committee:

V. Ikonomidou

Dr. Vasiliki N. Ikonomidou, Dissertation
Director

A. Manitus

Dr. Andre Manitus, Committee Member

J. K. Nelson

Dr. Jill K. Nelson, Committee Member

G. Cook

Dr. Gerald Cook, Committee Member

B. Familoni

Dr. Babajide Familoni, Committee Member

M. H. Hayes

Dr. Monson H. Hayes, Department Chair

K. Ball

Dr. Kenneth Ball, Dean, Volgenau School of
Engineering

Date:

April 13, 2016

Spring Semester 2016
George Mason University
Fairfax, VA

Visible Spectrum Based Non-Contact Detection and Characterization of Blood Wave
Signal Dynamics and Applications in Stress Detection

A Dissertation submitted in partial fulfillment of the requirements for the degree of
Doctor of Philosophy at George Mason University

By

Balvinder Kaur
Master of Science
George Mason University, 2012
Bachelor of Science
George Mason University, 1999

Dissertation Director: Vasiliki N. Ikonomidou, Assistant Professor
Department of Electrical and Computer Engineering

Spring Semester 2016
George Mason University
Fairfax, VA

Copyright © 2016 by Balvinder Kaur
All Rights Reserved

DEDICATION

I dedicate this thesis work to my beloved and supportive husband Harpreet Singh and our intellectual and affectionate son Taaren Veer Singh who encouraged and supported me throughout this journey of the doctorate degree program. Thanks are due to my father-in-law Mr. Jagjit Singh, mother-in-law, Mrs. Narinder Kaur, my father, Mr. Balbir Singh, and my mother, Mrs. Surjit Kaur, whose support and interest made the work much easier.

ACKNOWLEDGEMENTS

Dr. Vasiliki N. Ikonomidou, my advisor, provided me invaluable help, guidance, and support throughout my doctorate research. Her knowledge, flexibility, patience, kindness, mentoring, and friendship were vital to my success. I also gratefully thank and acknowledge my committee members, Dr. Andre Manitiu, Dr. Babajide O. Familoni, Dr. Dr. Gerald Cook, and Jill K. Nelson for their help, support, and guidance. Very special thanks are owed to my chain of command for encouraging and supporting higher education starting with Dr. Donald A. Reago, Richard A. Nabors, Mr. William S. Jarvis, Dr. Dr. Keith A. Krapels, Ms. Susan M. Harkrider, Dr. Joseph J Durek, Mr. Jonathan G. Hixson, my colleges and friends for guiding and supporting me throughout my Doctorate program. Finally, I want to thank Dr. James A. Hutchinson for being my mentor, associate, colleague, friend, and an individual who inspired me to find a visible spectrum based solution for remote stress detection.

TABLE OF CONTENTS

	Page
LIST OF ACRONYMS _____	viii
LIST OF TABLES _____	xi
LIST OF FIGURES _____	xii
ABSTRACT _____	xvi
CHAPTER ONE: INTRODUCTION _____	1
Problem Statement _____	2
Proposed Solution _____	2
Significance _____	2
Objectives _____	3
Innovation _____	4
Organization of Dissertation _____	5
CHAPTER TWO: BACKGROUND AND MOTIVATION _____	7
Heart Rate Variability (HRV) Analysis based on Contact Sensing _____	8
Obtaining More Accurate RR-Intervals by Noise Removal _____	8
Heart Rate Variability Analysis for Stress Detection _____	10
Heartbeat Signal Detection based on Non-Contact Sensing _____	12
Pulse Transit Time (PTT) and Its Relationship to Blood Pressure _____	16
Physiological Stress Detection based on Non-Contact Sensing _____	19
Motivation _____	21
CHAPTER THREE: CHARACTERIZE REMOTELY DETECTED BLOOD WAVE (BW) SIGNAL AND GENERATE RR-INTERVAL SIGNAL _____	24
Introduction _____	24
Materials and Methods _____	25
Experimental Setup _____	26
Experiments _____	27
Remote Blood Wave (BW) Signal Detection _____	29
Factors Impacting a Remote BW Signal _____	36
RR-Interval Estimation from BW Signals _____	38

Results	51
Discussion	55
CHAPTER FOUR: REMOTE MEASUREMENTS OF HEART RATE VARIABILITY AND ITS USE FOR STRESS DETECTION	57
Introduction	57
Materials and Methods	59
Experiments	60
Prepare Data for HRV Analysis	62
Determine HRV-Driven Features for Stress Detection	63
Classification for Stress Detection	64
Confidence Metrics to Quantify Algorithm Performance	68
Results	69
Stress Detection Results using ECG Data	71
Stress Detection Results using VIS Data	74
Repeatable Stress Detection using VIS Data	77
Improvements in Stress Detection Results	79
Discussion	81
CHAPTER FIVE: REMOTE MEASUREMENTS OF DIFFERENTIAL PULSE TRANSIT TIME AND ITS USE FOR STRESS DETECTION	84
Introduction	84
Materials and Methods	85
Experiments	85
Remote Blood Wave (BW) Signal Detection	88
Differential Pulse Transit Time (dPTT) Computations	88
Remote Stress Detection using dPTT	90
Results	91
Discussion	96
CHAPTER SIX: ROBUSTNESS OF REMOTE STRESS DETECTION FROM VISIBLE SPECTRUM VIDEOS	98
Introduction	98
Methods and materials	100
Remote Blood Wave (BW) Detection	100
Remote Differential Pulse Transit Time (dPTT) Estimation	101
Remote Heart rate variability (HRV) Feature Generation	101
Simulated Data	102
Robustness of the BW Signal	103
Robustness of the dPTT Metric	104
Robustness of the HRV-driven Features	104
Results	106

Discussion and Conclusions _____	112
CHAPTER SEVEN: CONCLUSIONS AND FINAL COMMENTS _____	115
Conclusions _____	115
Impact of Dissertation _____	119
Future Research Areas _____	120
Final Remarks _____	121
REFERENCES _____	122

LIST OF ACRONYMS

AAMI	Advancement of Medical Instrumentation
ANS	Autonomic Nervous System
ASRT	Affective Stress Response Test
AUC	Area Under the Curve
BDC	Blind Deconvolution
BPL	Back Palm Left
BPM	Back Palm Middle
BPR	Back Palm Right
BW	Blood Wave
CF	Curve Fitting
CH	Chin
CL	Cheek Left
CR	Cheek Right
DC	Direct Current
dPTT	Differential Pulse Transit Time
DSLR	Digital Single-Lens Reflex
ECG	Electrocardiograph or Electrocardiogram
FFT	Fast Fourier Transform
FL	Forehead Left
FM	Forehead Middle
FN	False Negative
FP	False Positive
FPL	Front Palm Left

FPM	Front Palm Middle
FPR	Front Palm Right
FR	Forehead Right
FSVM	Fuzzy Support Vector Machine
GT	Ground Truth
GUI	Graphical User Interphase
HB	Heartbeat
HF	High Frequency
HPF	High Pass Filter
HRV	Heart Rate Variability
HRVAS	Heart Rate Variability Analysis Software
HRVTi	Heart Rate Variability Triangular Index
ICA	Independent Component Analysis
IR	Infrared
IRB	Internal Review Board
LDA	Linear Discriminant Analysis
LDV	Laser Doppler Vibrometer
LF	Low Frequency
LFHF	Low Frequency over High Frequency
LMS	Least Mean Squares
LNR	Light to Noise Ratio
LPF	Low Pass Filter
LR	Logistic Regression
LS	Least Squares
LWIR	Long-Wave Infrared
MSE	Mean Square Error
MST	Modified Stroop Test
MWIR	Mid-Wave Infrared
nHF	Normalized to Total Power High Frequency
PCA	Principal Component Analysis

PD	Probability of Detection
PDM	Principal Dynamic Mode
peakHF	Peak High Frequency
pHF	Percentage of the Sum of Average High Frequency
pLF	Percentage of the Sum of Average Low Frequency
PPG	Pulseplethesmograph
PTSD	Post-Traumatic Stress Disorder
PTT	Pulse Transit Time
pVLF	Peak Very Low Frequency
PWTT	Pulse Wave Transfer Time
QRS	Peaks in ECG Cycle
RGB	Red, Green, and Blue
RMSE	Root Mean Square Error
ROC	Receiver Operating Characteristic
ROI	Region-of-Interest
RR-Interval	Time interval between successive R-peaks in ECG signal
SCWT	Stroop Color-Word Test
SDNNi	Standard Deviation of Inter Beat Intervals Index
SE	Shannon Entropy
SNR	Signal-to-Noise Ratio
SVD	Singular Value Decomposition
SWIR	Short-Wave Infrared
TBI	Traumatic Brain Injury
TN	True Negative
TP	True Positive
TSST	Trier Social Stress Test
VIS	Visible Spectrum
ZC	Zero Crossings

LIST OF TABLES

Table	Page
Table 1: A list of task relevant HRV-driven features for stress detection.	70
Table 2: Area under the curve for all four cases using LR and LDA	73
Table 3: Area under the curve for high and mild stress detection using LR and LDA.....	76
Table 4: The truth tables with stress detection results from remote HRV (12 subjects, experiment 2 with zero crossing based detected peak).	80
Table 5: The truth tables with stress detection results from remote HRV (15 subjects, experiment 3 with blind deconvolution based detected peaks and HRV baseline correction).	80
Table 6: A list of significant HRV-driven features that can be used for stress detection.	109

LIST OF FIGURES

Figure	Page
Figure 1: Experimental setup with controlled illumination source (CFL).....	27
Figure 2: Subject positions during experiments with their hand leaning against head with: palm facing camera (left), and it back facing camera (right).....	28
Figure 3: The effects of multipath within an ROI (left) on skin reflectivity signals in green band (right).	31
Figure 4: An example of plots with PCA generated first principal component from each band indicating periodicity similar to a cardiac signal: Red (top), Green (middle), and Blue (bottom).33	
Figure 5: Sample skin reflectivity signals after denoising (PCA) and source selection (ICA) with the highest SNR in the IC2.	35
Figure 6: A subject with the body locations that were investigated to identify the best candidate areas with the highest SNR for the BW signal.....	37
Figure 7: Typical BW signal computed from the human skin reflectivity after the cardiac pulse (ECG) passes through the human body (low-pass filter).	38
Figure 8: ZC based estimated periods (blue spikes) on a typical BW signal and a false period (red arrow).....	40
Figure 9: An example with CF algorithm generated plots with BW signal (black), initial peaks (green), estimated BW signal (red), and final peaks (blue).	43
Figure 10: An example with estimated input (left-red curve) and impulse response (right-red curve)	

with L0 penalty.	48
Figure 11: An example of the plot with MSE between BW signal and the estimated BW signal showing the convergence of the BDC algorithm using L0 penalty.	48
Figure 12: An example with estimated input (left-red curve) and impulse response (right-red curve) with L1 penalty.	49
Figure 13: An example with estimated input (left-red curve) and impulse response (right-red curve) with L2 penalty.	49
Figure 14: SNR measurements of BW signal from 12 different body locations indicating the highest SNR for the palm and forehead location.....	51
Figure 15: Plots showing a lower average SNR values for the darker skin color.....	52
Figure 16: Plot showing the bars with absolute normalized error between the GT and the three algorithms (ZC, CF, and BDC).....	53
Figure 17: An example with the VIS and GT peaks (top) and RR-interval signals (bottom) showing a close relationship between the two.....	54
Figure 18: HRVAS GUI used to compute HRV-driven features from RR-interval signals for both normal and stress states.....	64
Figure 19: An example of generation and usage of Logistic Regression based model for classification of normal (left) and stress (right) states.	66
Figure 20: An example of data (two classes) distribution with two features only (left); LDA generated projection vector to maximize the inter-class separation and minimize intra-class separation (right).....	68
Figure 21: Box and whisker plots showing the distribution of the relevant features (from 12 subjects) for the normal and stress states.	71
Figure 22: ROC curves for stress detection using logistic regression and LDA comparing: (1) rest	

with scale, (2) rest with test, (3) rest with announcement, and (4) rest with talk.	72
Figure 23: Bar charts with sensitivity, specificity, precision, and accuracy metrics for logistic regression classification for the four comparison cases of Figure 22.	73
Figure 24: ROC curves for stress detection using logistic regression and LDA comparing: Normal with Stress1 and (2) Normal with stress2.	75
Figure 25: Bar charts with sensitivity, specificity, precision, and accuracy metrics for logistic regression classification for the two comparison cases of Figure 24.	76
Figure 26: ROC curves for stress detection using LR comparing states: Normal with stress1 (left) and Normal with stress2 (right).	78
Figure 27: Bar charts with sensitivity, specificity, precision, and accuracy metrics for LR classification for the two comparison cases of Figure 26.	78
Figure 28: ROC curves for stress detection using LR with improved algorithms (red) and standard algorithms (green), comparing states: Normal with stress1 (left) and Normal with stress2 (right).	79
Figure 29: Subject positions during experiments with their hand leaning against head with and palm facing camera.	86
Figure 30: Typical averaged heart beat signals and their time shift between forehead (red dots) and palm (blue stars).	90
Figure 31: Average dPTT values (Experiment one, first normal state, 15 subjects).	92
Figure 32: Average dPPT value distribution for the normal and stress states using data from experiment one (15 subjects).	93
Figure 33: Average dPPT value distribution for the normal and stress states using data from experiment two (12 subjects).	94
Figure 34: Paired plots showing the dPTT values from all subjects for the three normal and three	

stress states, and their relationship between states under the second experiment.....	95
Figure 35: Paired plots showing the dPTT values from all subjects for the three normal and three stress states, and their relationship between states under the third experiment.	95
Figure 36: An example with the flickering noise (1 Hz): simulated BW (black), flickering noise (green), and noise-modulated BW (red) signals.	103
Figure 37: The plots showing the absolute error between the peaks of the BW and the noise-modulated BW signals over a range of noise LNR values due to respiration motion.	107
Figure 38: The plots showing the absolute error between the peaks of the BW and the noise-modulated BW signals over a range of noise LNR values due to light flickering.....	107
Figure 39: Plot showing the normalized absolute difference between the normal and stressed states for the identified relevant HRV-driven features, with red stars showing mid-point value and black star with below the mid-point value for each feature.....	109
Figure 40: The box and whisker plots of relevant HRV-driven features with the absolute normal difference between the simulated and noise-modulated (respiration noise) signals with the thresholds for each (red and black horizontal dotted line).....	111
Figure 41: The box and whisker plots of relevant HRV-driven features with the absolute normal difference between the simulated and noise-modulated (flickering noise) signals with the thresholds for each (red and black horizontal dotted line).	112

ABSTRACT

VISIBLE SPECTRUM BASED NON-CONTACT DETECTION AND CHARACTERIZATION OF BLOOD WAVE SIGNAL DYNAMICS AND APPLICATIONS IN STRESS DETECTION

Balvinder Kaur, Ph.D.

George Mason University, 2016

Dissertation Director: Dr. Vasiliki N. Ikonomidou

Stress is a major health concern that not only compromises our quality of life, but also affects our health and well-being. Despite its importance, our ability to objectively detect and quantify stress in a real-time, non-invasive manner is limited. This capability would have a wide variety of medical, military, and security applications. Under the dissertation research, we have developed a pipeline of image and signal processing algorithms for such a capability, which includes remote blood wave (BW) signal detection based on minor color intensity fluctuations in visible spectrum videos of the human skin during the cardiac cycle, and physiological stress measurements based on the temporal variability in these remotely detected cardiac signals.

To detect BW signals reliably, we applied Principal Component Analysis (PCA) for noise reduction and Independent Component Analysis (ICA) algorithms for source selection. A blind deconvolution (BDC) algorithm based on least squares (LS)

minimization was then applied to the BW signals to determine peaks, which were then used to detect reliable RR-intervals, the intervals between the adjacent BW signal peaks. The series of RR-interval values was then used to derive heart rate variability (HRV) features in both temporal and frequency domain. The stress significant features were then identified based on the paired t-test, which were then used with logistic regression (LR) classifier to discriminate stress states from the normal ones. In addition, we have defined a new metric called differential pulse transit time (dPTT) as the difference in arrival time of BW signal at two separate distal locations, and have demonstrated its potential use for stress detection.

The developed algorithms were tested against the human subject data collected under two physiological conditions using the modified Trier Social Stress Test (TSST) and the Affective Stress Response Test (ASRT). This dissertation presents the developed algorithms and the stress detection results. This research provides a proof that the variability in remotely-acquired BW signals can be used for stress (high and mild) detection with 92% likelihood of being correct, and a guide for further development of a real-time remote stress detection system based on remote HRV and dPTT.

CHAPTER ONE: INTRODUCTION

Stress is a major health concern that not only compromises our quality of life, but also affects our health and well-being. Despite its importance, our ability to objectively detect and quantify stress in a real-time, non-invasive manner is very limited. Through the means of our dissertation research, we contribute to such a capability, by combining remote heart beat detection through a visible spectrum camera and heart rate variability analysis in order to develop a compact, low-cost and possibly covert system for detecting stress.

The research presented in this dissertation builds on two well-studied fields: remote detection of cardiac pulse signals using skin color variations in visible spectrum video [1]–[6], and stress detection on the basis of heart rate variability (HRV) [1], [7]–[11] and pulse transit time (PTT) [12]–[15]. In this research work, we have demonstrated that it is possible to detect acute stress in a non-contact manner based on variability in the remotely acquired cardiac pulse signals. Remote cardiac pulse detection has been shown to be highly correlated with ground truth (ECG signal) measurements and, as such, enables the development of a remote stress detection method based on HRV and a new novel metric called differential pulse transit time (dPTT).

Problem Statement

Stress is a major health concern that not only compromises our quality of life, but also affects our health and well-being. Despite its importance, our ability to objectively detect and quantify stress in a real-time, non-invasive manner is very limited. This capability would have a wide variety of medical, military, and security applications.

Proposed Solution

We developed a pipeline of image and signal processing algorithms for a remote stress detection system, which includes remote blood wave (BW) detection based on visible spectrum videos, and physiological stress detection based the variability in the remotely detected cardiac signals. The pipeline includes algorithms for: noise-robust RR-interval extraction, stress detection based on remote HRV-driven features, differential pulse transit time (dPTT) measurements based on the difference in arrival of a BW signal at two separate distal body locations, and stress detection based on dPTT.

Significance

A quantifiable technique to measure stress states without introducing additional stress due to the use of contact sensors will be valuable to many applications such as: in the medical field, it could help identify stressors in patients with anxiety disorders, supporting diagnosis and treatment; in the security field, it could be used for screening interviewees with the purpose of deception detection; in a time critical situation, in the military field, it may be used for treating wounded warriors in-transit or during long-term monitoring; in other time-critical situations (e.g., during an event, in-flight, etc.) it may

alert the control center to an emergency without the need for any additional communication from an operator. Such remote stress detection based on visible spectrum recordings will enable a solution through the use of standard day cameras which are easy to use, inexpensive, non-invasive, light weight, and accessible.

Objectives

The main objective of this research was to develop a pipeline of algorithms for a visible spectrum based remote stress detection system. The developed algorithms would facilitate the non-contact measurement of BW signals and dPTT, and stress detection based on their variability. This research had three aims: 1) to characterize remotely detected BW signals and generate noise-robust RR-interval signals, 2) to develop noise-robust stress detection algorithms based on remote HRV, and 3) to determine dPTT and investigate its value for stress detection.

For aim one, we: 1) designed controlled experiments and collected data on human subjects under approved protocols, 2) mitigated recording noise by collecting human skin reflectivity data under controlled lighting and relatively motionless conditions, 3) mitigated pulse broadening and phase noise by applying principal components analysis (PCA) [16], [17], 4) mitigated composite signal effects by applying independent component analysis (ICA) [18] and determined BW signals, 5) characterized the BW signals for optimal skin locations and colors, and 6) determined RR-interval timings by applying a blind deconvolution (BDC) algorithm using penalized regression [19].

Under aim two, we: 1) identified relevant BW-driven features, 2) identified robust and relevant HRV-driven features for stress detection, 3) identified classification algorithms to distinguish stress states from the normal ones, 4) determined metrics to quantify results and generated ROC curves, and 5) applied the developed algorithms to the facial and palm video recordings in order to detect stress states.

Finally, under aim three, we: 1) estimated dPTT based on the relative time shift between the remotely acquired BW signals in two distal body locations, 2) investigated the value of dPTT for stress detection, and 3) investigated the repeatability of the dPTT metric for stress detection.

Innovation

The main novelty of our research is that, to the best of our knowledge, this is the first study demonstrating that the variability analysis of cardiac pulse acquired in visible spectrum can be used for remote stress detection. In order to do so, it was necessary to develop a pipeline of image and signal processing methods. Therefore, the novelty was in the development of methods for noise-robust RR-interval extraction, stress detection based on remote HRV-driven features, dPTT measurements based on the difference in arrival of a BW signal at two distal body locations, and stress detection based on dPTT. Unlike ECG signals, BW signals, which are the basis for the remote stress detection system, are more complex because they are a mixture of signals, such as heartbeat, respiration, motion, etc., and also are susceptible to various types of noise. In order to obtain clean BW signals with peaks that represent ECG R-peaks closely, we have developed algorithms which involved

phase noise removal using PCA, source selection using ICA, and peak detection using BDC.

The novelty within this research is in the development of methods for noise-robust RR-interval extraction, stress detection based on remote HRV-driven features, and dPTT measurement and its use for stress detection and measurement. To increase the confidence in the remote stress detection system, BW signals were characterized for various skin colors and body locations, and optimal body locations were identified where the BW signal could be acquired with high signal-to-noise (SNR) values. In addition, the effects of a commonly seen multiplicative noise introduced by human motion due to respiration and light flickering on BW signals was studied to understand any limitations introduced.

The algorithms for stress detection based on remote BW signals and their variability analyses facilitate repeatable and reliable measurements for stimulus response, under controlled environment and daylight conditions for many medical and security applications.

Organization of Dissertation

The balance of this dissertation is broken up into six chapters. Chapter Two covers the background literature on all of the topics covered in the dissertation and their relevance to our problem. Chapters Three through Six cover the introduction, materials and methods, results, and discussion for the topics covered. Chapter Three discusses our novel approaches for remote BW signal detection and clean RR-interval generation based on the BDC algorithm. Chapter Four discusses our approach of identifying HRV-driven features

for stress detection and developing classifiers for HRV-based remote stress detection. Chapter Five includes a novel method that we have developed to determine dPTT employing the remotely measured BW signals at two separate distal locations, and its use for remote stress detection. Chapter Six includes the studies we have conducted to show the robustness of our remote stress detection system against multiplicative noise. Chapter Seven presents the summary of our research with the conclusions, impact of dissertation, future research areas, and final remarks.

CHAPTER TWO: BACKGROUND AND MOTIVATION

Due to the importance of stress both in everyday life activities and in response to pathological conditions, many attempts have been made to monitor stress in real-time [20], [21]. Most of these attempts target activities regulated by the autonomic nervous system (ANS) as indicators of stress. The ANS is responsible for the fight-or-flight response, which is our body's main physiological response to stress [22]. This is the part of the nervous system that controls involuntary actions such as the heartbeat, vasomotor, and sweat gland activity. Traditionally, heart rate variability (HRV) [23]–[26], sweat gland activity [27]–[29], and blood pressure [29]–[32] have been explored as stress markers along with more invasive markers, such as cortisol levels [33]–[35]. However, most of these systems require contact sensors, which may introduce additional stress to the subject, and are not appropriate if a covert system is desired. A method to track physiological stress remotely in a non-invasive manner will be advantageous to many applications (discussed in the Introduction chapter).

In this chapter we discuss the current state-of-the-art in three main areas applicable to stress detection: 1) cardiac pulse measurement using contact sensors and its variability analysis for stress detection, 2) cardiac pulse measurement using non-contact sensors, and 3) pulse transit time (PTT), the time that is required for the blood pressure wave (BW) to

cover the distance from the heart to a defined remote location in the body and its relationship with blood pressure.

Heart Rate Variability (HRV) Analysis based on Contact Sensing

Heart rate variability (HRV) can be an important indicator of several conditions that affect the autonomic nervous system, including traumatic brain injury, post-traumatic stress disorder and peripheral neuropathy [7], [9]–[11]. For many decades, contact sensor systems such as electrocardiograph [8], [10], [36]–[39] [40] and pulseplethysmograph (PPG) [41]–[43], [3], [44] have been used to measure heartbeat signals for the purpose of variability analysis. These signals are then processed further to determine RR-intervals, the interval from the R-peak of one QRS complex to the R-peak of the next QRS complex (in ECG signal). An RR-interval signal (a series of RR-intervals) is used to determine HRV-driven features (e.g., average, standard deviation, maximum, minimum, etc.), which are then used for discriminating one physiological condition from another. Two major parts of HRV analysis involve clean RR-interval determination and then HRV analysis for a specific condition detection.

Obtaining More Accurate RR-Intervals by Noise Removal

Noise in the BW signal can significantly complicate extraction of the desired signals. In order to obtain clean RR-interval signal for variability analysis, many researchers have designed denoising algorithms to remove artifacts due to the physical motion of the subject's body during measurement [45]–[51].

Lee et al. [51] developed noise reduction algorithms for PPG signals using a particle filter with 500 particles and have generated RR-interval signals. These algorithms were tested against an experimental data, and noise reduction of 12.7% for stationary and 10.9% for the non-stationary (walking) conditions was achieved. Zhu et al. [45] developed a method for sparse signal denoising based on compressive sensing. Shaoxiang et al. developed a framework for signal denoising based on wavelet packet hidden Markov models [46]. Reddy et al. [47] developed a method to remove motion artifacts from corrupted PPG signals by applying Fourier series analysis on a cycle-by-cycle basis. Following their method, researchers achieved data compression by a factor of 12 which results in motion artifact reduction by 23 dB. Durand et al. [48] developed a method for denoising signals by applying the wavelet transform method, which helped removing Gibbs phenomenon effects (the sharp discontinuities), while preserving the other structures. Their results showed an improvement in the SNR values of the signals and reduction in visual artifacts. Yousefi et al. [49] developed a real-time, two-stage normalized least mean square adaptive noise canceller algorithm, which removed the motion artifacts introduced by various sources such as tissue effects and venous blood changes during body movements. The results demonstrated a correlation of 0.98 for HR and 0.7 for SpO₂ between the measurements from reference sensors and the developed algorithm output. Selvaraj et al. [50] introduced a statistical approach to overcome the motion and noise artifacts (MNA) in PPG signals based on the computation of kurtosis and Shannon Entropy (SE). The accuracy of the fusion of kurtosis and SE metrics for the artifact removal was 99.0%, 94.8% and 93.3% for simultaneously recorded ear, finger and forehead PPGs, respectively,

obtained in a clinical setting. This body of work has made significant advances in the important area of obtaining clean RR-intervals through noise removal.

Heart Rate Variability Analysis for Stress Detection

Many researches [8], [10], [36], [37], [39], [40], [44], [52]–[54] have used the variability in PPG and ECG signals for discriminating between two conditions (e.g., healthy or sick, normal or stressed). While the HRV is usually detected as low- and ultra-low-frequency activity in the RR-interval time series, time domain techniques have been developed that overcome the stationary assumption of the Fourier transform analysis, allowing better identification of both the presence of stress and stressors [8], [10], [36], [38], [54].

In one study, Verma et al. [39] showed that the HRV-driven PPG-based features such as low frequency (LF), high frequency (HF) and ratio of LF over HF (LFHF) can be used to quantify parasympathetic influences and sympathovagal balance. In another study, Lu et al. [44] showed that variability in PPG signals can be used to discriminate between two physiological conditions. Their viability analysis showed that LFHF from both ECG and PPG driven features had a high significance ($p < 0.05$), which helped with distinguishing two positions (upright and supine). Leschyshyn et al. [40] presented HRV as a periodically correlated stochastic process. They used Neyman-Pearson Criterion, a coherent method for digital spectrum analysis to compute characteristics of non-stationarity in HRV, and claim that the method can potentially be used for discriminating two physiological conditions. Luo et al. [52] conducted a variability analysis using PPG

data from 40 patients and identified that healthy patients can be discriminated from hypertensive patients using pulse wave transfer time(PWTT).

Lin et al. [38] conducted a study in which variability in ECG recordings was analyzed for two conditions (resting state and during a driver-vehicle simulation). Their results showed that the Lyapunov exponents has a reduction in signal amplitude with increasing stress level. Boonnithi et al. [10] studied six subjects under normal and stressed conditions and reported that the variability in mean RR-intervals, mean heart rate, low frequency power, and low frequency/high frequency power ratio have potential as features for distinguishing stressed subjects from non-stressed subjects. Kim et al. [36] studied the effect of long-term variations in HRV on chronic stress levels. Their analysis on ECG recordings from 23 subjects demonstrated that the high stress group shows significantly less HRV as compared to the low stress group. Wu et al. [53] developed a system to extract HRV features from the ECG-driven signals for stress analysis and demonstrated that short-term visual stress affects the HRV, but in the long-term stress decreases the HRV as the ANS adapts to the environment. Choi et al. [55] developed an approach to detect mental stress using ECG recordings. Their variability analysis on 3 subjects showed that the Principal Dynamic Mode (PDM) features are more stable and less subject-dependent as compared to the spectral features and therefore can reliably be used for stress detection. Sung and Pentland [8] proved that HRV can be a useful metric for stress and lie detection. Their HRV analysis on the experimental ECG recordings collected during a poker game was able to detect stress conditions with 82% accuracy. Kaur et al. [24] demonstrated that

the HRV in ECG recordings can be used for multiple levels of stress detection using both logistic regression (LR) and linear discriminant analysis (LDA) classifiers.

Currently, the primary method of deriving the HRV signal is to acquire the ECG signal, apply appropriate QRS detection algorithms to locate the R wave and its peak, find the RR-intervals, and perform suitable interpolation and resampling to produce a uniformly sampled tachogram. This process sometimes result in errors in the HRV signal due to drift, electromagnetic and biologic interference, and the complex morphology of the ECG signal. Based on the literature, PPG signals that are similar to VIS spectrum based signals [56] have the potential to eliminate the problems with the ECG signal to derive the HRV features and therefore represent a potentially practical replacement for ECG-derived HRV signals in ambulatory cardiac monitoring in individuals.

The body of research conducted in stress detection based on the variability in the ECG and PPG signals encouraged us to explore the use of variability in the remotely measured cardiac signal (called the non-contact HRV) for stress detection. In addition, the experimental designs adapted by various groups to induce physiological stress gave us insight to the design of effective experiments.

Heartbeat Signal Detection based on Non-Contact Sensing

Reliable non-contact sensing of heartbeat and potential stress indicators would be a major advance in the practical applicability of stress detection methodologies. In the past, cardiac signal measurements have usually been made using contact sensors. However, recent work has shown that the cardiac signal can be obtained actively using

Laser Doppler Vibrometer (LDV) and passively using thermal (IR) and visible (VIS) cameras. Several remote cardiac pulse detection methods are discussed in the subsequent paragraphs of this section.

For example, Desjardins et al. [57] developed a method for detecting the blood pulse waveform based on skin vibration measurements at the carotid artery made with an LDV. The group was able to identify important events in the cardiac cycle, such as heart rate, the timing of the peak systole, the left ventricular ejection time and the aortic valve closure. In another study, Byrd et al. [58] demonstrated that vibration measurements at various skin and non-skin areas (e.g., clothing) made with an LDV can be used to determine cardiac signal from a distance.

Garbey et al. [59] conducted a study to determine cardiac pulse rate from thermal imagery collected in a controlled environment. They used the signals emitted from recognized vessels to determine cardiac pulse rate. It was the heat signature due to blood flow in the vessels that was measured and tracked over a set of frames to construct signals. Then the Fast Fourier Transformation (FFT) was performed on the measured signals from 34 subjects to compute pulse rate, which demonstrated positive results for pulse detection in thermal imagery.

Many researchers have shown that the cardiac pulse can be obtained from measurements of minor fluctuations in intensity (skin reflectivity) recorded using VIS spectrum RGB video [41], [41]–[43], [5], [60]. The mechanism behind this is the change in skin reflectivity at specific wavelengths during the cardiac cycle. As the blood pressure

wave corresponding to cardiac systole arrives in the skin arterioles and capillaries, the diameters of the arterioles and some capillaries increase, leading to a temporal peak in blood concentration is observed. Oxy- and deoxyhemoglobin, two main blood components influence light absorption at the skin, due to significant absorption peaks in the Soret (~400nm to ~450 nm, corresponding to blue/violet) and q-bands (~500nm to 600nm, spanning green and yellow) [61]. Based on the phenomenon of time varying light absorption due to the oxy-hemoglobin content, spectral ranges in the q-bands can be used for cardiovascular activity measurements in a non-contact manner [11]. Changes in light absorption in the Soret region are quite small, as light in this band penetrates to the arterioles to a much smaller degree.

In addition to identifying the spectral ranges that can help with remote measurements of cardiac pulse activity, it was essential to understand the source of variable light absorption. Purves et al. [62] have studied the human blood circulatory system and have measured blood pressure, blood velocity and the area subtended by blood vessels at various levels (from arteries to veins). The arteries have the maximum hemodynamic pressure variation and would be the optimal areas-of-interest for remote heartbeat measurement. However, they are deep down in the tissue and the blood pressure wave causes a very small change in the skin reflectivity. Arterioles and capillaries cover a larger area close to the surface of skin as compared to the arteries and have relatively high hemodynamics as compared to the veins. These two properties of arterioles and capillaries make them the most likely candidates as the sources of the time varying skin reflectivity

[61]–[63]. Many researchers have been able to measure cardiac pulse remotely in the VIS spectrum and an overview of the relevant studies is presented below.

Wang et al. (Z. Wang et al. 2004b) at the Beckman Laser Institute found that PPG signals can be measured remotely ($> 1\text{m}$) using ambient light and a simple digital video camera. This group was able to quantify heart and respiration rates up to several harmonics. They have also shown that the PPG signals can be extracted using the red and blue bands, but that the green band works best because it corresponds to an absorption peak of oxy-hemoglobin. Many researchers [5], [6], [4] measured heart rate using a mobile phone camera. In their experiments, a subject's finger was placed directly on the camera lens to capture skin images, which were then processed to determine heartbeat. Poh et al. [42], [2] in a study at MIT have shown that heartbeat can be measured remotely using a standard iSight webcam. Their approach involved processing color video recordings (collected at 15Hz) of the human face using blind source separation of the color channels into independent components. When compared with the ECG data, a correlation coefficient of 0.98 ($p < 0.001$) during still conditions and 0.95 ($p < 0.001$) during motion conditions was achieved. Hsu et al. [41] have developed ICA based algorithms to measure cardiac pulse rate from visible spectrum based video recordings and chrominance-based features to improve the signal strength. Their data analysis showed a root mean square error (RMSE) value of 7.31 and a correlation coefficient of 0.77 in the scenario where the subjects were motionless and an RMSE value of 5.48 and correlation of 0.88 in the scenario where the subjects were moving. McDuff et al. [43] conducted a study to measure cardiac signals using a five band camera (digital single-lens reflex (DSLR) camera with a standard

Zuiko 50mm lens). Their results from experimental data collected on 10 participants under rest and stress conditions showed that the measurements from the orange band were highly correlated (0.92 with a p-Value < 0.01) with the contact PPG sensor measurements. Kwon et al. [3] developed an application for smartphone use to remotely measure heart rate. In order to extract cardiac pulse signals from the video recordings, ICA was applied to the raw traces from the RGB videos and the results show an error rate of 1.47% between the VIS and ECG heart rates.

Established success in remote cardiac pulse measurement utilizing visible spectrum cameras forms the basis for our research: remote stress detection based on variations in the remotely acquired skin reflectivity. We add to the existing research by designing a novel algorithm pipeline to measure the varying reflectivity with more accurate timing based on signal denoising to remove pulse broadening effects, source selection to determine BW signal [1], and blind-deconvolution to detect cardiac pulse peaks.

Pulse Transit Time (PTT) and Its Relationship to Blood Pressure

Pulse transit time (PTT) is a measure of blood pressure wave velocity. The PTT is loosely defined as the time it takes for the blood pressure wave to travel from the heart to a distal location. It is usually measured as the time difference between the R-wave of the ECG and the peak of a distally situated PPG [64]. Most recently, Teja [65] showed shown that the PTT can be computed using two PPG sensors placed at two distal body locations.

When explicitly measured, changes in PTT offers further insight into the ANS response. In literature, it is considered to be an indicator of blood pressure [14], [66]–[69].

PTT has been postulated that blood pressure can be measured indirectly from the pulse transit time, i.e., the time of the pulse arrival in different areas of the body. Geddes et al. [66] have shown good correlation of true pulse transit time with blood pressure in dogs; Obrist et al detected moderate correlations in humans, with errors imposed by myocardial sympathetic excitation and vascular processes [67]. More recently, Poon and Zhang examined 85 subjects, and in a total of 999 measurements found that the estimated systolic and diastolic blood pressure differed from the measured one by 0.6 ± 9.8 mmHg and 0.9 ± 5.6 mmHg respectively, comparable to the 5 ± 8 mmHg target levels of the Association for the Advancement of Medical Instrumentation (AAMI) [14]. As an application of the PTT measurement, Sahoo et al. [64] have designed a noninvasive cuff-less blood pressure and pulse rate estimation system based on PTT. Jeong et al. [70] postulated that PTT and derivatives of PPG and ECG signals can be used for assessing BP during exercise. Their methods were tested against ECG and PPG data from five participants collected over three days and a correlation of -0.959 was achieved between the PTT and the systolic blood pressure. Gribbin et al. [71] in one of their earliest works reported a linear relationship between the arterial transmural pressure and PTT, with correlation coefficients of over 0.9 and significance at the 0.001 level. In a follow-up work, they confirmed a strong linear relationship under different types of stressors [72].

Obrist et al. [67] observed a strong correlation between PTT and systolic (but not diastolic) blood pressure. Allen et al. [73] reported significant covariation between PTT and systolic BP, with the association being stronger in hypertensive patients. Recently, similar results have been reported by, among others, Schmalgemeier et al. [74], Gesche et

al. [68], Kim et al. [75] and Lass et al. [76]. More recently, Zheng et al. [12], [77] have proposed a wearable PTT-based system for BP monitoring, which they report to show good correlation and small error (2.4 ± 5.7 mmHg) for systolic BP estimation.

In our own preliminary work, we have shown that it is possible to remotely measure, from red, green and blue (RGB) video, PTT among various regions of the body, with the forehead and the palm giving the best signal to noise ratio. Measurement was performed by finding the position of the correlation peak between upsampled versions of the derived heartbeat signal from region of interests (ROIs) in these two areas. We were also able to show that pulse transit time measured in this manner shows a strong correlation with systolic blood pressure; however the correlation is strongly dependent on the individual.

The association with blood pressure, which is regulated by the ANS and has been related to mental stress [78], [79], makes PTT an attractive candidate for stress monitoring. A study conducted by Gil et al. [13] shows that the variability in PTT during sympathetic activity is much more significant as compared to the HRV and therefore can be a good metric for stress detection.

Blood pressure is a well-known stress marker; many studies have shown that change in blood pressure is correlated with stress during exercise [80], [81] and other cardiovascular related stresses [82], [83]. The association with blood pressure, which is regulated by the ANS and has been related to mental stress [78], [79], makes PTT an attractive candidate for stress monitoring. However, as PTT measurement requires the use

of both ECG and PPG, it cannot be used for non-contact, possibly covert, measurements. In order to overcome this, we explored the use of our newly developed metric, differential pulse transit time (dPTT) to detect physiological stress remotely (covered in Chapter Four).

Physiological Stress Detection based on Non-Contact Sensing

In these past works great progress has been made in the areas of physiological stress detection based on contact HRV analysis derived from ECG or PPG. However, a few researchers have looked into remote options of physiological stress detection using sensor modalities such as audio, thermal, and visible.

Using a visible camera, Bousefsaf et al. [84] showed that mental workload can be measured by monitoring changes in video frames of the face. To prove this, experimental videos collected on 12 subjects under the Stroop Color-Word Test (SCWT) using a webcam at 30Hz were processed using classical wavelets and 3rd order derivative analysis to determine features under the two physiological conditions and the features were then compared for stress detection. Those researchers have shown that the remotely acquired features correlate with the skin conductance.

Using thermal cameras, a few researchers have shown that physiological stress can be detected remotely by tracking heat signatures [45], [85] on targeted skin areas. In one example, Zhu et al. [45] developed a system to monitor thermal signatures of the forehead's cutaneous tissue for lie detection. To verify this, thermal data collected on 38 subjects under an interrogation for a mock crime scenario were processed to determine features on the forehead region and a success rate of 76.3% in deceptive state classification was

reported. In another example using a thermal camera (8-12 μm), Yuen et al. [85] developed algorithms to detect emotional and physical stress. Thermal videos of 9 subjects under two conditions (physical stimulus (running) and mental stimulus (emotional response)) were processed to determine features which were then used to identify the stress responses. In addition, researchers have found elevated temperature regions in the forehead forming patterns characteristic of the types of stressors, dependent on whether they are physical or emotional.

Using visible cameras, a few researchers have developed methods for stress detection based on changes in ocular signatures [86], [87]. Mokhayeri et al. [86] have demonstrated that mental stress can be detected based on soft computing techniques using ocular signatures. To demonstrate this, data samples collected on 60 healthy subjects between the ages of 22-28 under the SCWT were processed to generate ocular signatures, which were then analyzed to detect stress states using a fuzzy support vector machine (FSVM) classifier. Ren et al. [87] developed an approach to evaluate a computer user's affective state as he transitions from "relaxation" to "stress" states through processing the pupil diameter signals. Experimental pupil videos collected with a TOBII system on 30 individuals during the SCWT were denoised using wavelet and Kalman filtering, and then the features were used to identify stress states using a set of classification algorithms (e.g., Multilayer Perceptron, Naive Bayes, Random Forest, and JRip). An average accuracy of 83.16% was achieved with the Multilayer Perceptron and the Naive Bayes classifiers.

Although not a common approach, Soury et al. [88] developed a method for stress detection from audio signals. The group captured audio signals on 29 subjects using a

wireless lapel microphone under the Trier Social Stress Test (TSST). These audio signals were then processed to generate features under normal and stressed conditions, which were then classified using the support vector machine (SVM) classifier to achieve an accuracy of 71.9 %.

The studies in the areas of physiological stress detection using modalities such as: pore response in thermal imagery, ocular information in visible imagery, and speech information in audio, inspired us to explore cardiac response information (non-contact HRV and dPTT) in the visible spectrum for stress detection. In addition, the experiments that were used by these researchers to induce stress were the candidates that we considered while designing our experiments.

Motivation

Motivated by the research conducted in the areas of our interest, we investigated the problem of remote mental stress detection based on the variability in the cardiac response signals in imagery acquired with a low cost day camera. To fill the gaps in the existing research, this research effort had three aims: 1) characterize remotely detected BW signals and generate noise-robust RR-interval signals, 2) develop noise-robust stress detection algorithms based on remote HRV, and 3) determine dPTT from remotely acquired BW signals and investigate its value for stress detection.

Since the remote sensing of human cardiac response measurement for stress analysis is such a new field, limited research work had been done in the areas of generating cardiac pulse signals with high SNR values and the resultant less noisier RR-intervals.

Noise in the estimation of the RR-interval is the limitation in an attempt to apply stress detection methodology to the contactless scenario. Detecting less noisy RR-intervals in remotely acquired cardiac signals is a big deviation from the conventional, ECG-based analysis. While noise is certainly a consideration for conventional ECG analysis, measurements of the RR time series depends on our ability to identify the R-peaks in the BW signal and is critical for computing robust and relevant HRV-driven features. We have developed novel algorithms for 1) remote cardiac signal detection by employing PCA for denoising and ICA for BW signal detection and 2) clean RR-interval detection based on accurately detected peaks employing a blind deconvolution algorithm.

As prior PTT measurement required the use of contact sensors, it cannot be used for non-contact, possibly covert, measurements. In order to overcome this limitation, we merged the research conducted in the areas of remote heartbeat detection and PTT computation based cardiac response signals measured at two distal body locations, and determined a new metric called dPTT. dPTT corresponds to the time difference in the pulse arrival time at two distal body locations. It is believed that due to the different pathways, blood arrival time at two different body locations will be different which should help with remote dPTT computations.

In addition, this research merges the research conducted in the areas of remote cardiac pulse response detection in the visible spectrum and stress detection based on HRV analysis and develops methodologies for remote stress detection based on the variability in the remotely acquired BW signals (remote HRV). A video-based stress detection system will help with overcoming additional (potential) stress introduced by contact sensors and

will provide a discrete means of monitoring stress in individuals. It is the combination of these technologies that pose unique challenges such as the low SNR of the RR-time series (derived from series of intervals between subsequent heartbeats) obtainable through video-based BW signals, remote detection of HRV and dPTT, and their use for stress detection. Details of these challenges along with solutions are addressed in subsequent chapters.

CHAPTER THREE: CHARACTERIZE REMOTELY DETECTED BLOOD WAVE (BW) SIGNAL AND GENERATE RR-INTERVAL SIGNAL

Introduction

While recent advances have shown that it is possible to acquire a signal equivalent to the heartbeat from visual spectrum video recordings of the human skin [1], [42], [53], [5], [2], extracting the exact timing information, a process that for the ECG signal involves calculating the positions of the R-peaks of the cardiac waveform, poses several difficulties for the blood wave (BW) signal as it requires estimating the equivalent peak positions in the BW signal.. There are two main factors that contribute to it: pulse broadening, due to both the low-pass nature of the cardiovascular system and multipath propagation effects [89], [90]; and the presence of multiple peaks, due to both reflected waves and additive noise [91], [92] . To mitigate the effects of these two factors, we have developed novel methods that are discussed in this chapter.

These novel methods were developed to detect cardiac pulse (BW signal) from facial skin video recordings and to estimate BW signal peak positions, aiming at a close representation of the R-peaks of the ECG signal. The method to estimate BW signals involved signal denoising with principal component analysis (PCA) and then source selection with independent component analysis (ICA). The method to estimate BW signal

peak positions is a blind deconvolution (BDC) algorithm based on least squares minimization. To prove the efficacy of the developed algorithms, we compared the BDC algorithm's generated peaks with the ECG peaks by means of absolute normal error and standard deviation of the normal error. To show the improvements achieved with the BDC algorithm, we compared the BDC results with the results of our initial "zero crossing" and newly developed "filtered least mean squares (LMS)" minimization algorithms. As compared to the other algorithms, BDC algorithm achieved the lowest absolute normal error and the lowest standard deviation of the error. This work, performed under an IRB approved protocol, provides initial proof that blind deconvolution techniques can be used to estimate timing information of the cardiac signal closely related to the one obtained by traditional ECG. The results show promise for further use of the detected peaks for generating clean RR-intervals, and the resultant RR-interval signals for heart rate variability (HRV) analysis.

Materials and Methods

This chapter has two major goals related to algorithm development: the first is to estimate the cardiac pulse (BW signal) from facial video recordings employing PCA for noise reduction and ICA for source selection, and the second is to generate cleaner RR-interval signals based on BDC-detected BW signal peaks. In addition to the algorithm development, we characterize the remotely acquired BW signal for various skin colors and commonly visible body locations. The research in this chapter builds on the work

discussed in the background chapter, addressing important problems that arise when trying to address the noisy environment of video-based signal extraction.

Experimental Setup

Healthy volunteers, age 18-50 with no prior history of heart conditions, participated in the study after providing informed written consent. A Basler scA640-70gc visible 12-bit video camera (Basler AG, Ahrensburg, Germany) with a spatial resolution of 400x300, at 59.9 Hz, with a 16mm/f1.2 lens was used to capture facial videos under broadband illumination (compact fluorescent lamp) conditions. To capture human skin reflectivity in the visible spectrum under these conditions, the compact fluorescent lamp, which has a broad spectrum with peak in green band (~525nm) and low noise spikes was used as an illumination source. The camera was calibrated at an exposure time of 16.7 ms to acquire facial videos without saturating the images. The exposure time was determined based on the SNR values of the acquired pulse signals from test videos of facial skin. Figure 1 shows the experimental setup we used to collect human subject data under controlled conditions.

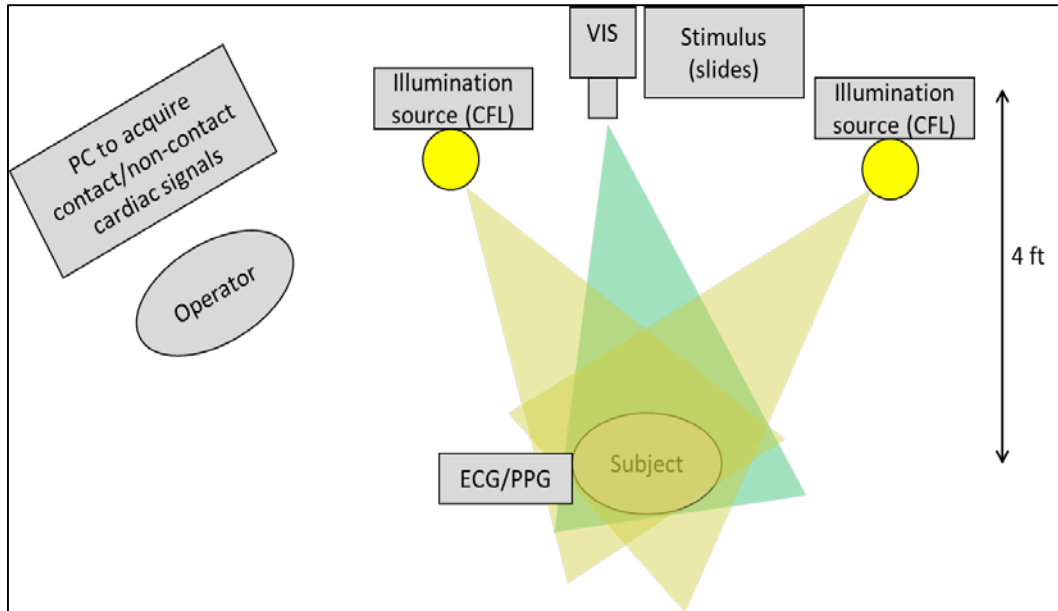


Figure 1: Experimental setup with controlled illumination source (CFL).

Experiments

We collected experimental data for two purposes: first, to design BW signal and peak detection algorithms, and second, to study the dependence of commonly visible body locations (e.g., face, palm, forehead, etc.) and skin colors (melanin) on SNR value of BW signals. During experiments, participants were asked to sit in a chair 5 feet away from the camera, with their head leaning against their hand and facing towards the camera. They were asked to sit as still as possible, and look at a computer screen in front of them, while we recorded their facial videos, and ground truth (ECG).

The first experiment was designed to capture body locations where skin is commonly visible such as forehead, cheeks, and the front and backside of the palm. The

purpose of this experiment was to identify locations where heartbeat signals can be captured with high SNR. During this experiment, participants were asked to view the computer screen with pleasant images (cats) for one minute each in two positions: with their head leaning against their hand with 1) their thumb under their chin, and palm facing towards the camera (Figure 2, left), and 2) with the back of their hand facing towards the camera (Figure 2, right).



Figure 2: Subject positions during experiments with their hand leaning against head with: palm facing camera (left), and it back facing camera (right).

The second experiment was designed to induce stress using the Affective Stress Response Test (ASRT). The purpose of this collection was to acquire facial videos and ECG data under two physiological states (normal and stressed), and use the collected data to design algorithms such as: BW signal detection, peak detection, and stress detection. Both visible and ECG data were collected on 15 volunteers, of which 5 had light skin color,

5 had medium skin color, and 5 had dark skin color. The skin variability in the collected data was used to study the effects of skin colors on the SNR of BW signals. During the experiment, participants were asked to view a series of alternating relaxing, and disturbing images on a computer screen with their head leaning against their hand and palm facing towards the camera (Figure 1, left). The stimuli presented on the computer screen were a series of photos, alternating between cat photos, and photos of dead people (chosen so as to make the participants feel uncomfortable). Two alternating sets of images were shown to capture human physiological responses under normal, and stressed states. The presentation lasted approximately 7 minutes, and included 3 sets of relaxing images with cats, and 2 sets of disturbing images with dead body parts. Each set of the relaxing images lasted one minute. The first set of the disturbing images lasted one minute, and the last two sets of the disturbing images lasted 2 minutes each. The data collected under the first normal state was used to design algorithms, and to study the effects of skin colors on the SNR of BW signals.

Remote Blood Wave (BW) Signal Detection

Within the context of this research, we formulated a pipeline of image processing algorithms for noise reduction with principal component analysis (PCA) and source selection with independent component analysis (ICA), and applied them to facial skin videos to determine BW signals.

Signal Denoising using Principal Component Analysis (PCA)

In our initial approach, as well as in literature, *signal averaging* was used as the de facto standard for increasing SNR. However, our studies in pulse transit time measurement indicate that the assumption of averaging the exact same signal does not hold, as there are differences in the time of arrival of blood pulse wave between different pixels (Figure 3), resulting in slightly shifted waveforms [15]. While the differences are not as dramatic as in the case of comparing, for example, signal originating from the forehead, and signal originating from the palm, there are still subtle differences between different areas of the forehead or the palm. In our preliminary experiments, we measured differences of the order of 10-20 ms in arrival time between adjacent areas of the palm. Differences in the forehead were less pronounced. However, small phase shifts between the signals from the neighboring pixels will broaden the pulse waveform peaks.

Additionally, in the averaging scenario, losing peak sharpness of a BW signal is an effect of phase noise as well. The problem is essentially equivalent to pulse broadening due to multipath propagation in digital communications; while averaging over an ROI, each capillary represents a slightly different path due to the local vascular anatomy. Antonios et al. report a capillary density in the skin in the order of 70 capillaries per 0.68 mm^2 [93]; numbers increase as we average over larger areas in order to increase the SNR. To preserve the SNR while mitigating the pulse broadening effects introduced by multi-paths, we elected PCA instead of averaging over a region of interest (ROI). Both PCA and Singular Value Decomposition (SVD) [94], [95] have been widely used for denoising in both signal, and image processing [96], [97]. Based on an implied orthogonality between signal and

noise, and assuming that signal energy is higher than the noise, a higher SNR version of the signal is reconstructed by keeping only the signal projections onto the first k eigenvectors.

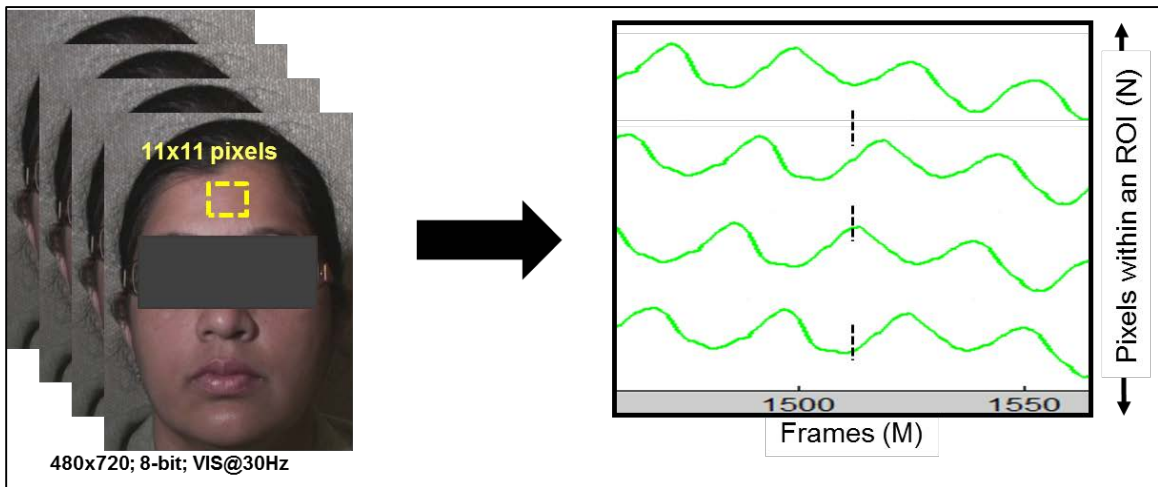


Figure 3: The effects of multipath within an ROI (left) on skin reflectivity signals in green band (right).

A necessary condition for this use of PCA is that the multiple signals used as inputs are synchronized. Non-synchronized signals cause artifacts in the output of the algorithm, with derivative-like signals with the phase shift dominating the eigenvectors after the first one. We used signals from individual pixels over time within an ROI (e.g., 11x11 pixels, Figure 3), after an initial high pass filtering (HPF) in order to remove the baseline variation, as inputs to the PCA algorithm. Similarly to averaging over an ROI, this approach helped with sensor noise. We assumed independence between different pixels; therefore, we

expected PCA to prove more resistant to pulse broadening due to phase shifts between different pixels.

To remove the baseline variations, a HPF filter with size of 250 and the frequency cutoff of 0.5 Hz was designed. This HPF was then applied to the raw signals from RGB bands, and low frequency fluctuations were removed. We then use the filtered signals as inputs to the PCA algorithm, with the analysis running independently for each color channel.

Using the SVD terminology, if X is a matrix with columns representing (normalized) signal recordings from repeated experiments, then it is possible to analyze it in the form:

$$X = USV^T \quad (1)$$

where the columns of U contain the left singular vectors (eigenvectors of XX^T), representing patterns in data; the diagonal matrix S the singular values; and the rows of V^T contain the right singular vectors, indicating the contributions of each left singular vector/eigenvector to each instance of the signal under examination. The maximum variability in the data resides in the first eigenvector, and therefore, it can be used to determine the PCA components with the best signal in the first component as shown in Figure 4.

Additionally, it was noticed that the first principal component in all three bands had the heart beat signal-like periodicity. Further, ICA was applied to detect BW signal from the mixture of three PCA generated components (one from each RGB band).

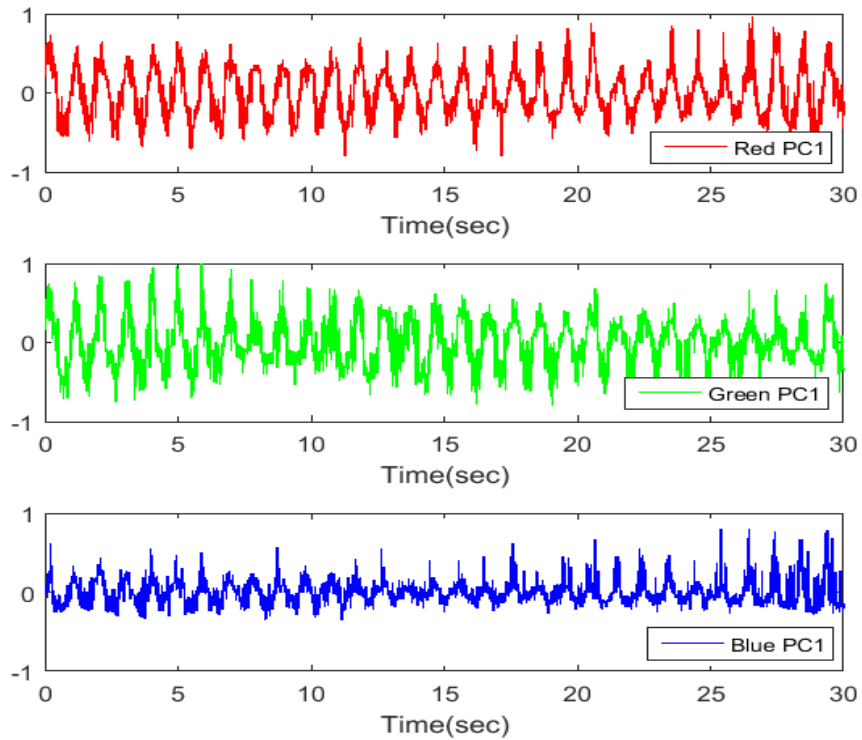


Figure 4: An example of plots with PCA generated first principal component from each band indicating periodicity similar to a cardiac signal: Red (top), Green (middle), and Blue (bottom).

BW Signal Detection using Independent Component Analysis (ICA)

To detect BW signals from the mixture of the three PCA generated components (one from each band), we investigated the use of ICA [18], [98]–[100]. The reason for extending this study to additional signal decomposition techniques was the different underlying assumption; we expect them to behave differently with respect to both phase shifts and noise.

The ICA algorithm is based on two principles: 1) Nonlinear decorrelation (whitening) and 2) maximum nongaussianity (rotation of whitened data) [17], [18], [101]. Applying the ICA algorithm to the PCA generated components ($\overrightarrow{PC1_R}, \overrightarrow{PC1_G}, \overrightarrow{PC1_B}$), three independent components (ICs) were generated. The equation used to compute these independent components is listed below:

$$X = AS \quad (2)$$

where,

X is a signal after applying the mixing matrix A to the source signals S

S is a matrix with PC1 from the red, green, and blue bands as column vectors

The first goal of the ICA algorithm is to compute estimated sources (\hat{S}) by first finding the demixing matrix W that is proportional to the inverse of the mixing matrix A .

$$\hat{S} = WX \quad (3)$$

The whitening operation is performed on the input data X to remove any correlation between the signals (column vectors). During this process, any correlation between the data is reduced to zero, and similar variance for each data set. This operation generates the orthogonal basis for the reduced dimensionality components. The diagonal covariance matrix of the whitened data confirms the accuracy of the whitening operation. Since W is approximately inversely proportional to the matrix A , it is used to rotate the whitened data to generate expected independent components \hat{S} (Figure 5).

Based on the literature [42], and our studies [60], IC2 (Figure 5) is the component that helps with generating a pulse signal with the highest accuracy for cardiac pulse

detection. However, the SNR of the remotely acquired BW signals may depend on various human factors such as melanin, and body locations (e.g., forehead, palm, cheek, etc.). The next section covers the studies we have conducted to learn the effects of these two factors on the SNR value of BW signals.

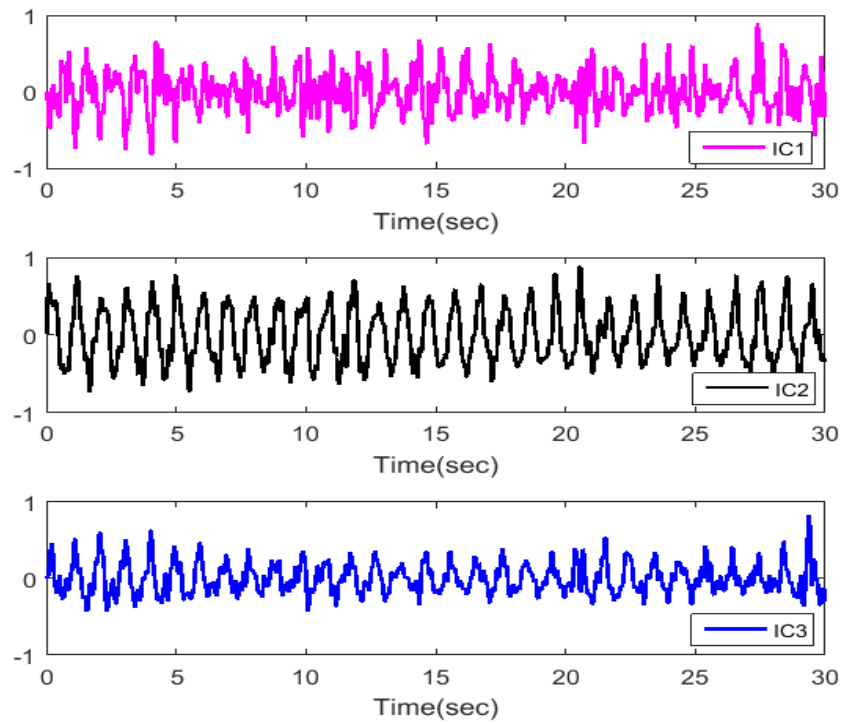


Figure 5: Sample skin reflectivity signals after denoising (PCA) and source selection (ICA) with the highest SNR in the IC2.

Factors Impacting a Remote BW Signal

In this section, we present a study to show the dependency of commonly visible body locations and melanin on SNR of a remotely acquired BW signal. To do this, we used the facial and palm videos from the first experiment.

Dependency of Body Locations on BW Signal

Most studies looking at the remote measurement of BW signals extract them from the face or the forehead. To study the dependency of various body locations, and to identify the best candidate areas with the highest SNR for the BW signal, we expanded our investigation to areas of the body where skin is normally visible. The body locations that we investigated were: forehead left (FL), forehead middle (FM), forehead right (FR), front palm left (FPL), front palm middle (FPM), front palm right (FPR), back palm left (BPL), back palm middle (BPM), back palm right (BPR), chin (CH), cheek left (CL), and cheek right (CR) (Figure 6).

The SNR was computed in the candidate areas using the equation below:

$$SNR = \frac{E_{signal}}{E_{noise}} \quad (4)$$

where, E_{signal} is the energy of the FFT peak corresponding to the BW frequency, E_{noise} is the energy of the entire signal excluding the FFT peak corresponding to the BW frequency.



Figure 6: A subject with the body locations that were investigated to identify the best candidate areas with the highest SNR for the BW signal.

Based on the highest SNR values of the BW signals from various body locations, we have identified that the forehead and the palm are the two optimal locations.

Dependency of Melanin on BW Signal

Since remotely acquired BW signal is based on skin reflectivity, melanin may affect the SNR of a BW signal. To study this effect, we processed facial videos from experiment two, collected under the first normal state and generated BW signals. An SNR value for each BW signal was then determined, and compared among the three skin color groups (light, medium, and dark). Results show a strong dependency of melanin on SNR of BW signals (discussed in the Results section).

Understanding effects of melanin and body locations on BW signals helped with determining BW signals with possible high SNR values. These BW signals were then used to determine RR-intervals, which is the first step for heart rate variability (HRV) analysis.

RR-Interval Estimation from BW Signals

Although a variety of algorithms have been developed to determine BW signals with high SNR values [1], [42], [53], [5], [2], extracting the exact timing information, a process that for the ECG signal involves calculating the positions of the R-peaks of the cardiac waveform, poses several difficulties for the BW signal as it requires estimating the equivalent peak positions in the BW signal. There are two main factors that contribute to it: pulse broadening, due to both the low-pass nature of the cardiovascular system, and multipath propagation effects [89], [90]; and the presence of multiple peaks, due to both reflected waves, and additive noise [91], [92]. Figure 7 gives an overview of this model, where the ECG signal, which has clearly defined peaks due to its high frequency content, is transformed into a low-frequency signal with difficult-to-detect peaks after passing through the cardiovascular system, represented as a lowpass filter, and being subjected to additive noise. This makes the extraction of the RR-intervals a very challenging problem.

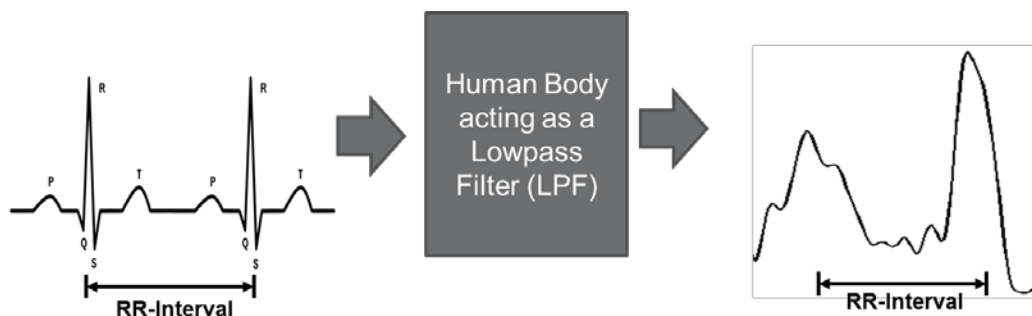


Figure 7: Typical BW signal computed from the human skin reflectivity after the cardiac pulse (ECG) passes through the human body (low-pass filter).

We explored three methods to determine cardiac pulse timing from BW signals based on: zero crossings, curve fitting with filtered LMS, and BDC. A subset of the data from experiment two was used to design these algorithms, and the other subset was used to test the performance of the developed algorithms.

Period Estimation based on Zero Crossings (ZC)

Our first option for estimating periods of a BW signal based on zero crossings involved four steps: 1) remove the DC component from the signal so that the mean value of the signal is zero, 2) determine zero crossings of the entire signal, 3) if number of samples between the two zero crossings is less than a certain threshold value (<10 samples), move to the next zero crossing location (this step helped with mitigating the false peak detections), and 4) identify period locations between the two identified zero crossings. We identified the period locations (Figure 8, blue spikes) as the maximum values (in the rising part of each cycle), which were below the threshold line (Figure 8, red dotted line). These periods were then used to construct RR-interval signals.

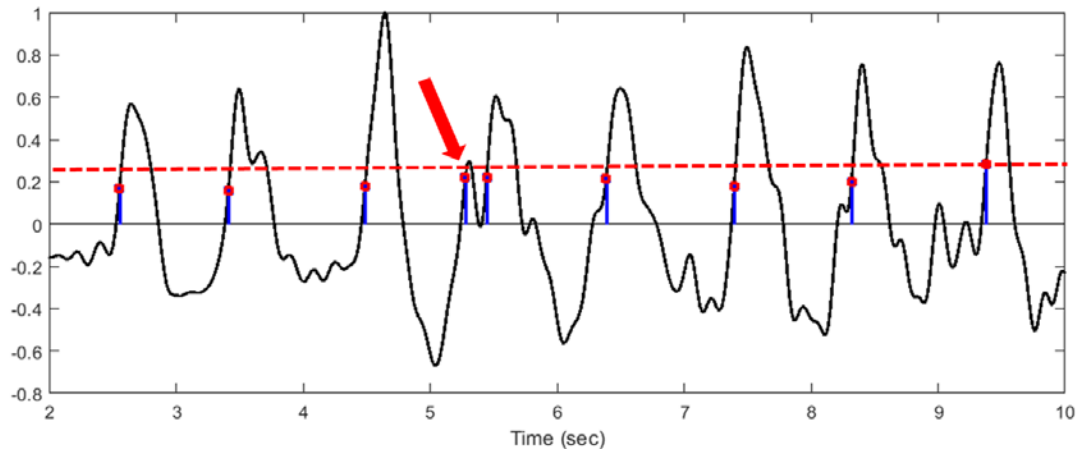


Figure 8: ZC based estimated periods (blue spikes) on a typical BW signal and a false period (red arrow).

Although our ZC based period detection algorithm helped with mitigating local maxima, some false periods (Figure 8, red arrow) could not be avoided. We removed such periods if the distance between the two periods was less than 0.5 times the average period distance. This method helped with selecting a period from the multiple periods within each cycle, but introduced skewness in the underlying structure of the current cycle, and therefore, reported inaccurate cycle locations.

To overcome the challenges of false period detection from BW signals with multiple peaks, we explored two novel methods to first construct BW signals with single peaks, and then use them to detect valid peaks. Our first method employed the least mean squares (LMS) minimization using steepest descent optimization [102], and a low-pass filter to estimate a fit with a relatively clear single peak. Our second method was based on a blind deconvolution (BDC) technique used least squares (LS) minimization to estimate

signals with single peaks [19]. These two methods are discussed in detail in the next two sections.

Peak Detection based on Curve Fitting (CF)

This approach employed a filtered LMS minimization using the steepest descent optimization method to construct a BW signal with single peaks. The modification consisted of introducing a filtering step in every iteration of the algorithm, which constrains it from forming multiple peaks. This new signal is then used to determine peaks that are the close representation of the ECG R-peaks. This algorithm determines a smoother signal without multiple adjacent local maxima by iteratively minimizing the mean square error between the estimated fit and the BW signal. The used optimization method is the steepest descent with small step size (0.01) to avoid oscillations between the estimated values. Since we have shown that the fundamental frequency of a remotely acquired BW signal is close to the one of the GT (ECG) [60], we use the fundamental frequency of the remotely measured BW signal to estimate an initial fit. Employing the filtered LMS CF method, we iteratively determine a smooth signal approximation, peaks of which are then identified and compared to the ECG peaks.

In our approach, the initial estimation $\hat{y}[n]$ is computed as the convolution of an impulse train at the fundamental frequency of the BW signal, determined by using the Fourier transform, convolved with a Gaussian kernel with $\sigma = 0.1$. Following that step, we use the steepest descent with a lowpass filter, to have a better estimate of $\hat{y}[n]$, which has clear local maxima. The algorithm converges if the mean square error (MSE) is not changing significantly between subsequent iterations (e.g., $|MSE_{old} - MSE_{new}| <$

Tolerance). The iteration loop is described as follows, where $\hat{y}[k, n]$ is the current estimation, and $y[n]$ the experimentally acquired data:

Loop Start

1. Determine point-by-point difference between the estimated ($\hat{y}[k, n]$), and the experimentally acquired BW ($y[n]$) signals

$$\hat{d}[k] = y[n] - \hat{y}[k, n] \quad (5)$$

2. Update the estimated BW signal $\hat{y}[k + 1, n]$

$$\hat{y}[k + 1, n] = \hat{y}[k, n] + 2 \times Step \times \hat{d}[k] \quad (6)$$

3. Apply a Gaussian kernel with $\sigma = 0.1$ to the estimated BW signal ($\hat{y}[k + 1, n]$). This step works like a low pass filter, and removes the high frequency contents from the estimated BW signal.

$$\hat{y}[k + 1, n] = \hat{y}[k + 1, n] * h[n] \quad (7)$$

4. Determine the MSE between $\hat{y}[k + 1, n]$ and $y[n]$

$$MSE_{new}[k + 1] = \|y[n] - \hat{y}[k + 1, n]\|^2 \quad (8)$$

5. Test for the algorithm convergence

$$\text{Convergence} = \begin{cases} \text{Yes} & , MSE_{new}[k + 1] - MSE_{old} < Tolerance \\ \text{No} & , MSE_{old} = MSE_{new}[k + 1] \end{cases} \quad (9)$$

6. If convergence is achieved, quit loop; otherwise, repeat from step 1

Figure 9 shows an example with the CF algorithm generated peaks (in blue). Clearly, the high frequency fluctuations were removed from the final estimate (in red).

Filtered LMS alternates between the steepest descent and filtering step, thereby converging into a smooth version of the original signals.

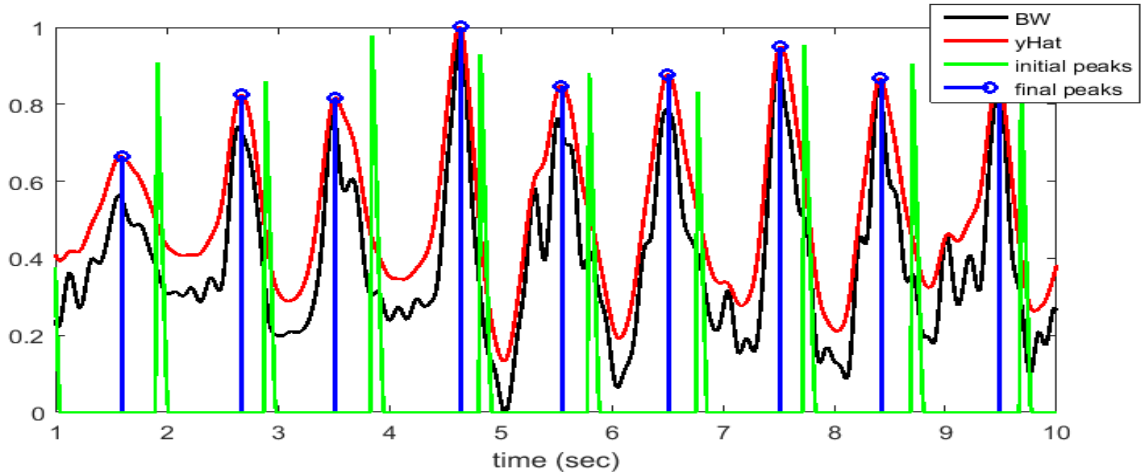


Figure 9: An example with CF algorithm generated plots with BW signal (black), initial peaks (green), estimated BW signal (red), and final peaks (blue).

Peak Detection based on Blind-Deconvolution (BDC)

In our second approach, we adapted the blind deconvolution (BDC) method to detect peaks from the observed BW signals that closely represented the GT peaks. The proposed BDC method uses the available BW signals and decomposes them into an input sequence ($\hat{x}[n]$), that is constrained to resemble an impulse train, and an estimated impulse response ($\hat{c}[n]$) of the cardiovascular system. These two parameters are initialized using the experimental data. Based on our observations of the BW signals and the associated ground truth, we believe that the human body acts as a lowpass filter (LPF), and therefore, we initialized the human body response ($\hat{c}[n]$) to a heartbeat signal as a lowpass filter. To

estimate an initial input signal ($\hat{x}[n]$), we applied a sinusoid curve fitting algorithm to the BW signals and used the detected peaks from each cycle to construct an impulse train. Then we used a Gaussian kernel with $\sigma = 0.1$ as an initial estimate of the human body response ($\hat{c}[n]$)

The BDC algorithm uses the closed form of the linear least mean squares (LMS) solution ($x = (S'S)^{-1}S'y$). The closed form of the LMS is driven from the model $y = Sx + e$ and estimates the input signal (x) by minimizing the error between the original BW signal (y) and the estimated signal (\hat{y}). In the equation, S is a convolution matrix with $m + (p - 1)$ rows and m columns. Row i of S contains the flipped and shifted (by $i-1$) copy of c and therefore, the columns of S are the identical but shifted, which results in a band matrix. Notice that we have two unknown parameters, the system response and the input to the system response. Using LMS minimization, we estimate these two parameters iteratively, with an iteration control parameter ($\beta = 0.0005$) to control the number of iterations, and a ridge penalty tuning parameter ($\alpha = 0.0007$) to prevent the singularity issues. At each iteration, the MSE between the original (y) and the estimated ($\hat{y}[k]$) BW signal is computed, and the algorithm converges when the MSE is no longer changing significantly (e.g., $|MSE_{old} - MSE_{new}| < \text{Tolerance}$). Alternating between estimating $\hat{x}[k]$ and $\hat{S}[k]$ to determine an optimized estimate makes this algorithm a blind deconvolution algorithm; both the input and the impulse response of the system are estimated in an iterative fashion, without the need of knowing one of them, as in the normal deconvolution problem. The iteration loop is described in detail as follows, where $\hat{y}[k]$ is the current estimation and y the experimentally acquired data:

Loop Start

1. Estimate $\hat{x}[k + 1]$ using regularization. Since the columns of S are the shifted copies of the impulse response, they are strongly correlated, and therefore, introduce singularity issues, which leads to the ill-conditioned S matrix. Regularization helps with conditioning the matrix, and mitigating singularity problems. Regularization is introduced through penalties such as the L0, L1, and L2 norms. Because we are interested in the estimated ($\hat{x}[k + 1]$) signal with sparse spikes representing an impulse train, we used the L0 penalty. The regularization parameter, W is a diagonal matrix, and the penalties (L0, L1, and L2) can be represented using the equations below [19]:

$$W_{jj}[k] = \left(\frac{1}{(\hat{x}_j[k])^2 + \beta^2} \right) \quad (\text{L0 penalty}) \quad (10)$$

$$W_{jj}[k] = \left(\frac{1}{\sqrt{(\hat{x}_j[k])^2 + \beta^2}} \right) \quad (\text{L1 penalty}) \quad (11)$$

$$W_{jj}[k] = 1 \quad (\text{L2 penalty}) \quad (12)$$

$$\hat{x}[k + 1] = (\hat{S}[k]^T \hat{S}[k] + \alpha W[k])^{-1} \hat{S}[k]^T y \quad (13)$$

Where, j represents the location in the \hat{x} vector and jj the diagonal location in the W matrix.

2. Estimate $\hat{S}[k + 1]$. Since the human body's system response function is not known, may vary from subject to subject, and may vary for a subject over time, we estimate the system response to a given heartbeat signal iteratively using

closed form solution of the LS minimization. Three steps involved to estimate $\hat{S}[k + 1]$ are as follows:

- a. Estimate $X[k]$, the convolution matrix. The rows of which are the shifted copies of the most recent input estimate ($\hat{x}[k + 1]$).

$$X[k] = \begin{bmatrix} \hat{x}[k + 1, p + 1 - n] \\ \hat{x}[k + 1, p + 2 - n] \\ \hat{x}[k + 1, p + 3 - n] \\ \vdots \\ \hat{x}[k + 1, p + i - n] \end{bmatrix} \quad (14)$$

- b. Estimate $\hat{c}[k + 1]$, the updated impulse response. To estimate this parameter, a regularization is not needed because this is a well-conditioned regression problem as the size of the convolution kernel (\hat{c}) is much smaller than the input (\hat{x}) and the output (y) signals.

$$\hat{c}[k + 1] = (X[k]^T X[k])^{-1} X[k]^T y \quad (15)$$

- c. Construct $\hat{S}[k + 1]$, the updated convolution matrix. The rows of $\hat{S}[k + 1]$ are the flipped and shifted copies of the most recent impulse response estimate ($\hat{c}[k + 1]$).

$$\hat{S}[k] = \begin{bmatrix} \hat{c}[k + 1, p + 1 - n] \\ \hat{c}[k + 1, p + 2 - n] \\ \hat{c}[k + 1, p + 3 - n] \\ \vdots \\ \hat{c}[k + 1, p + i - n] \end{bmatrix} \quad (16)$$

3. Estimate $\hat{y}[k + 1]$, the estimated BW signal

$$\hat{y}[k + 1] = \hat{S}[k + 1] \hat{x}[k + 1] \quad (17)$$

4. Compute MSE between the original (y) and the estimated ($\hat{y}[k + 1]$) BW signals

$$MSE_{new}[k + 1] = \|y - \hat{y}[k + 1]\|^2 \quad (18)$$

5. Test for the algorithm convergence

$$\text{Convergence} = \begin{cases} \text{Yes} & , |MSE_{new}[k + 1] - MSE_{old}| < Tolerance \\ \text{No} & , MSE_{old} = MSE_{new}[k + 1] \end{cases} \quad (19)$$

6. If convergence is achieved, quit loop; otherwise, repeat from step 1

Loop End

Employing the BDC algorithm, we processed pilot data to estimate impulse trains and impulse responses using L0, L1, and L2 penalties. L2 penalizes large values, so this should lead to an energy distribution that includes a maximum number of small nonzero values. L0, on the other hand, penalizes nonzero values, so it tends to concentrate the input energy in as few nonzero values as possible. L1, which looks at the sum of the values, does not favor either distribution. Figure 10 shows an example of the estimated impulse train (left in red), and the system response (right in red) with L0 penalty. It shows that the estimated impulse trains (in red) closely align with the BW cycles (in black). On the other hand, the estimated trains with L1, and L2 penalties had more spikes (Figure 12 and Figure 13), and were not successful in producing an $x[n]$ estimation that was an impulse train. In addition, Figure 11 shows that the BDC algorithm for a typical BW signal with L0 penalty converges to the steady-state MSE value in less than 100 iterations. Based on this analysis, L0 was determined to be the best penalty for our application, and therefore, BDC algorithm with L0 penalty was used as the third algorithm to detect peaks from the experimental data.

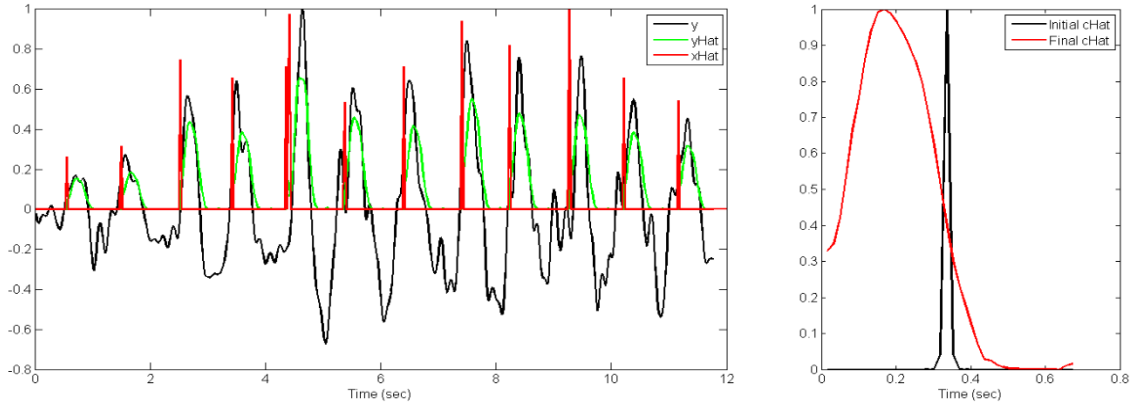


Figure 10: An example with estimated input (left-red curve) and impulse response (right-red curve) with L0 penalty.

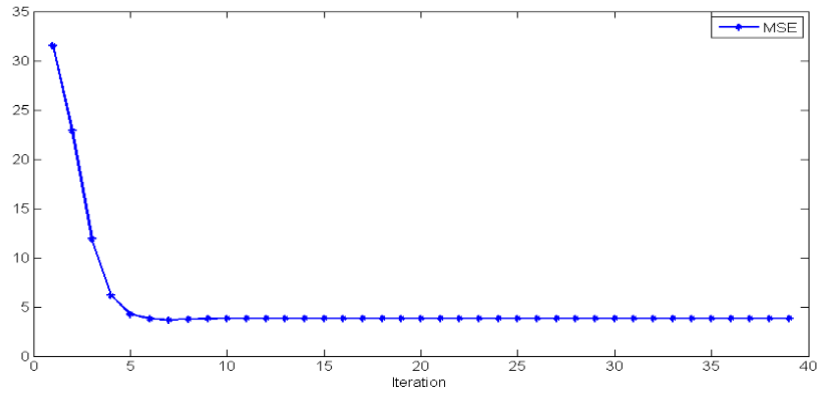


Figure 11: An example of the plot with MSE between BW signal and the estimated BW signal showing the convergence of the BDC algorithm using L0 penalty.

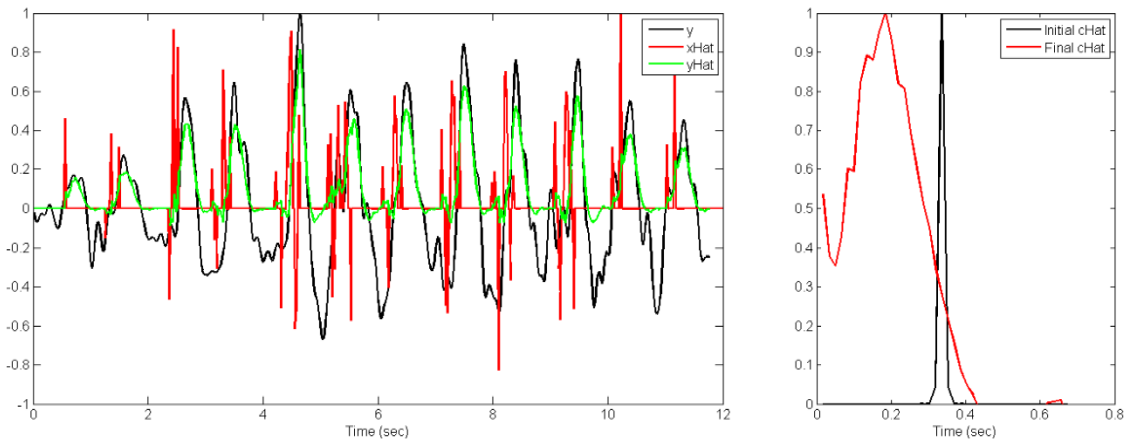


Figure 12: An example with estimated input (left-red curve) and impulse response (right-red curve) with L1 penalty.

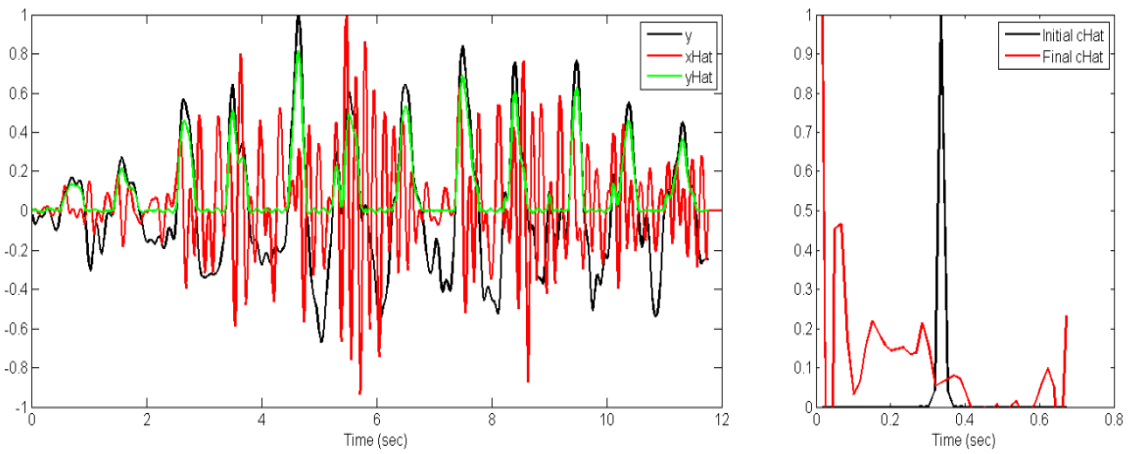


Figure 13: An example with estimated input (left-red curve) and impulse response (right-red curve) with L2 penalty.

Validation for Accurate Peak Detection

To validate the accuracy of the algorithm detected peaks, they were compared with the GT peaks. The error was reported by means of the absolute normal error (%), and the standard deviation of the absolute normal error (%). Equations used to determine these errors are as follows:

1. Absolute error

$$Err_i = |t_{o,i} - t_{VIS,i}| \quad (20)$$

Where, $t_{o,i}$ are the GT peak locations, $t_{VIS,i}$ are the BW peak locations; i is the peak number; $i = 1,2,3,\dots,N$; N is the total number of peaks

2. Absolute normal error (%)

$$\overline{Err} = \frac{1}{N} \sum_{i=1}^N Err_i \quad (21)$$

3. Standard deviation of the normal error (%)

$$S = \sqrt{\frac{\sum (Err_i - \overline{Err})^2}{N-1}} \quad (22)$$

Determine RR-interval Signals

The periods or the peaks generated by the algorithm that had the smallest absolute normal error and the smallest standard deviation of the normal error were used to generate RR-intervals. A series of these RR-intervals make the RR-interval signal. Following the novel methods to first generate BW signals and then to detect peaks based on single peaked signals helped with generating clean RR-interval signals that were further used for stress detection (Chapter Five).

Results

Figure 14 shows the average SNR values of the BW signals measured at all suggested body locations from 15 subjects. As clearly seen, both the palm and the forehead (two distal body locations) show a relatively high SNR value as compared to the other body locations. We use the forehead as an optimal location to acquire BW signals for the purpose of HRV analysis for stress detection, and both forehead and palm as the optimal locations for dPTT computations.

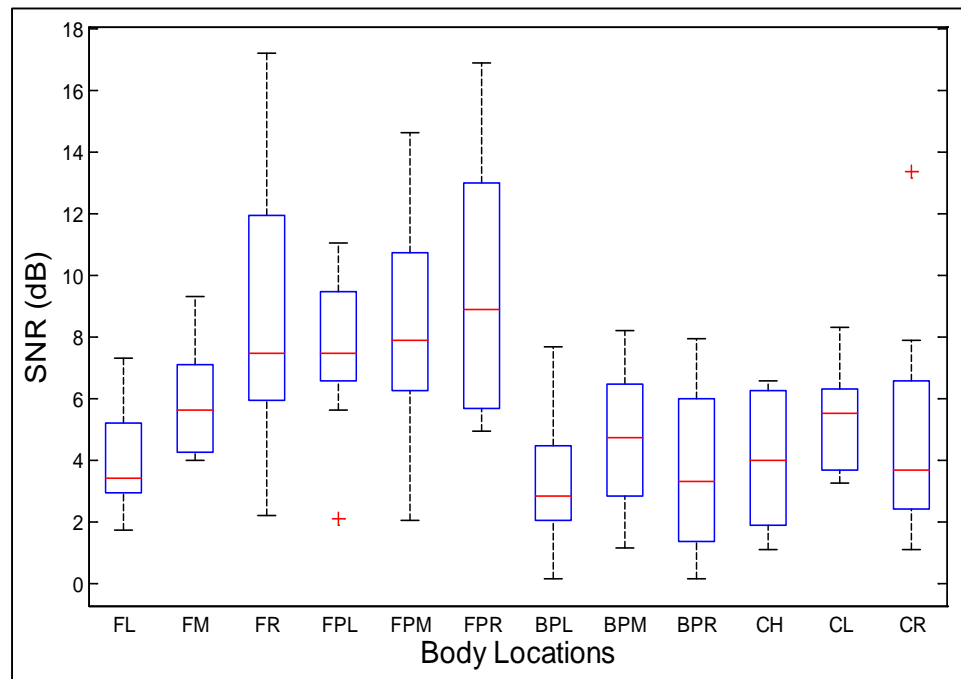


Figure 14: SNR measurements of BW signal from 12 different body locations indicating the highest SNR for the palm and forehead location.

Figure 15 shows the average SNR value of the remotely acquired BW signal for the three skin color type from 15 subjects. As clearly seen, SNR values range from low to high as the pigmentation (skin color) decreases (dark to light). Therefore the plot indicates a strong dependency of melanin on the SNR value of the remotely acquired BW signals.

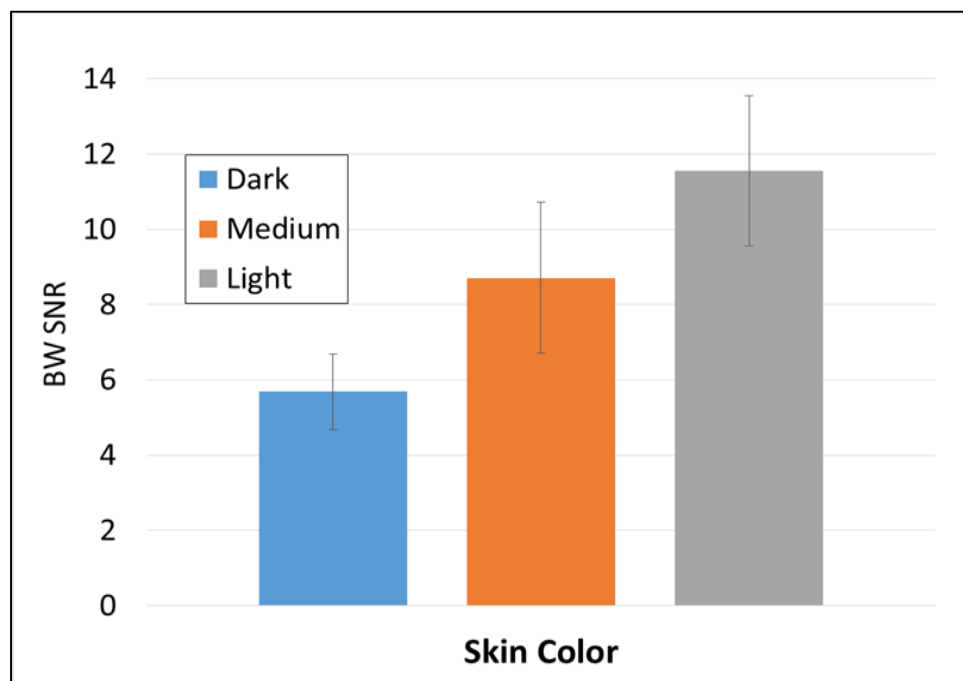


Figure 15: Plots showing a lower average SNR values for the darker skin color.

Following the methods for period/peak detection based on ZC, CF, and BDC with L0 penalty, data from the experiment two under the first normal state were processed, and peaks were detected. The periods/peaks detected by the three algorithms were then

compared with the GT peaks by means of absolute normal error, and the standard deviation of the normal error (Figure 16).

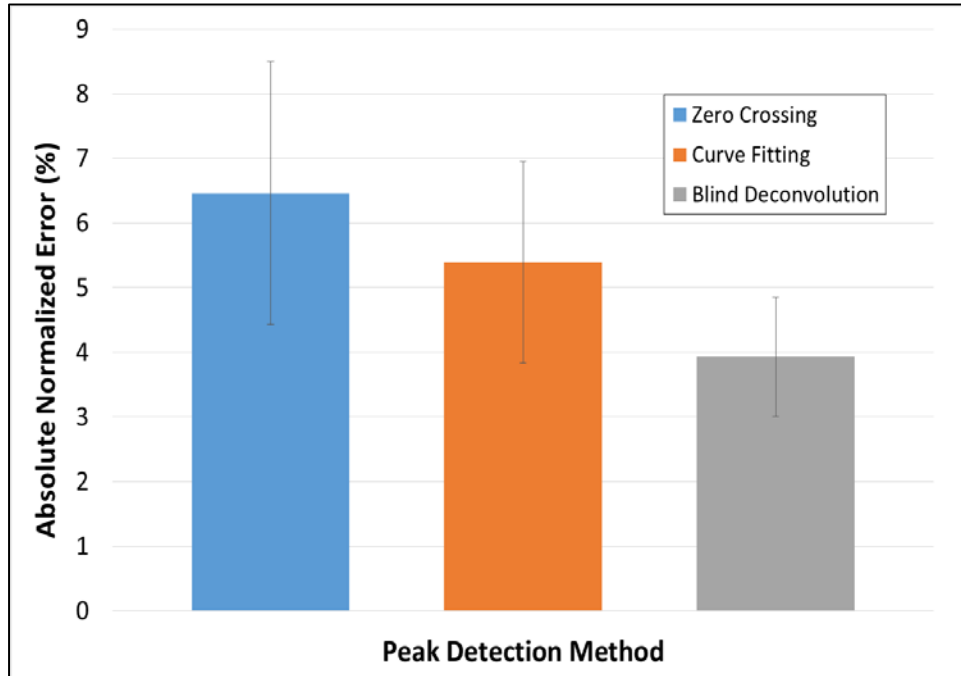


Figure 16: Plot showing the bars with absolute normalized error between the GT and the three algorithms (ZC, CF, and BDC).

The absolute normal errors for the ZC, the CF, and the BDC algorithms were 6.46%, 5.39%, and 3.93% respectively. The standard deviations of the absolute normal error for the ZC, the CF, and the BDC algorithms were 3.90%, 3.84%, and 2.63% respectively. In addition, when compared with the ZC algorithm, an improvement in absolute normal error of 37.17% was achieved with the CF algorithm, and 64.40% with the BDC algorithms. When compared with the ZC algorithm, an improvement in standard

deviation of the absolute normal error of 46.18% was achieved with the CF algorithm, and 48.32% with the BDC algorithm. Overall, BDC algorithm outperformed the other two period/peak detection algorithms.

Finally, the BDC algorithm generated peaks were used to construct clean RR-interval signals, which were then used for the HRV analysis (discussed in Chapter Four). Figure 17 shows an example of GT and VIS peaks (top), and the generated RR-interval signals (bottom). Clearly, similarities between the GT and the VIS peaks yield results in the RR-intervals, which also closely matched with RR-intervals from GT, and therefore, resulted in a clean RR-interval signal.

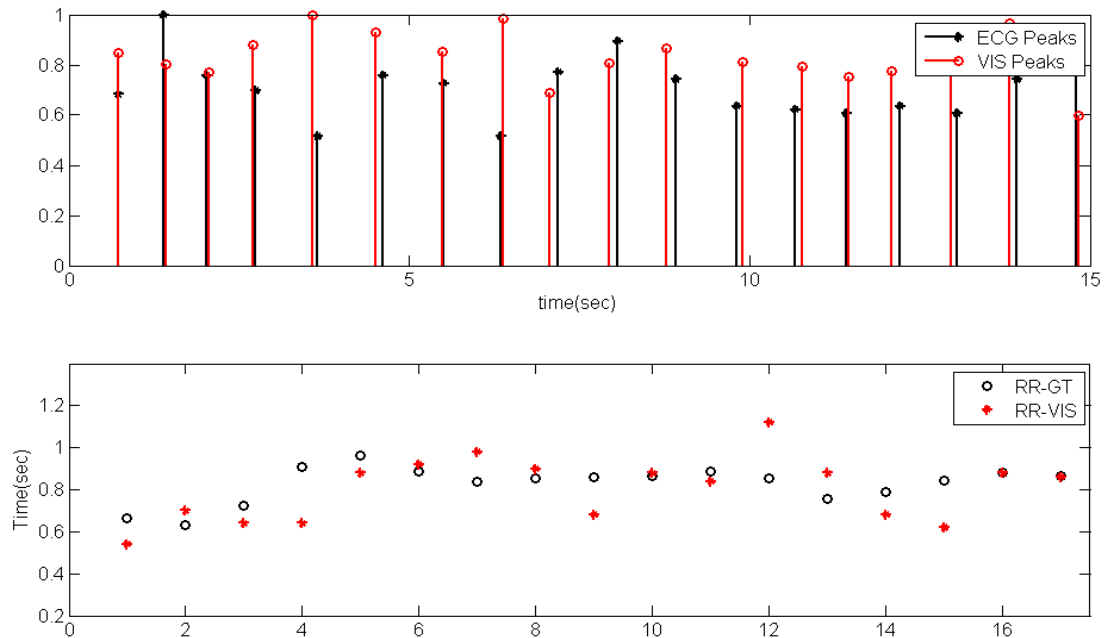


Figure 17: An example with the VIS and GT peaks (top) and RR-interval signals (bottom) showing a close relationship between the two.

Discussion

In this work, we were able to demonstrate that the newly developed algorithm for BW signal detection, and peak detection (BDC) can help with detecting peaks that are highly correlated with GT. Using the BDC algorithm, the absolute normal error, and the standard deviation of the normal error between GT and BW signal peak locations, was relatively low (3.93%, and 2.63%) as compared to the two other peak detection algorithms (ZC and CF), and therefore, BDC outperforms the other two algorithms. Our results are in agreement with literature [19], which shows that the use of L0 penalty in the BDC algorithm can constrain the input estimation to a sparse solution, resembling an impulse train. In our experience, as long as the regularization parameter, the initial estimates of the impulse response, and the impulse train are defined appropriately, the BDC algorithm can detect peaks with high accuracy.

When compared to the ZC and CF algorithms, BDC is a novel method for estimating two unknown parameters: the impulse train representing the peaks of the BW signal, and the human body response to that estimated impulse train. As expected, this method provided an individualized response to each subject. Moreover, this method was computationally faster than the other two methods (converges in less than 100 iterations). Finally, as compared to our initial ZC based period detection algorithm, BDC helped with improving an absolute normal error by 64%, and the standard deviation of the normal error by 48%.

Overall, our results demonstrate that the BDC based detected peaks are highly correlated with the GT, and therefore, can help with generating cleaner RR-interval signals, which is the first step for HRV analysis [1]. While further research is needed to improve both acquisition and data processing strategies, we believe that our study shows the potential of a non-contact, potentially covert system for remote vital sign detection, which can be used for many medical, and security applications.

CHAPTER FOUR: REMOTE MEASUREMENTS OF HEART RATE VARIABILITY AND ITS USE FOR STRESS DETECTION

Introduction

Heart Rate Variability (HRV) is a measure of change in the periodicity of the heartbeat signal, and is also implicated in the “fight-or-flight” stress response. We define the HRV as the statistical change in the remotely acquired blood wave (BW) signal from small differences of the skin color in visible spectrum videos. Overarching goal of this chapter was to merge the research conducted in the areas of remote BW signal detection in the visible spectrum and contact HRV, and investigate the possibility of detecting physiological stress using a novel, contactless method. In this chapter, we have developed a pipeline of algorithms which involves BW signal detection and RR-interval generation following the novel methods developed in Chapter Three, HRV-driven features generation and identification of stress-significant HRV-driven features, and stress detection using experimental data.

First, we determined BW signals and RR-interval signals for normal and stress physiological states by following the novel methods developed in Chapter Three. In this chapter, for the purpose of comparing RR-intervals from two physiological states, we determined statistical (HRV-driven) features in both time and frequency domains, and

identified a set of stress significant features based on the paired t-test. Further, we explored logistic regression (LR) and linear discriminant analysis (LDA) classifiers to distinguish stress states from the normal ones.

To prove the efficacy of the developed algorithms, ECG recordings and facial skin videos collected under the three experiments were processed to distinguish stress states from the normal ones. The goodness of the used classifiers was measured in terms of sensitivity/specificity, and the results were reported in terms of receiver operating characteristic (ROC) curve for each level of stress state.

Additionally, the experimental data were used to determine the feasibility of a classifier for stress detection by answering the following three questions:

- 1) Which classifier is feasible for stress detection using contact HRV-driven features?
- 2) Will the identified classifier be feasible for stress detection using remote HRV-driven features?
- 3) Are the stress detection results repeatable with the identified classifier?

To answer these questions, we used the HRV-driven features from both ECG and facial videos from all three experiments. To answer the first question, the ECG data from the first experiment was used to test the scope of the identified classifiers for stress detection and to identify the feasible classifier for stress detection. To answer the second question, the identified classifiers were used to process facial skin videos from the second experiment to verify that the identified classifier is actually feasible for stress detection for

visible data, as well. To answer the third question, we processed facial skin videos from the third experiment using the identified classifier and compared the generated results with the results from experiment two to determine if they were repeatable.

Because ECG signals are much cleaner as compared to the remote BW signals, we expected to detect all stress levels. However, given that the remote RR-interval signals would have some noise, we expected to detect only high and mild stress levels with high confidence. Our results confirm that, and show a proof of principle for the use of remote HRV for stress detection, and therefore, a further development of a remote-sensing stress detection system based on remote HRV.

Materials and Methods

This chapter has two major goals related to the algorithm development: the first is to identify stress significant HRV-driven features, and the second is to explore classifiers that can be used to distinguish stress states from the normal ones. The research in this chapter builds on the work discussed in the background chapter, addressing important problems that arise when trying to classify various levels of physiological stress states. Keeping these two goals in mind, we designed experiments to induce stress at various stress levels, and used the experimental setup discussed in Chapter Three to collect facial skin videos and ECG signals. A set of experiments conducted to design algorithms are discussed as follows.

Experiments

With a goal to acquire remote heartbeat signal with high SNR values under the stress and normal physiological states, and to explore their use for stress detection, we conducted three experiments: one using a modified “Trier Social Stress Test” (TSST) and the other two using an “Affective Stress Response Test” (ASRT). During experiments, participants were asked to sit in a chair 5 feet away from the camera, as still as possible, and look at a computer screen in front of them, while we recorded their facial videos and ground truth (ECG).

The first experiment was designed to collect data from 13 subjects using the TSST, in which stress was induced by asking a subject to prepare and deliver a five minute speech. During our modified version of the test, we had four stress states in which: 1) subjects were asked to fill out a perceived stress scale test (“scale”), 2) read text from the monitor screen (“Read Text”), 3) subsequently prepare (“Announce”), and 4) deliver the speech (“Talk”) on an investigator’s announced talk topic. During the experiment, resting states were incorporated in which subjects were asked to relax. A resting state of 2 minutes was introduced prior to the first and second stimulus, 1 minute prior to the third stimulus, and 5 minutes after the fourth stimulus. For the purpose of designing stress detection algorithms using this experimental data, we defined four cases in which the first resting state would be compared with the four stress states: case1- Rest to Scale; case 2- Rest to Read Text; case 3- Rest to Announce; case 4- Rest to Talk.

The second experiment was designed to collect data from 15 subjects using an ASRT, in which subjects were asked to view a series of pleasant and unpleasant images. The images (stimuli) presented on the computer screen were a series of photos, alternating between cat photos and photos of dead people (chosen so as to make the participants feel uncomfortable). Three alternating sets of images were shown to capture human physiological responses under normal and stress states. The stimuli presented on the computer screen were 3 sets of images, alternating between cat images and images of dead people for 1.5 minutes each. Total duration of the experiment was 10.5 minutes. For the purpose of testing the developed stress detection algorithms against visible data from this experiment, we defined three cases in which baseline (the first) normal state would be compared with the three stress states: case1- Normal to Stress1; case 2- Normal to Stress2; case 3- Normal to Stress3.

The third experiment was designed to repeat the second experiment with some modifications (discussed below) and induce stress using the ASRT. The purpose, the experimental setup, and the stimuli presented on the computer screen were similar to the second experiment. However, during this experiment, we increased the resting intervals from 1 minute to 2 minutes to bring a subject's physiological state to "Normal". This change in the experiment was designed to measure the true response of ANS as the stimulus was introduced for the second time. The presentation lasted approximately 7 minutes, and included 3 sets of relaxing images with cats and 2 sets of disturbing images with dead body parts. Each set of the relaxing images lasted one minute. The first set of the disturbing images lasted one minute, and the last two sets of the disturbing images lasted 2 minutes

each. To test the stress detection algorithms against facial skin videos from this experiment, we defined two cases in which baseline (the first) normal state would be compared with the two stress states: case1- Normal to Stress1; case 2- Normal to Stress2.

All experiments were designed to induce multiple stress levels by presenting stimuli. The algorithms were developed using the ECG data from the first experiment, and then the developed algorithms were tested against the facial skin videos from experiments two and three to identify the feasible classifier. In addition, to test the repeatability of the stress detection algorithms, results from the second and the third experiments were compared.

Prepare Data for HRV Analysis

In the process of designing algorithms for HRV based analysis for stress detection, we used the first 30 second interval from each physiological state. Both ECG and facial videos were processed to determine RR-intervals from each state.

First, the original Pan and Tompkins method for QRS detection [103] was used to determine ECG peaks. These peaks were then used to determine RR-intervals and the resultant RR-interval signals.

A BW is the remotely measured heartbeat signal. The BW signals were constructed from facial videos (within an ROI placed at forehead) based on minor intensity fluctuations during the heartbeat [104], [105]. To mitigate the phase noise and pulse broadening effects, we applied principal component analysis (PCA) to the color intensity time series for each pixel in a region of interest (ROI) in order to obtain a signal with a higher SNR value. This

yielded three signals, one for each color band (RGB). To select the BW signal from them, we used independent component analysis (ICA). The BW signal corresponded to the second independent component in the resulting signal. The peaks of the detected BW signals were then detected using a blind deconvolution algorithm based on least squares minimization approach. These peaks were then used to determine RR-interval signals.

Determine HRV-Driven Features for Stress Detection

In order to compare RR-interval signals (from different states), we needed a standard set of statistical matrices (e.g., HRV-driven features), representing the variability in the signals. The use of HRV-driven features helped with setting up a framework for comparing two RR-interval signals based on their variability. We used the Heart Rate Variability Analysis Software (HRVAS) [106] and computed ~ HRV-driven 103 features . The HRVAS software computed features in both frequency and time domains, using the algorithms such as: the Welch, the Burg, and the Lomb-Scargle periodograms. Figure 18 shows a screenshot of the HRVAS GUI along with the variables that were used to compute HRV-driven features from a sample RR-interval signal. These parameters were adjusted based on the number of samples in an RR-interval signal.

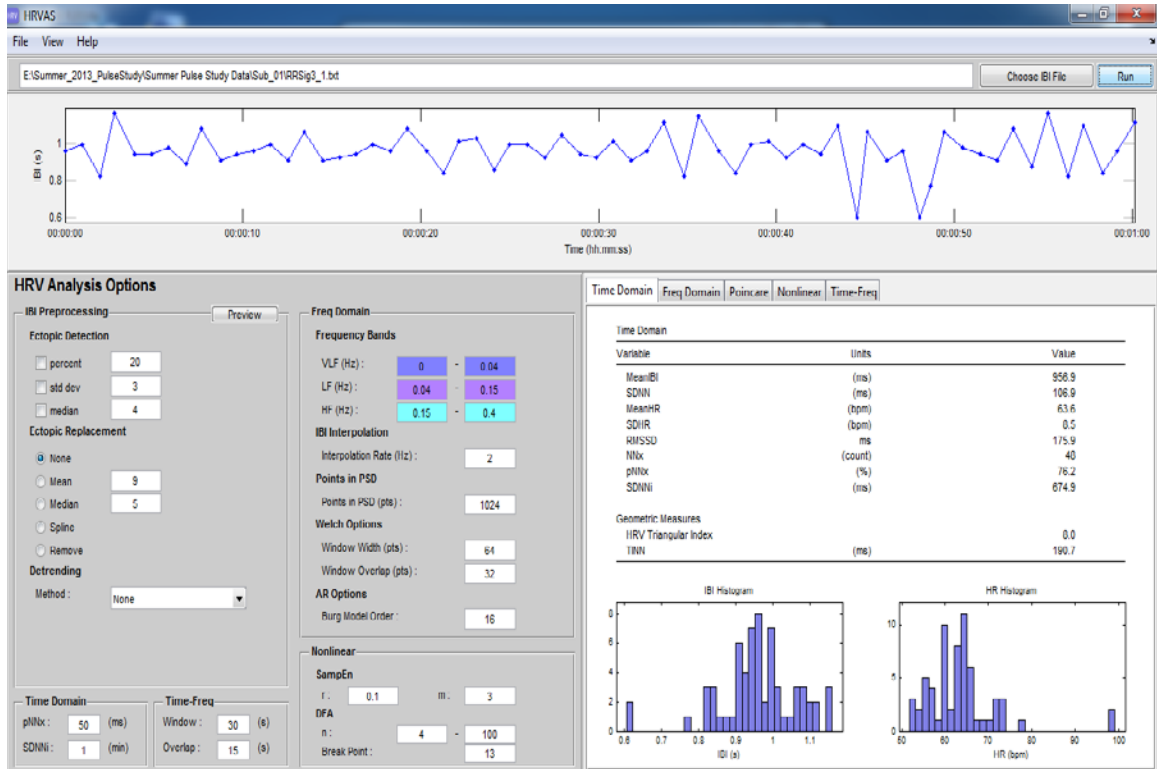


Figure 18: HRVAS GUI used to compute HRV-driven features from RR-interval signals for both normal and stress states.

Since HRVAS computed ~103 HRV-driven features, not necessarily all were relevant for stress detection. To identify the relevant HRV-driven features that were significantly different under the two physiological states, we employ a well-known and widely used statistical test called the paired t-test [107]. Based on this test, we identified the relevant HRV-driven features based on their p-value (<0.05).

Classification for Stress Detection

The identified relevant features for stress detection could not be used individually for stress detection due to the lack of high significance. However, they could be combined

to increase their significance for stress detection. To do this, we explored various classification methods to combine and to transform these features. The two classifiers that gave us the best results were: logistic regression (LR) [108] and linear discriminant analysis (LDA) [109]. These classifiers were tested against the ECG data and the generated results were then compared to identify the best classifier for remote stress detection.

Normally, a subset is used to train classification algorithms for a large data set, and a different subset is used for cross validation. However, in the case of a limited data set, “leave-one-out” is a preferred approach [110]. For example, for a data set of 26 samples (13 normal cases and 13 stress cases) from 13 subjects, the leave-one-out method would have 26 iterations, with 25 observations to train the classifier and one sample to validate. This scheme allows for the use of entire data set training and cross validating for stress detection.

Classification based on Logistic Regression (LR)

To classify stress states, our first selection was the logistic regression (LR) [108]. Based on the HRV-driven features, LR computed the location of a given state on the sigmoid function. The leave-one-out data analysis method was adapted to classify stress states from the normal ones. The LR’s hypothesis/sigmoid function and the classification conditions are as follows:

$$h_{\theta}(x) = \frac{1}{1+e^{-\theta^T x}} \quad (23)$$

$$h_{\theta}(x) = g(z) \quad (24)$$

$$\text{where, } z = \theta^T x \quad (25)$$

$$h_{\theta}(x) = g(z) = \begin{cases} \text{normal}; & z \geq \text{threshold} \\ \text{stressed}; & z < \text{threshold} \end{cases} \quad (26)$$

Based on the values of $g(z)$ for each data point, a state is assigned. For example, normal state is assigned to the data point if $z \geq \text{threshold}$, and a stress state is assigned to the data point if $z < \text{threshold}$. A threshold value is determined based on the average value of the training data. Below is an example of an LR model with the two boundaries (normal and stress) and test data point projections onto the model. The location of the projected test data determines the association of the test data with the normal (Figure 19, left) or stress states (Figure 19, right).

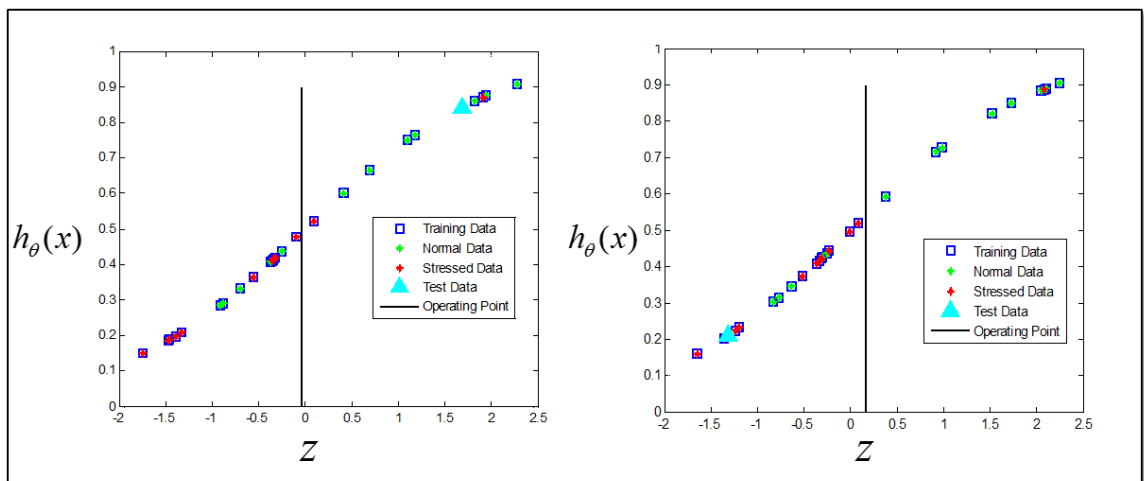


Figure 19: An example of generation and usage of Logistic Regression based model for classification of normal (left) and stress (right) states.

Classification based on Linear Discriminant Analysis (LDA)

Our second classifier was the LDA that we used to discriminate stress states from normal ones [109]. An LDA algorithm employing Fisher's criterion provides a projection vector for the original data transformation onto a vector space. The projection vector is calculated such that the distance between the classes is maximized and distance within each class is minimized. After projecting both HRV-driven features from normal and stress classes onto this projection vector, the average location of each class is computed. Then each test data point is mapped onto the LDA projection space and, based on the minimum Euclidian distance of this test point to each class' average location, its class association is formed. Below is an example with the data distribution for two classes using only two features indicating the spread, which is difficult to classify with a linear segmentation boundary (Figure 20, left). Figure 20, right, indicates the implication of the LDA projection to create a better separation between the two classes, which is based on the Fisher's criterion.

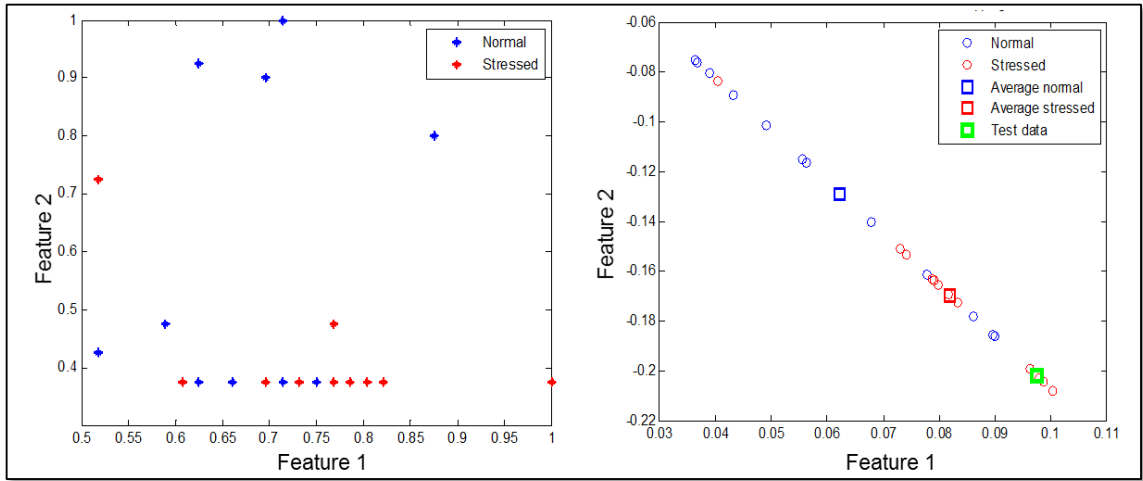


Figure 20: An example of data (two classes) distribution with two features only (left); LDA generated projection vector to maximize the inter-class separation and minimize intra-class separation (right).

Confidence Metrics to Quantify Algorithm Performance

To study the overall performance of the identified classifiers, results were quantified by the criteria of sensitivity, specificity, precision, and accuracy: 1) by sensitivity, we mean the probability of declaring the subject “stressed” if the subject is actually in the stress state, 2) by specificity, we mean the probability of declaring the subject not “stressed” if the subject is actually not in the stress state (1-specificity defines the probability of declaring a subject stressed if the subject is not stressed), 3) by precision, we mean the probability of being right when the algorithm declares a subject “stressed,” or the number of times correctly declaring “stressed”/the total number of times the algorithm states “stressed”, and 4) by accuracy, we mean the probability of declaring the stress and normal states correctly. Equations used to compute these metrics are as follows:

$$Sensitivity = \frac{TP}{TP+FN} \quad (27)$$

$$Specificity = \frac{TN}{TN+FP} \quad (28)$$

$$Precision = \frac{TP}{TP+FP} \quad (29)$$

$$Accuracy = \frac{TP+TN}{TP+TN+FP+FN} \quad (30)$$

where, TP = true positives, FN = false negatives, TN = true negatives, and FP = false positives.

Results

Using human facial skin and ECG data from experiment one, we processed 30 second segments from each state and computed the RR-interval signals from 13 subjects. These RR-intervals were then processed using the HRVAS software to compute HRV-driven features. Applying the procedure for relevant feature selection (discussed above) to the remote HRV-driven features under the first two physiological states, nine HRV-driven features were identified that were significantly different, and therefore, relevant for stress detection. These identified relevant HRV-driven features (Table 1) were in agreement with the literature [111].

Table 1: A list of task relevant HRV-driven features for stress detection.

Features	Description
HRVTi	HRV Triangular Index $(D(t)/Y)$ $D(t)$ = density distribution of the histogram of RR-interval Y = maximum value of $D(t)$
pVLF (%)	Percentage of the sum of absolute very low frequency (0.003-0.05 Hz)
pLF (%)	Percentage of the sum of absolute low frequency (0.04-0.15 Hz)
pHF (%)	Percentage of the sum of absolute high frequency (0.15-0.4 Hz)
SD (ms)	Standard deviation
LFHF	The ratio of LF to HF
nLF (%)	Normalized to total power low frequency
nHF (%)	Normalized to total power high frequency
peakHF (HZ)	Peak of the high Frequency

The variability of the identified relevant features is shown in box and whisker plots (Figure 21). These plots show the distribution of each relevant feature for both normal and stress states from all tested subjects under experiment one. In addition, box and whisker plots can be used to visualize the overlap between the two states for a given feature. As clearly seen in the plots, the peaks for each feature for both states do not overlap significantly, and therefore, these features can be used for stress detection. A combination of these features would add power for a better discrimination between the two states.

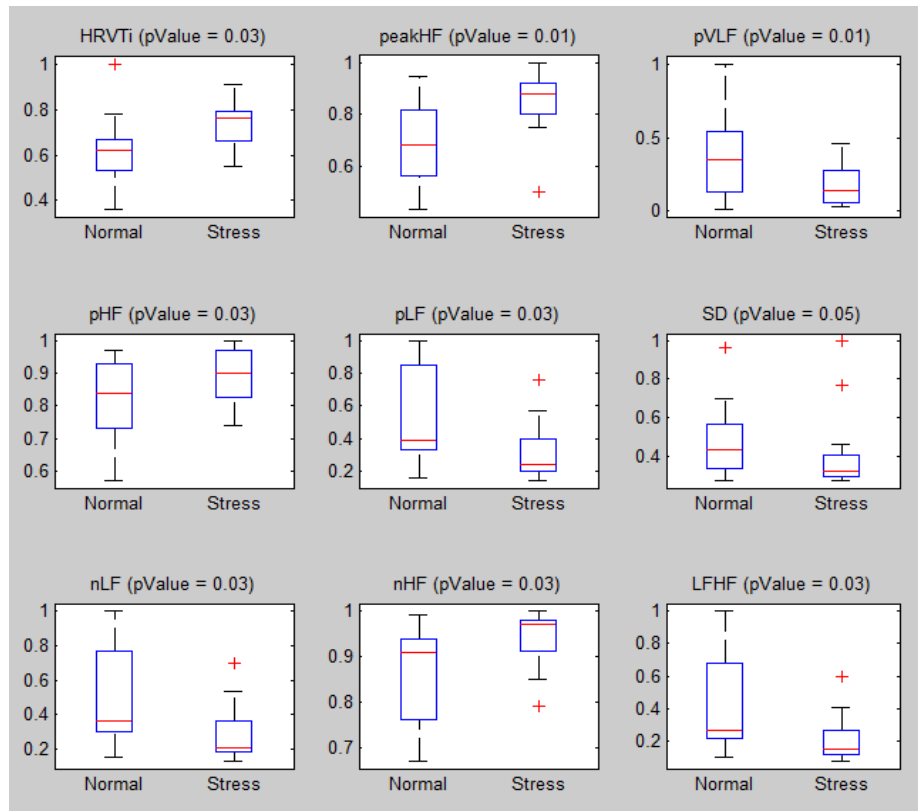


Figure 21: Box and whisker plots showing the distribution of the relevant features (from 12 subjects) for the normal and stress states.

The relevant HRV-driven features from both ECG and facial videos were then used to answer the three questions (posed in the starting of this chapter), and determine the best classification algorithm which can be used for remote stress detection.

Stress Detection Results using ECG Data

To answer the first question (Which classifier performs best for stress detection using contact HRV-driven features?), we used ECG recordings from the experiment. Applying both LR and LDA, we discriminated normal states from stress states for the four

cases (with stress levels ranging from high to low). Figure 22 shows the ROC curves for each case using both classifiers.

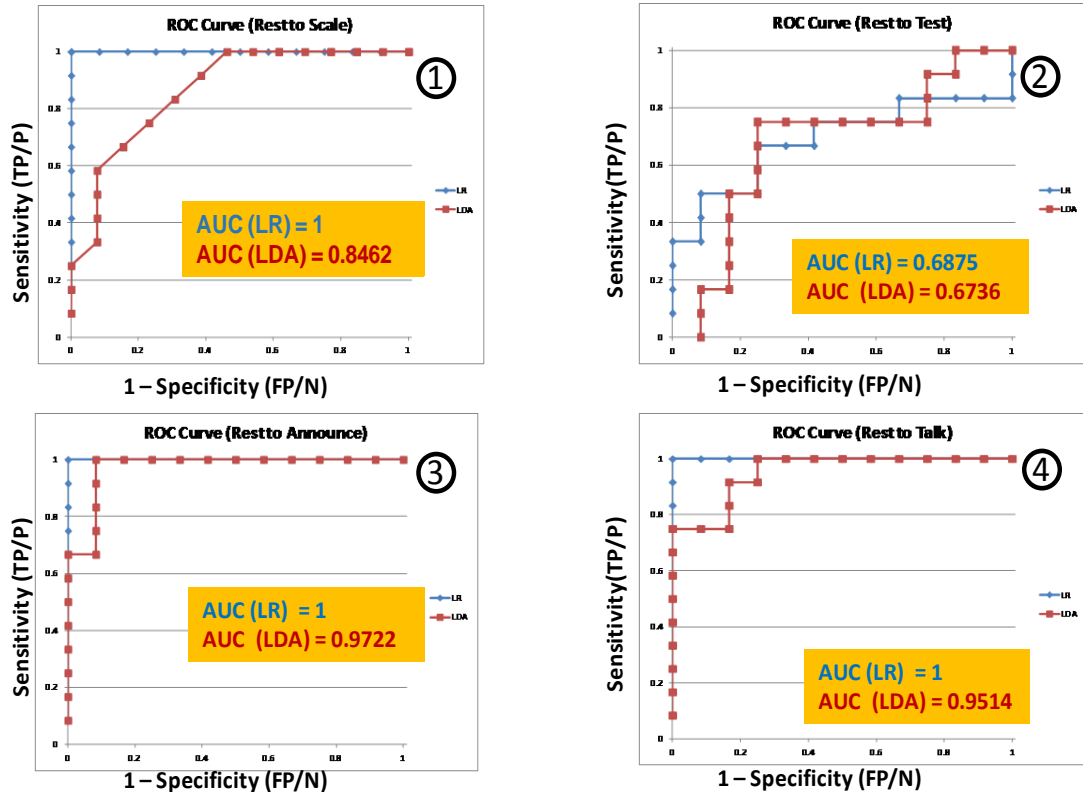


Figure 22: ROC curves for stress detection using logistic regression and LDA comparing: (1) rest with scale, (2) rest with test, (3) rest with announcement, and (4) rest with talk.

In summary, Table 2 shows the area under the curve (AUC) for all four cases using both LR and the LDA classifiers. Using LR, an AUC for the high (case 4) and mild (case 1, case 3) stress states was 1 and the low stress state was 0.686. Using LDA, an AUC for the high (case 4) and one mild (case 3) stress state was above 0.95, while one mild (case 1)

stress state was 0.846, and the low stress state was 0.686. Both classifiers were able to discriminate normal states from all levels of stress states, but clearly LR outperformed the LDA classification.

Table 2: Area under the curve for all four cases using LR and LDA

	Case 1 (Rest to Scale)	Case 2 (Rest to Test)	Case 3 (Rest to Announce)	Case 4 (Rest to Talk)
LDA	1	0.688	1	1
LR	0.846	0.673	0.922	0.951

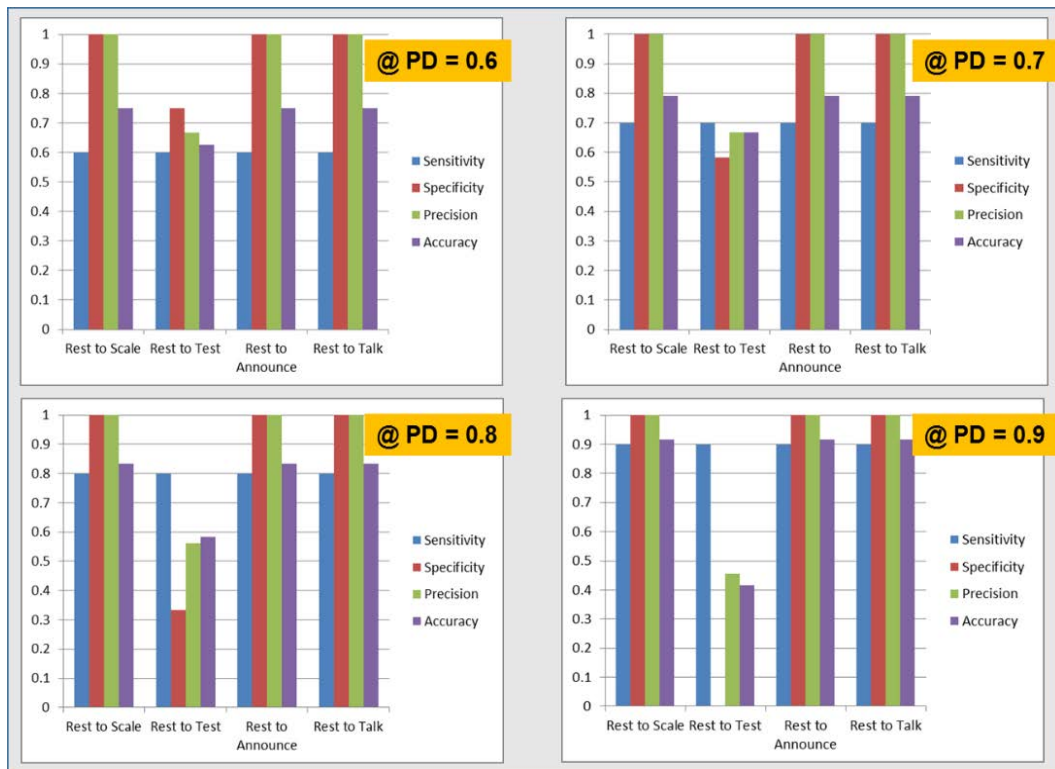


Figure 23: Bar charts with sensitivity, specificity, precision, and accuracy metrics for logistic regression classification for the four comparison cases of Figure 22.

Additionally, Figure 23 shows the metrics with four sets of bars representing the four cases of comparison between the normal and stress states at four sensitivity levels (PD-probability of detection). Within each set of the bars, one bar is for the sensitivity, one for the specificity, one for the precision, and one for the accuracy. Since we were interested in achieving the highest value for all the four quantifiable metrics for the most stressful case, in which resting state was compared with the state while delivering a speech (case 4). For this case, at sensitivity of 90%, we achieved a high level of specificity, precision, and accuracy (> 90%). Although human subject data analysis is always complicated and uncertain due to sensors, subjects, and environmental factors, we identified that the LR outperforms the LDA and classifies all levels of stress states from normal ones.

Stress Detection Results using VIS Data

To answer the second question (Will the best classifier be the best for stress detection using remote HRV-driven features?), we used remote HRV-driven features from experiment two. The features were computed from the RR-intervals generated from the peaks detected by our original zero crossings based algorithm. Applying both LR and LDA, we discriminated normal states from stress states for the first two cases. As expected, both LR and LDA helped with detecting high and mild levels of stress with high confidence. Figure 24 shows the ROC curves for these two cases using both classifiers.

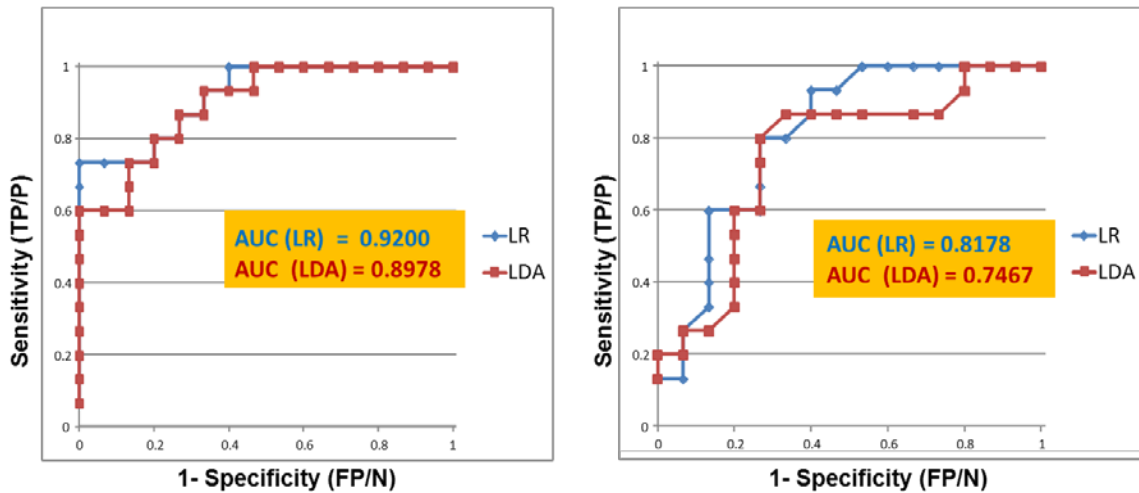


Figure 24: ROC curves for stress detection using logistic regression and LDA comparing: Normal with Stress1 and (2) Normal with stress2.

In summary, Table 3 shows the AUC for the two (high stress and mild stress) cases using both classifiers. Using LR, the AUC for the high stress state (case 1) was 0.920 and the mild stress state (case 2) was 0.818. Using LDA, the AUC for the high stress state (case 1) was 0.898 and the mild stress state (case 2) was 0.747. Both classifiers were able to discriminate normal states and stress states for both high and mild stress levels. Additionally, Figure 25 shows that for the high stress level case, at sensitivity of 70%, we achieved a high level of specificity, precision, and accuracy (> 80%). Similar to the LR's performance for stress detection based on contact HRV, LR outperforms the LDA classifier when the non-contact HRV data was used.

Table 3: Area under the curve for high and mild stress detection using LR and LDA.

Classifier	Case 1 Normal1 to Stres1	Case 2 Normal1 to Stres2
LDA	0.920	0.818
LR	0.898	0.747

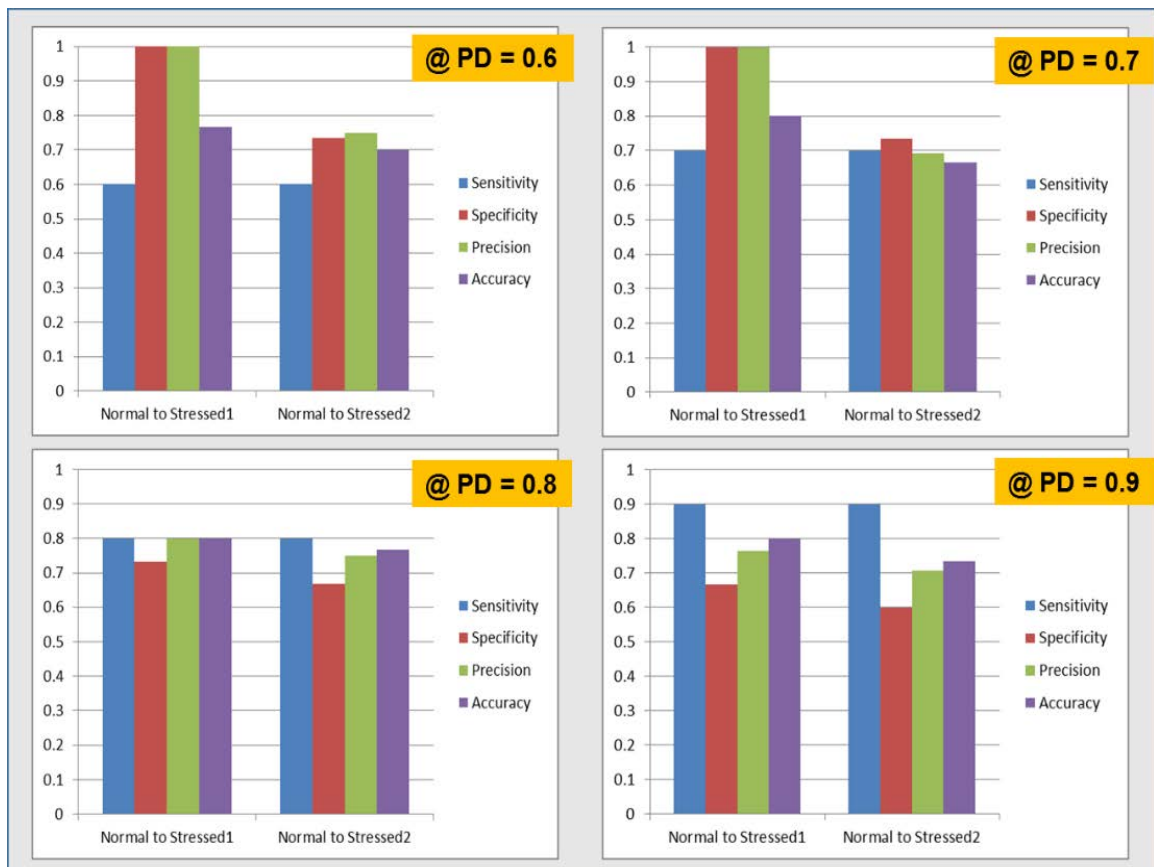


Figure 25: Bar charts with sensitivity, specificity, precision, and accuracy metrics for logistic regression classification for the two comparison cases of Figure 24.

Repeatable Stress Detection using VIS Data

Finally to answer the third question (Are the stress detection results repeatable with the best classifier?), we used remote HRV-driven features from experiment three. The features were computed from the RR-intervals generated from the peaks generated by the blind deconvolution based algorithm. Additionally, the HRV-driven features from the two states were corrected for a baseline. For each subject, a baseline for each HRV-driven feature was computed using a 30 second facial video segment from the first normal state. The HRV-driven features from the normal and stress states were then subtracted from the baseline HRV-driven features to generate the baseline corrected features. Applying the LR to these baseline corrected features from two cases, we then discriminated stress states from the normal ones. As expected, LR helped with detecting both levels of stress with high a confidence (Figure 26), with an AUC of 0.94 for the high stress level and 0.83 for the mild stress level. Additionally, Figure 27 shows that for the high stress level case, at sensitivity of 90%, we achieved a high level of specificity, precision, and accuracy (> 80%).

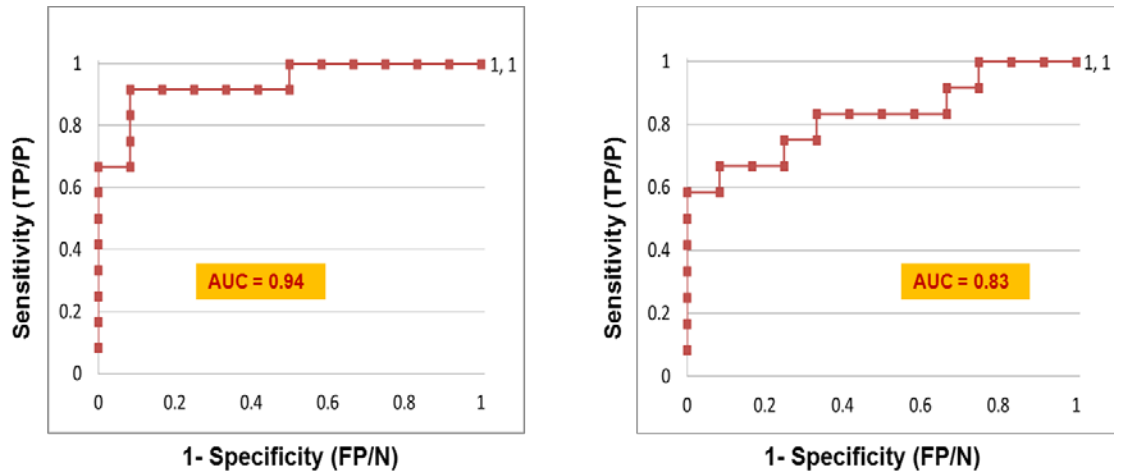


Figure 26: ROC curves for stress detection using LR comparing states: Normal with stress1 (left) and Normal with stress2 (right).

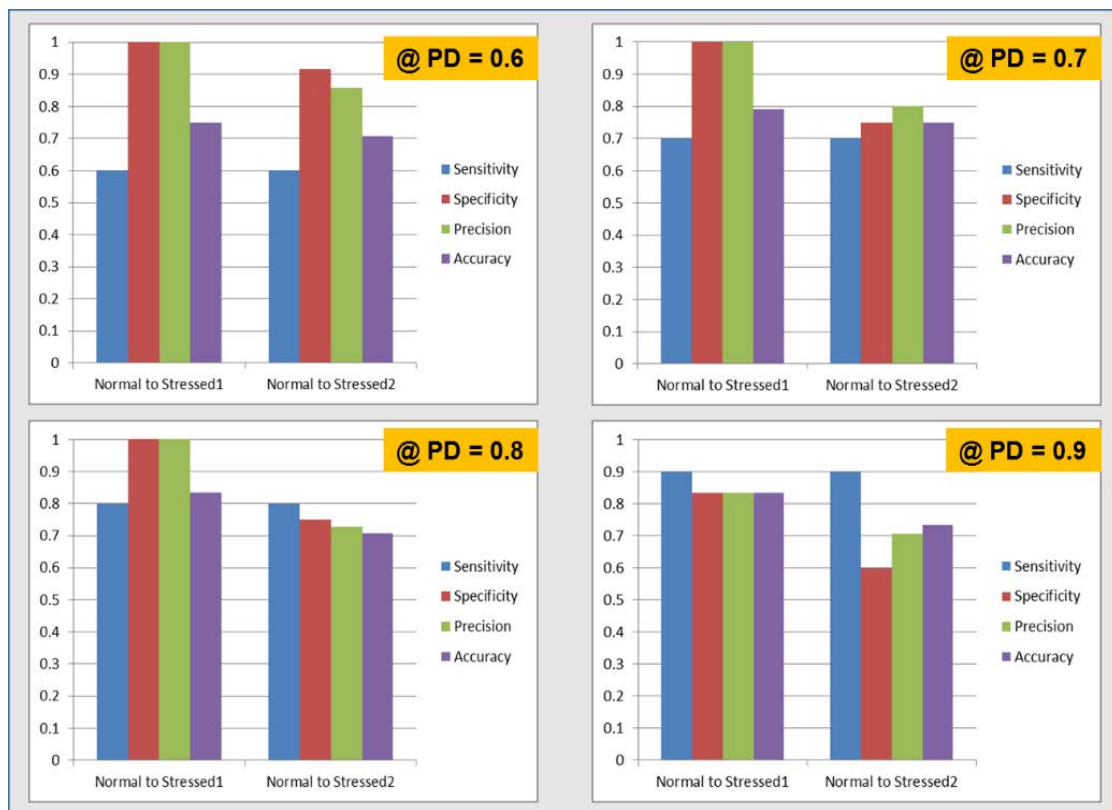


Figure 27: Bar charts with sensitivity, specificity, precision, and accuracy metrics for LR classification for the two comparison cases of Figure 26.

Improvements in Stress Detection Results

Figure 28 shows a comparison between the two ROC curves generated based on two approaches: S2014 – (green curve) RR-intervals generated with peaks detected by the zero crossings algorithm; S2015 – (red curve) RR-intervals generated with peaks detected by the blind deconvolution algorithm and HRV baseline correction. In addition to improvement in stress detection due to the cleaner RR-intervals driven from the blind deconvolution detected peaks and baseline correction of the HRV-driven features, plots clearly show the repeatability between the ROC curves for both stress levels. Additionally, at a specificity, precision, and accuracy of 80% for the high stress level, improved algorithms helped with increasing the sensitivity from 70% to 90%.

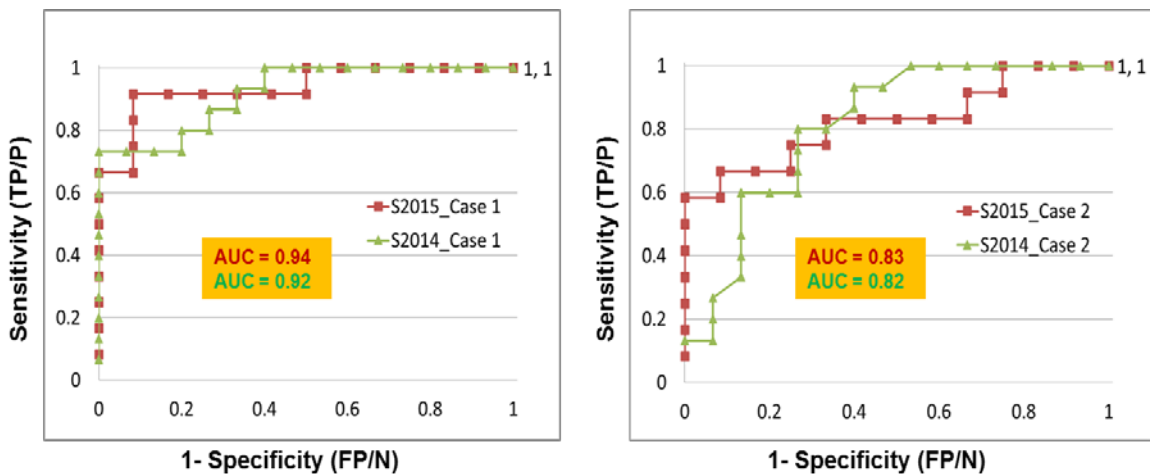


Figure 28: ROC curves for stress detection using LR with improved algorithms (red) and standard algorithms (green), comparing states: Normal with stress1 (left) and Normal with stress2 (right).

To show a better comparison between the two approaches, at the sensitivity level of 90%, we studied the likelihood of correctly detecting a stress state and generated truth tables (Table 4 and Table 5). Comparing the truth tables, the likelihood of correctly detecting a stress state improved when the blind deconvolution based detected peaks were used to determine RR-interval signals and the HRV-driven features were corrected for the baseline. For a high level of stress, it increased from 87% to 92%, and for a mild level of stress, it increased from 80% to 92%.

Table 4: The truth tables with stress detection results from remote HRV (12 subjects, experiment 2 with zero crossing based detected peak).					Table 5: The truth tables with stress detection results from remote HRV (15 subjects, experiment 3 with blind deconvolution based detected peaks and HRV baseline correction).						
Observations	Pd = 0.6 Ground Truth					Observations	Pd = 0.6 Ground Truth				
		Case 1		Case 2				Case 1		Case 2	
		Stress	Normal	Stress	Normal			Stress	Normal	Stress	Normal
	Stress	0.53	0.00	0.60	0.20		Stress	0.50	0.00	0.58	0.00
	Normal	0.47	1.00	0.40	0.80		Normal	0.50	1.00	0.42	1.00
Observations	Pd = 0.7 Ground Truth					Observations	Pd = 0.7 Ground Truth				
		Case 1		Case 2				Case 1		Case 2	
		Stress	Normal	Stress	Normal			Stress	Normal	Stress	Normal
	Stress	0.60	0.00	0.60	0.27		Stress	0.67	0.00	0.67	0.17
	Normal	0.40	1.00	0.40	0.73		Normal	0.33	1.00	0.33	0.83
Observations	Pd = 0.8 Ground Truth					Observations	Pd = 0.8 Ground Truth				
		Case 1		Case 2				Case 1		Case 2	
		Stress	Normal	Stress	Normal			Stress	Normal	Stress	Normal
	Stress	0.80	0.20	0.80	0.27		Stress	0.67	0.08	0.75	0.25
	Normal	0.20	0.80	0.20	0.73		Normal	0.33	0.92	0.25	0.75
Observations	Pd = 0.9 Ground Truth					Observations	Pd = 0.9 Ground Truth				
		Case 1		Case 2				Case 1		Case 2	
		Stress	Normal	Stress	Normal			Stress	Normal	Stress	Normal
	Stress	0.87	0.27	0.80	0.33		Stress	0.92	0.42	0.92	0.67
	Normal	0.13	0.73	0.20	0.67		Normal	0.08	0.58	0.08	0.33

Overall, our studies show a proof of principle that the LR classifier, when used with the improved algorithms (BDC and baseline correction), would classify high and mild levels of stress states with a high confidence.

Discussion

In this work, we were able to demonstrate that it is possible to use the HRV analysis of remotely detected HR information for physiological stress detection. This is based on the combination of two well-known techniques: the remote detection of cardiac pulse wave through skin color changes during the cardiac cycle, and HRV analysis techniques used for stress detection. Although, it is not an optimal solution, using LR classifier, at a sensitivity level of 90%, we were able to achieve the specificity, precision, and accuracy of above 82% for the high stress state and 62% for the mild stress state. Additionally, a likelihood of being correct for stress detection was noted to be above 92% for both high and mild stress levels.

However, this work was not without challenges. Our initial RR-intervals generated from the remotely acquired BW signals based on zero crossings were noisier as compared to the RR-intervals generated from the ECG signals, which resulted in compromised statistics. Therefore, the first step in our analysis was to extract a reliable RR-interval time series. To generate cleaner RR-intervals, we used the peaks detected by the BDC algorithm (developed in Chapter Three), which were highly correlated with the GT peaks. These RR-intervals were much cleaner as compared to our original RR-intervals. As a result, we noticed an improvement in stress detection for both high and mild stress levels. For a high

level of stress, it increased from 87% to 92%, and for a mild level of stress, it increased from 80% to 92%.

HRV analysis was performed using a variety of state-of-the-art HRV descriptors, as implemented in the HRVAS software package. HRV analysis makes use of a large number of different statistical descriptors from the areas of time-domain, frequency domain and nonlinear dynamics. However, not all were relevant to our classification problem. Following the HRV-driven feature selection procedure described in the methods section, nine stress significant features were identified. Most of these features were based on low and high frequencies of the RR-interval signals and were in agreement with the literature [10], [112]. These selected features were then weighted and combined to classify stress states from the normal ones using the logistic regression classifier.

The physiological response decreases due to the habituation when a stressor is introduced more than once. As a result, the difference between the HRV-driven features from two physiological states becomes less significant. We noticed this effect in our analysis as well (Figure 28, red curves): the AUC for the high stress level case, in which the stressor was introduced for the first time, was 0.94, and for the mild stress level case, in which the stressor was introduced for the second time, it was 0.83.

Overall, our study demonstrates that HRV-based analysis of a video-based estimation of the BW signals can be used for stimulus-based acute stress detection, using short-time recordings (30 second). While further research is needed to improve both

acquisition and data processing strategies, we believe that our study shows the potential of a non-contact, possibly covert system for short-time stress detection.

CHAPTER FIVE: REMOTE MEASUREMENTS OF DIFFERENTIAL PULSE TRANSIT TIME AND ITS USE FOR STRESS DETECTION

Introduction

In this chapter, we investigate the possibility of detecting mental stress using a novel, contactless method. It is based on the pulse transit time (PTT), the time that is required for the blood wave (BW) to cover the distance from the heart to a defined remote location in the body. Loosely related to blood pressure, PTT is a measure of blood velocity, and is also implicated in the “fight-or-flight” response. We define the differential PTT (dPTT) as the difference in PTT between two remote areas of the body, such as the forehead and the palm. Using remote BW detection from visible spectrum videos, we built a system that remotely measures dPTT. We further show that the dPTT can be measured using this system and it responds to stress, and therefore, is a potential stress indicator. Human subject data from two separate experiments were used to initially establish the potential use of remote dPPT detection as a stress indicator.

In Chapter Three, the palm and the forehead were identified as the two distal locations with the highest SNR values (Chapter Three), hence they are chosen as the optimal locations for remote BW signal detection for the purpose of remote dPTT detection. Under this study, first we hypothesized that there will be a measurable phase

shift between the two cardiac pulse waves obtained at two distal locations, and the phase difference between these two waves can be used to determine dPTT; and second, that the dPTT will change significantly under the presence of mental stress, indicating that our measure can in principle be used as a mental stress marker in healthy individuals repeatedly. To prove these hypotheses, we detected BW signals with high SNR at forehead and palm locations, designed an algorithm to use the BW signals to determine dPTT, and compared the obtained dPTT values under stressed and non-stressed conditions from multiple experiments. A strong agreement between the dPTT values under the similar physiological states from two experiments confirm the repeatability of the dPTT metric under both normal and stress states.

Materials and Methods

This chapter has three major goals to describe: the first is to develop the method to determine dPTT remotely, the second is to use of dPTT for stress detection, and the third is to show the repeatability of dPTT for stress detection. Keeping these three goals in mind, we designed experiments to induce stress at various stress levels, and used the experimental setup discussed in Chapter Three to collect facial skin videos and ECG signals. A set of experiments that were conducted is discussed as below.

Experiments

To acquire remote heartbeat signal with high SNR values (from palm and forehead) under the stress and normal physiological states, and to explore their use for stress detection based on the dPTT, we conducted two experiments using an “Affective Stress Response

Test” (ASRT). For the experiments, participants were asked to sit in a chair 5 feet away from the camera, with their head leaning against their hand and facing towards the camera (Figure 29). Participants were asked to sit as still as possible, and look at a computer screen in front of them, while we recorded their facial videos and ground truth (ECG).



Figure 29: Subject positions during experiments with their hand leaning against head with and palm facing camera.

The first experiment was used to collect data from 15 subjects, in which subjects were asked to view a series of pleasant and unpleasant images. The images (stimuli) presented on the computer screen were a series of photos, alternating between cat photos and photos of dead people (chosen so as to make the participants feel uncomfortable). Three alternating sets of images were shown to capture human physiological responses under normal and stress states. The stimuli presented on the computer screen were 3 sets

of images, alternating between cat images and images of dead people for 1.5 minutes each. Total duration of the experiment was 10.5 minutes.

The second experiment was used to repeat the first experiment to collect data from 12 subjects. The experimental setup, and the stimuli presented on the computer screen were similar to the first experiment. The purpose of this experiment was to show that the dPTT measurements are repeatable for stress detection. In addition, during this experiment, we increased the resting intervals from 1 minute to 2 minutes to bring a subject's physiological state to "Normal". This change in the experiment was designed to measure the true response of ANS as the stimulus was introduced for the second time. The presentation lasted approximately 7 minutes, and included 3 sets of relaxing images with cats and 2 sets of disturbing images with dead body parts. Each set of the relaxing images lasted one minute. The first set of the disturbing images lasted one minute, and the last two sets of the disturbing images lasted 2 minutes each.

Both experiments were designed to induce multiple stress levels by presenting stimuli. Multiple levels of stress was induced by presenting disturbing images in multiple blocks. For the first time, when the disturbing images are presented, the physiological response is expected to be high, which means a high stress level; however, for the second or third time when the same stimulus is presented, due to habituation, the physiological response is expected to reduce, which means a lower stress level as compared to the first time. Collected data under both experiments were used to assess whether BW signals, as extracted from video recordings of face and hand, can be used for detecting dPTT, be associated with various levels of stress, and be used to prove repeatability of the dPTT

Remote Blood Wave (BW) Signal Detection

BW signals were obtained by first spatially averaging the image intensities within the specified ROIs over the facial and hand skin areas for video segments to construct raw signals, and then applying an IIR bandpass filter with a bandwidth range of 0.3-8Hz [7], [11] to the raw signals. Image intensities were averaged within small ROIs to avoid noise due to multi-pathways and to increase SNR of the remotely acquired BW signal. A bandpass filter was applied to remove baseline low frequency fluctuations and higher frequency noise. However, due to differences in melanin content at various body locations and the location of capillaries within the dermis, we needed to identify the optimal locations where the BW signal could be measured with high SNR. We selected forehead and palm for this study, which were identified (in Chapter Three) as the optimal locations to detect BW signal with high SNR values.

Differential Pulse Transit Time (dPTT) Computations

To prove our first hypothesis that the BW signals measured at two distal body locations have a phase difference, we used data from the first experiment collected under the first normal state and determined the dPTT values for each subject by identifying the peak position in the correlation function between the BW signals from the two optimal body locations (forehead and palm). However, two extra steps were necessary before the correlation measurement could take place. The first was the definition of the ROIs for detecting BW signals, and the second was the upsampling of the detected BW signals to overcome the 60 frames per second limitation of our camera.

As described, the first step was to define the ROIs for detecting BW signals from the identified body locations. While averaging the intensity signal over larger areas is acceptable if the target is the heart rate estimation from the BW signal, this approach leads to errors in the calculation of the dPTT values. The errors are due to the different arterial pathways in the adjacent areas. This error propagates further and results in a less accurate estimate of the dPTT. Our solution to this problem was to define smaller ROIs in both the palm and the forehead. To determine at least one BW signal with high SNR from each of the identified locations, we placed three ROIs at each location. These ROIs were placed manually on the body parts of interest by trained observers following landmarks such as eyebrow or finger position. Then, following the BW signal extraction method, BW signals were determined within each ROI.

The second step was to upsample the BW signals to overcome the 59.9 frames per second limitation of our camera. We upsampled both BW signals by a factor of 1000 by linearly interpolating between each pair of two consecutive points. A representative waveform and the time shift between the forehead and palm ROIs is shown in Figure 30.

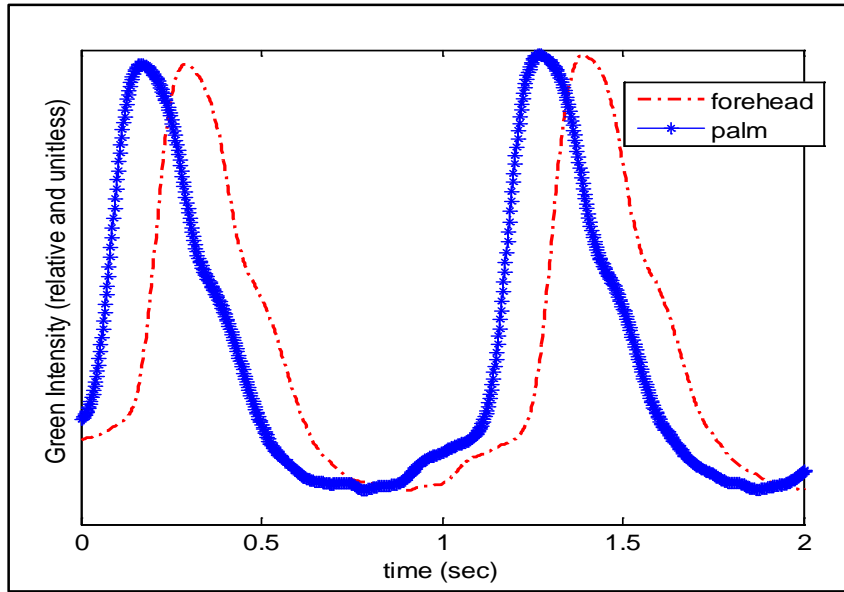


Figure 30: Typical averaged heart beat signals and their time shift between forehead (red dots) and palm (blue stars).

We used the phase shift between the two waveforms and calculated the dPTT as the time at which a peak occurs in the correlation function between the two up-sampled BW signals. First, BW signals were computed within each ROI placed on the forehead and the palm areas. Then the BW signals from the two locations were correlated and the dPTT values were computed. To validate the efficacy of the suggested method for computing the dPTT values, we used the human subject data from our first experiment and computed dPTT values for each subject.

Remote Stress Detection using dPTT

To prove our second hypothesis that the dPTT changes between normal and stressed states, we used the data from our first experiment. In order to test this hypothesis, we first calculated dPTT values for the time intervals corresponding to the normal (cat

photos) and stressed (dead body parts photos) states. To remove the transition effects between the two states (normal to stress or vice-versa), we ignored the first 30 seconds from each interval and then used a sliding window of 20 seconds over one minute duration to compute the dPTT value. The sliding window with a short duration was used to avoid the effects of signal averaging over the longer time period and to capture the physiological response at short duration intervals. To determine if there is a significant variability between the dPTT values of the normal and stress states, statistical analysis was performed by means of paired t-tests. To prove repeatability of the dPTT metric for stress detection, data from both experiments under both physiological states were used and compared.

Results

Data from first experiment, collected under first physiological normal state from each subject, was used to determine the range of dPTT. Following the methods for BW signal detection, these data were processed to determine BW signals within the ROIs placed on the forehead and palm locations, which were then used to determine dPTT values. As shown in Data analysis shows that the dPTT values under normal physiological states range from 6 ms to 30 ms (Figure 31).

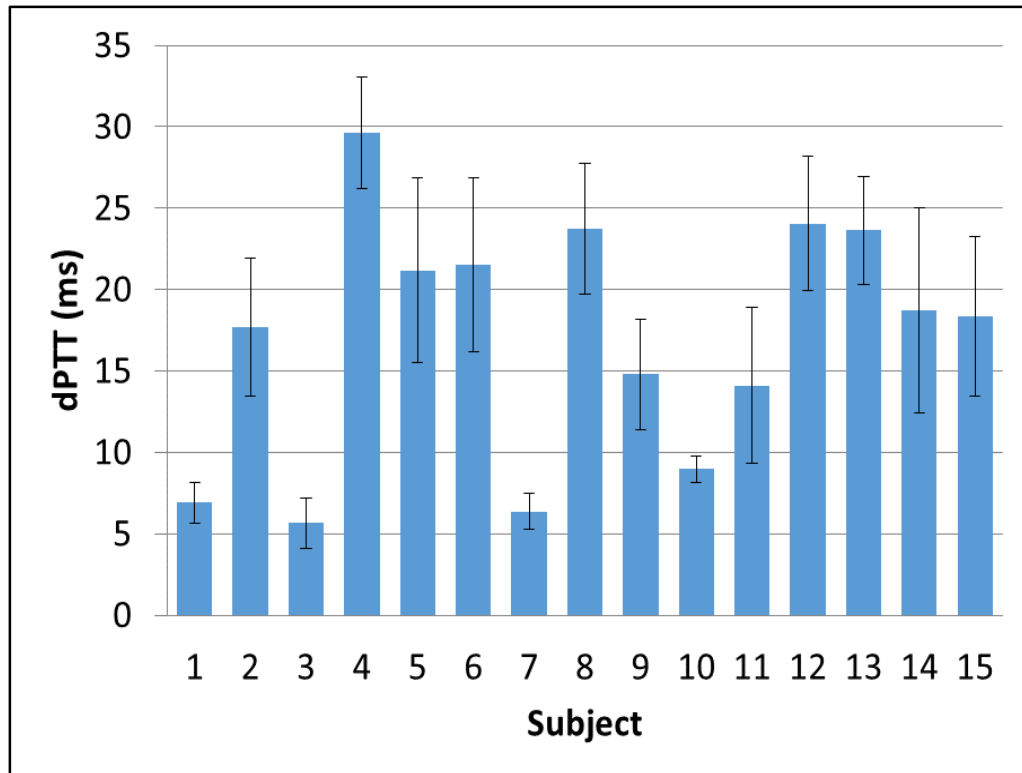


Figure 31: Average dPTT values (Experiment one, first normal state, 15 subjects).

We then used facial and palm videos from the both experiments and computed dPTT values under both normal and stress states. Figure 32 and Figure 33 show that the average dPTT values for all stress states (S1, S2 & S3) are higher than the first normal state (N1), which indicates the effect of stimulus on the dPTT value. Further, a lower dPTT value for all the normal states (N1, N2 & N3) preceding the stress states (S1, S2 & S3) indicates the dPTT response to the ANS.

Furthermore, to show a significant difference between the dPTT values measured during the normal and stress mental states, a statistical analysis was conducted and p-values were computed for the three cases: case 1- first normal (N1) state compared with the first

stress state (S1); case 2- first normal (N1) state compared with the second stress state (S2); case 3- first normal (N1) state compared with the third stress state (S3). Using data from both experiments, p-values for each case were computed with the highest significance for case 1 (p-value < 0.05). Case 1 from experiment one had a p-value of 0.009 and from experiment two had a p-value of 0.007. In experiment one, significance for the second and the third case was not as high because the resting time period between the states was short. However, for the second experiment, we increased the resting duration for N2 from 1.5 minutes to 2 minutes and as a result achieved a higher significance (0.007).

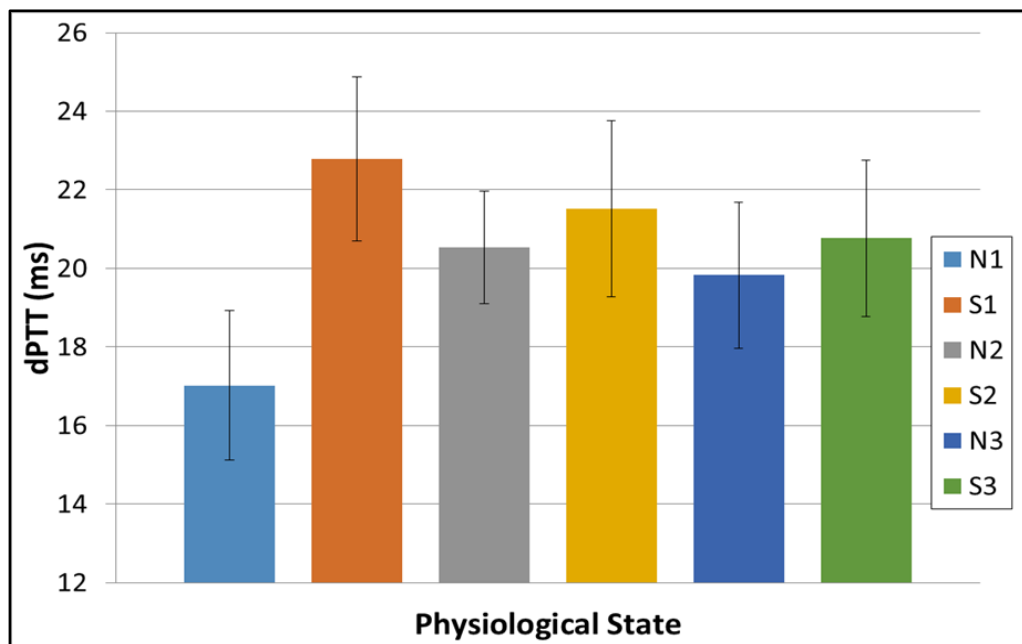


Figure 32: Average dPPT value distribution for the normal and stress states using data from experiment one (15 subjects).

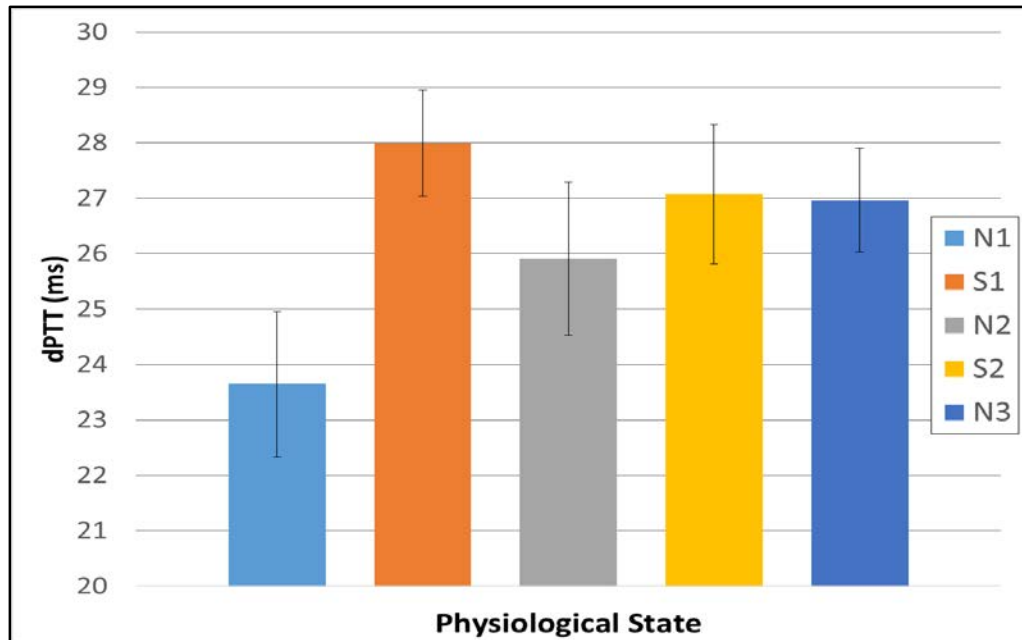


Figure 33: Average dPPT value distribution for the normal and stress states using data from experiment two (12 subjects).

In addition, the paired plots (Figure 34 and Figure 35) show significant difference in dPPT values between the physiological states (especially between the first normal and stress states). As expected, the plots show that the dPPT values for majority of the subjects increase when a stressful stimulus is introduced for the first time (S1). Some subjects show no change in the dPPT values and some subjects show an opposite response. Diversity in the results show that the dPPT values cannot be generalized for each subject, and therefore, identifying a baseline for each subject would help with the use of this newly developed metric (dPPT) for stress detection.

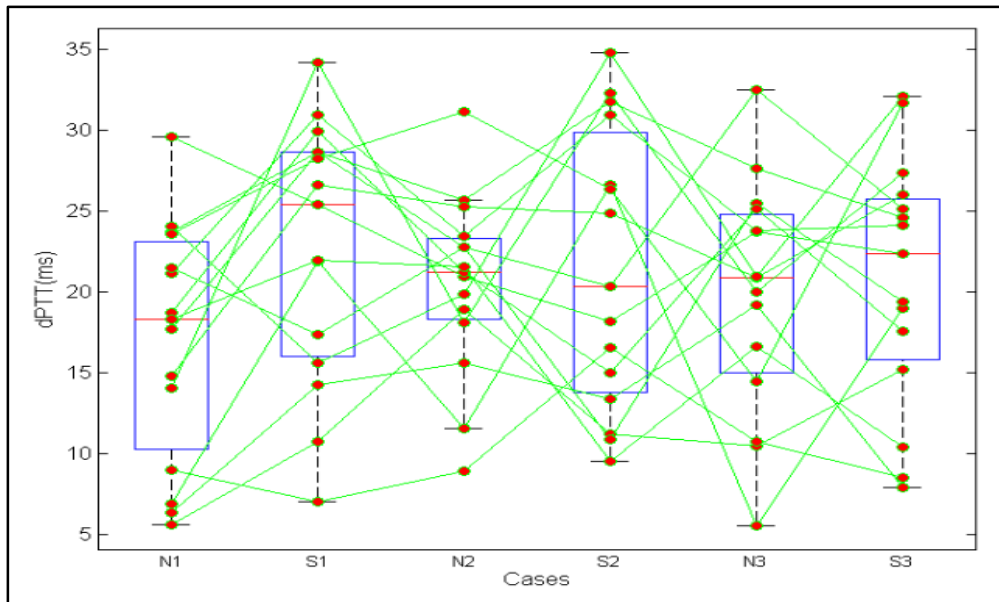


Figure 34: Paired plots showing the dPTT values from all subjects for the three normal and three stress states, and their relationship between states under the second experiment.

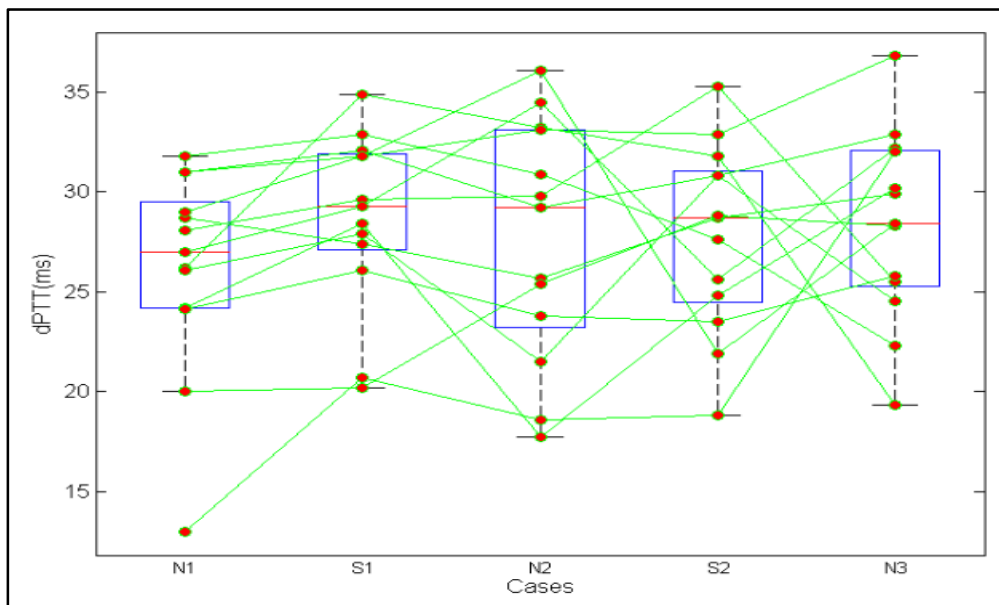


Figure 35: Paired plots showing the dPTT values from all subjects for the three normal and three stress states, and their relationship between states under the third experiment.

Discussion

In the literature, dPTT has been measured based on the difference in arrival time of the heartbeat signals measured at two body locations (e.g., finger, chest, ear, etc.) using contact sensors [113], [114]. In our study, we expanded on this by detecting dPTT remotely, based on the phase shift in heartbeat signals measured at two distal body locations (face and palm) in visual spectrum camera recordings, and showed that this remotely detected dPTT metric can be used as a basis for remote stress detection. Remote dPTT detection posed challenges, mainly due to the low SNR of the BW signals, different pathways, and multiplicative noise.

Defining small and repeatable ROIs to determine BW signals from the facial and palm skin areas with high SNR was essential for our experiments. While averaging over a large ROI helps with determining a BW signal with high SNR, the phase shift between the two BW signals acquired from large ROIs in two distal locations proved an unreliable measure. This was attributed to the presence of phase differences within adjacent skin areas, especially in the palm, possibly due to different arterial pathways in those areas. We acquired BW signals with high SNR by first designing experiments to ensure minimal subject motion without introducing any additional stress to the subjects, and then defining small ROIs to avoid averaging over multi-pathways.

Remote BW signal is likely to exhibit multiplicative noise, mainly due to flickering of the illumination source, natural human motion, and respiration. In our collected data, we noticed some flickering at a frequency of ~ 1 Hz, which corresponds to the intensity

fluctuation envelope of CFL bulbs [115]. In some cases this noise significantly impacted the BW signals. However, due to the multiplicative nature of this noise, the phase shift between the two BW signals acquired from two distal locations was preserved. As a result, even with the existence of some limited noise, we were able to compute dPTT for each subject. However, the presence of flickering may rise to levels where it may overwhelm the measurement of the phase shift, and needs therefore to be taken into account in system design.

Despite various challenges, we were able to show that it is possible to measure phase shift between the BW signals acquired from two distal locations (dPTT) that we believe to be related to the pulse transit time. We have further shown that the dPTT changes with the stimuli and therefore can be used as a potential stress indicator. In the literature, PTT has been correlated with blood pressure [66] [67], which also relates to stress [78], [79]. In the past, dPTT has been measured using contact sensors; however, we have for the first time measured the dPTT remotely. We believe this remotely measured dPTT metric has a potential as a stress indicator. We believe that a higher confidence in remote stress detection can be achieved if used in conjunction with the other stress markers such as heart rate variability (HRV) [23]–[26] and sweat gland pore response/Galvanic Skin Conductance [27], [28], [54], resulting in a video-based contactless stress detection system.

CHAPTER SIX: ROBUSTNESS OF REMOTE STRESS DETECTION FROM VISIBLE SPECTRUM VIDEOS

Introduction

In Chapter Three, we have shown that it is possible to extract high fidelity timing information of the cardiac pulse wave from visible spectrum videos, which can then be used as a basis for stress detection (Chapter Four and Chapter Five). In that approach, we used both heart rate variability (HRV) metrics and the differential pulse transit time (dPTT) as indicators of the presence of stress. One of the main concerns in this analysis is its robustness in the presence of noise, as the remotely acquired signal that we call blood wave (BW) signal is degraded with respect to the signal acquired using contact sensors.

Remote HRV and dPTT measurements depend on the heartbeat signals measured from video recordings based on the skin color variations (image intensity), which may change due to illumination changes. Illumination levels may change as a result of light flickering and slight motion due to respiration. The image intensity is a multiplication of illumination and reflectance [116], and therefore, a change in illumination would introduce multiplicative noise.

In this chapter, we discuss the robustness of our metrics (HB, HRV, and dPTT) in the presence of multiplicative noise. Specifically, we study the effects of subtle motion due

to respiration and changes in illumination levels due to light flickering on the BW signal, the HRV-driven features, and the dPTT. Our sensitivity study involved both Monte Carlo simulations and experimental data from human facial videos, and indicates that our metrics are robust even under moderate amounts of noise. Generated results will help the remote stress detection community with developing requirements for visual spectrum videos based stress detection systems.

Since multiplication changes the frequency contents of a signal, this introduces an error in the estimation of signal timing. This is supported by our observation that the fundamental frequency of the remotely acquired heartbeat signals were slightly different from the GT, and as a result, there was a non-zero average error in the estimation of the peak position when compared to the ground truth (GT) ECG signal. This type of noise cannot be reversed by means of conventional filtering.

Because HRV can be regarded as changes in the phase of the heart rate (HR) signal, we are expecting the effects of multiplicative noise to be limited. This is based on similar results from communications theory, which have shown limited effects of multiplicative noise on phase modulated systems [117]. Therefore we expect at least a subset of the metrics used in our stress detection system to be unaffected by such noise. The aim of this study is to identify metrics related to HRV and dPTT that are robust in the presence of multiplicative noise.

We focus on multiplicative noise introduced by two common factors: respiration motion and light flickering. First, we compare the fundamental frequency and the peak

locations of BW signals when the signal is subjected to multiplicative noise of various SNR levels. Second, we test the hypothesis that, because multiplicative noise should affect the BW signal in two different distal body locations in a similar manner, effects on the dPTT metric should be minimal. Third, because HRV is a metric of phase differences between subsequent heart beats, and we expect these phase shifts to be relatively robust to multiplicative noise, we hypothesize that some HRV features will be relatively unaffected by the presence of such noise. To prove this, we conducted sensitivity studies using both Monte Carlo simulations and experimental data from human facial videos and tested for accuracy of the BW signal peaks, the dPTT, and the HRV-driven features (significant for our stress detection application) under the effects of light flickering and respiration motion.

Methods and materials

This chapter's goal is to conduct sensitivity studies, to show the minimal effects of multiplicative noise (light flickering and respiration motion) on the BW signal peak locations and the fundamental frequency, the dPTT, and the HRV-driven features (significant for our stress detection application). To show, we simulated BW signals and used the facial and palm skin videos from the second experiment of Chapter Five, and conducted sensitivity studies following the methods presented in this chapter.

Remote Blood Wave (BW) Detection

BW is the remotely measured heartbeat signal. These signals are constructed from the facial and palm skin videos based on the minor intensity fluctuations (Kaur et al. 2014a). Following the methods in Chapter Three, BW signals were determined for the

experimental data under each physiological state. The fundamental frequency of a BW signal was determined using the Fast Fourier Transform (FFT), and the peaks were determined employing the blind deconvolution (BDC) algorithm presented in Chapter Three.

Remote Differential Pulse Transit Time (dPTT) Estimation

We define the dPTT as the difference in the pulse arrival time between two remote areas of the body, such as the forehead and the palm. Following the methods in Chapter Five, we processed experimental data to determine dPTT from each subject under the first normal condition. In Chapter Five, we have demonstrated the potential use of this metric for remote stress detection, as well.

Remote Heart rate variability (HRV) Feature Generation

Conventionally, the RR-interval is the interval from the R-peak of one QRS complex to the R-peak of the next QRS complex (in ECG signal). We use the BW signal peaks, as determined by a blind deconvolution algorithm, to estimate the RR-intervals and construct an RR-interval signal. These signals are then used to compute remote HRV-driven features that were relevant for stress detection (identified in Chapter Four). These features were: HRVT_i, SDNN_i, pVLF, pLF, pHF, and nHF (definition in Table 1). In Chapter Four, we have demonstrated that the variability in these features can be used for discriminating two physiological states (stressed and normal).

Simulated Data

To study the effects of multiplicative noise on the metrics of our interest, we simulated 120 BW, noise, and noise modulated signals, of which 40 were simulated at 60 ± 1 bpm, 40 at 80 ± 1 bpm, and 40 at 100 ± 1 bpm. To generate realistic BW signals, the impulse trains constructed at the identified fundamental frequencies were convolved with a Gaussian kernel with $\sigma = 0.1$. The multiplicative noise signals ($m[n]$) were simulated as sinusoidal waves superimposed on a DC component, which represents the ambient illumination. The model used to simulate such a signal is shown below:

$$m[n] = A + B \sin[2\pi f_m n] \quad (31)$$

Where, f_m is the fundamental frequency of the noise signal (0.3 Hz for the respiration motion and 1 Hz for the light flickering); A is the DC level, representing the average ambient illumination level, at which the noise signal resides; B is the amplitude of the noise signal.

The amplitude (B) of the noise signal was varied to achieve various levels of light to noise ratios (LNR) values. We defined the LNR as a ratio of the DC component over the noise amplitude ($LNR = A/B$). Since the signal $m[n]$ can be perceived as the illumination pattern measured on a white reference background, we processed white reference videos to measure LNR values. In our experimental data, the lowest LNR observed was 8 in the presence of particularly bad light flickering; normal SNR values were in the order of 10000. For our simulations, the LNR ranged from 1 to 36.

The simulated BW signals were multiplied with the noise signals to determine noise modulated BW signals. Both the BW signals and the noise modulated signals were then used to test the robustness of the HB signals, dPTT, and the HRV-driven features.

Robustness of the BW Signal

To test the robustness of a BW signal under the effect of multiplicative noise, we used the simulated BW and noise modulated BW signals and computed HR and peak locations. Both HR and the peak locations from the simulated and the noise-modulated signals were compared using absolute normal error. Figure 36 shows an example of a simulated BW signal (in black), a multiplicative noise signal due to light flickering (in green), and the noise-modulated BW signal (in red). The plot shows a clear shift in noise-modulated signal peaks (red) from their original locations in BW signal (black).

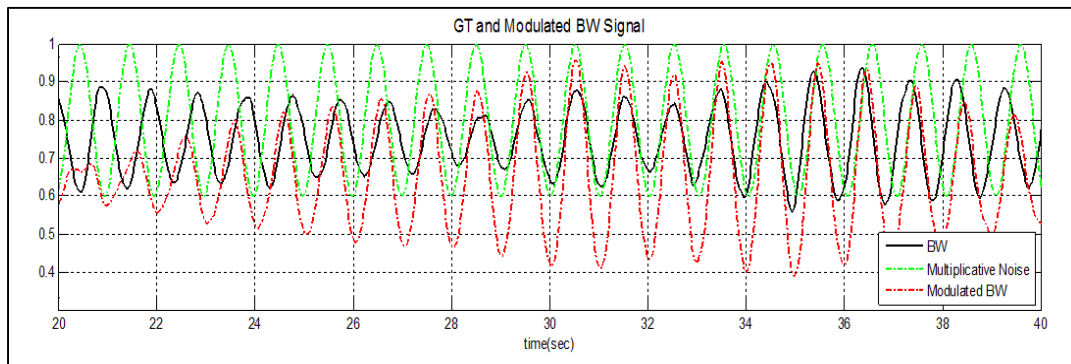


Figure 36: An example with the flickering noise (1 Hz): simulated BW (black), flickering noise (green), and noise-modulated BW (red) signals.

Robustness of the dPTT Metric

The differential pulse transit time (dPTT) is computed as the difference in arrival time of the BW signal at two distal body locations, which can be regarded as a phase difference between the two BW signals. Hence, we conducted a sensitivity analysis to test if a phase shift between the two signals changes as a result of the multiplicative noise and if it does, then by how much.

To study the effects of this shift, we added different values of phase shift to each simulated BW. The phase shift range was determined based on our dPTT studies [6], in experimental data from 12 subjects under the first normal and stress states and measured dPTT between 3ms to 30 ms. To cover the observed dPTT values, we tested phases between 1 ms and 40 ms. The noise signals at various SNR levels were also constructed following the method in the *Simulated Data* section. Then the noise modulated signals for each simulated and phase-shifted BW signal were constructed by multiplying them with the noise signals. A phase shift between the noise modulated BW signals was then determined for each pair and compared with the phase shift of the signals without the noise by means of the absolute normal error. A small value of the absolute normal error would show the minimal impact of the multiplicative noise on the dPTT metric.

Robustness of the HRV-driven Features

To study the robustness of HRV-driven features that are significant for stress detection, we used both experimental and simulated data. The experimental data from the first normal and stress states were used to determine the stress significant (relevant) HRV-

driven features based on a paired t-test between their values from the two states [5] . The HRV-driven features with the p-value <0.05 were identified as the relevant features for stress detection. An absolute difference for each identified relevant feature was determined, and a threshold value was identified (at 50% and 25%) to test the robustness of the associated features in the presence of multiplicative noise.

Simulated data were used to test the robustness of the relevant HRV-driven features under the effect of respiration motion and light flickering. RR-interval signals were generated, using our blind deconvolution algorithm, from each BW and noise-modulated signal, and were then used to determine relevant HRV-driven features. For each relevant feature, we computed the absolute difference between the simulated and the noise-modulated pairs. The difference from each relevant HRV-drive feature was then plotted and compared against the identified threshold values. Instead of choosing only mid-points (at 50%) of the relevant features as the threshold values, we chose another threshold value which was below the mid-point (at 25%). The reason for selecting a second lower threshold values was that a stimulus might not be as strong as we used in our experiments (disturbing images), which will result in a smaller difference between the HRV-driven features under two physiological conditions. The HRV-driven features with their average absolute difference below the specified threshold values (at all LNR levels) were identified as the robust HRV-driven features in the presence of the tested multiplicative noise.

Results

Applying the method discussed in the *Simulated Data* section, we constructed simulated and noise-modulated BW signals and conducted a sensitivity analysis to study the effects of respiration motion and flickering noise on the estimated HR and signal peak locations as a function of the simulated signal's LNR. In the presence of both the respiration and the flickering noise, a maximum absolute normal error for the HR was determined to be $<0.1\%$. In the presence of multiplicative noise (either respiration motion or light flickering), the absolute error between the simulated and noise modulated BW signals, at the commonly observed SNR values in our BW signals ($\gg 30$), was noted to be $< 1\text{ms}$. Figure 37 and Figure 38 show the absolute normal errors (blue dots) between the simulated and the noise modulated BW signals at various LNR levels. The black line in the plots is the polynomial fit to the data (blue dots) showing the average trend of the absolute normal error over the range of LNR values. Clearly, at the higher LNR levels, the plots show a minimal effect of the respiration motion and the light flickering on the peak locations. The range of the absolute normal error values in peak detection implies that the detected BW signal peaks would be slightly off from the ground truth peaks under the presence of the flickering and the motion noise.

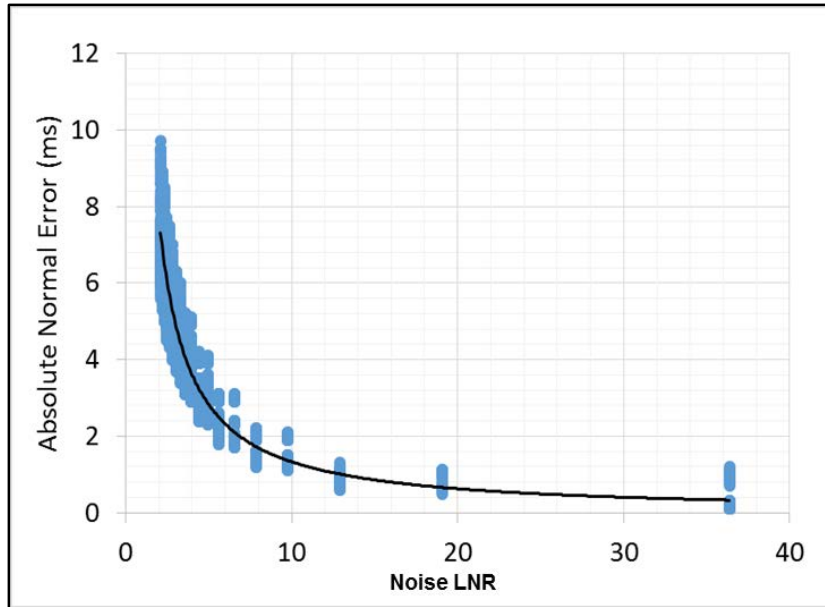


Figure 37: The plots showing the absolute error between the peaks of the BW and the noise-modulated BW signals over a range of noise LNR values due to respiration motion.

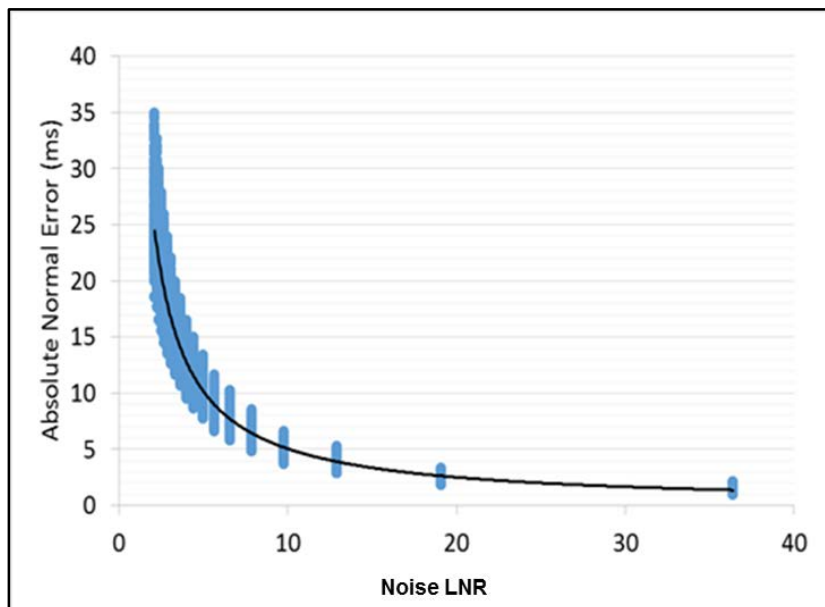


Figure 38: The plots showing the absolute error between the peaks of the BW and the noise-modulated BW signals over a range of noise LNR values due to light flickering.

Applying the methods discussed in the dPTT section, we constructed simulated BW signal pairs, one with and one without a phase shift. Then the multiplicative noise was applied to both signals and a phase shift between the two noise-modulated signals was determined for each set. The absolute normal error between the phase shifts of the original and the noise-modulated signals was computed, and as expected, for both respiration motion and light flickering noise; even in the worst case scenario (LNR = 1), the error was negligible ($< 0.0008\%$). The simulation results imply that the phase shift between the two signals acquired from two distal body locations is not affected in the presence of the tested multiplicative noise. In other words, the dPTT metric is robust to the presence of respiration motion and light flickering noise.

Following the method in the HRV analysis section, we studied the effects of respiration motion and flickering noise on the stress significant HRV-driven features. A list of stress significant features identified based on the experimental data analysis is shown in Table 6. Figure 39 shows the normalized absolute difference between the average values from the first two physiological states (stress and normal), with the mid-point (red star) and below mid-point (black star) as the thresholds for that feature. To discriminate a stress state from a normal state with high confidence, a large threshold value is desirable.

Table 6: A list of significant HRV-driven features that can be used for stress detection.

Features	Description
HRVTi	HRV Triangular Index (D(t)/Y) D(t) = density distribution of the histogram of RR-interval Y = maximum value of D(t)
pVLF (%)	Percentage of the sum of absolute very low frequency (0.003-0.05 Hz)
pLF (%)	Percentage of the sum of absolute low frequency (0.04-0.15 Hz)
pHF (%)	Percentage of the sum of absolute high frequency (0.15-0.4 Hz)
SD (ms)	Standard deviation
LFHF	The ratio of LF to HF
nLF (%)	Normalized to total power low frequency
nHF (%)	Normalized to total power high frequency
peakHF (HZ)	Peak of the high Frequency

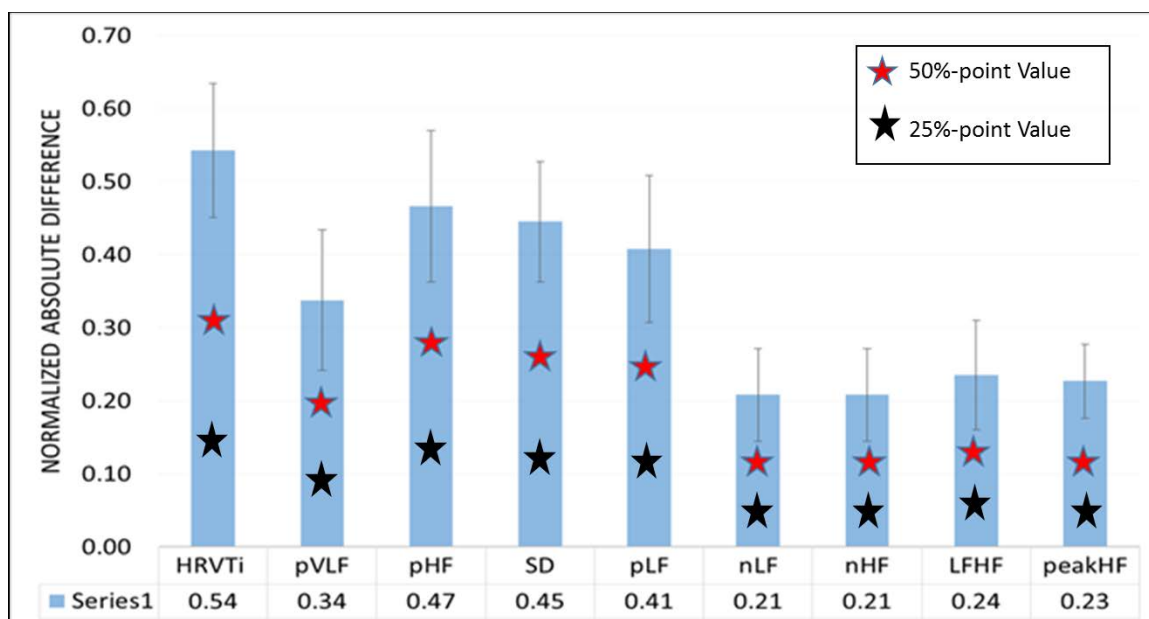


Figure 39: Plot showing the normalized absolute difference between the normal and stressed states for the identified relevant HRV-driven features, with red stars showing mid-point value and black star with below the mid-point value for each feature.

Following the method suggested in the HRV section, we simulated BW and noise modulated BW signals, processed them to generate relevant HRV-driven features, and then computed absolute normal error between the HRV-driven features from the signals with and without noise. Figure 40 and Figure 41 show the box and whisker plots with the Monte Carlo simulation results for the respiration motion and the light flickering noise respectively. Clearly, both Figure 40 and Figure 41 show that the average difference of HRVTi, SDNNi, pVLF, pLF, pHF, and peakHF are below the associated 50% threshold value, and pLF and peakHF are below the 25% threshold value, and therefore, these features should be robust under the effect of the multiplicative noise introduced by respiration motion and light flickering.

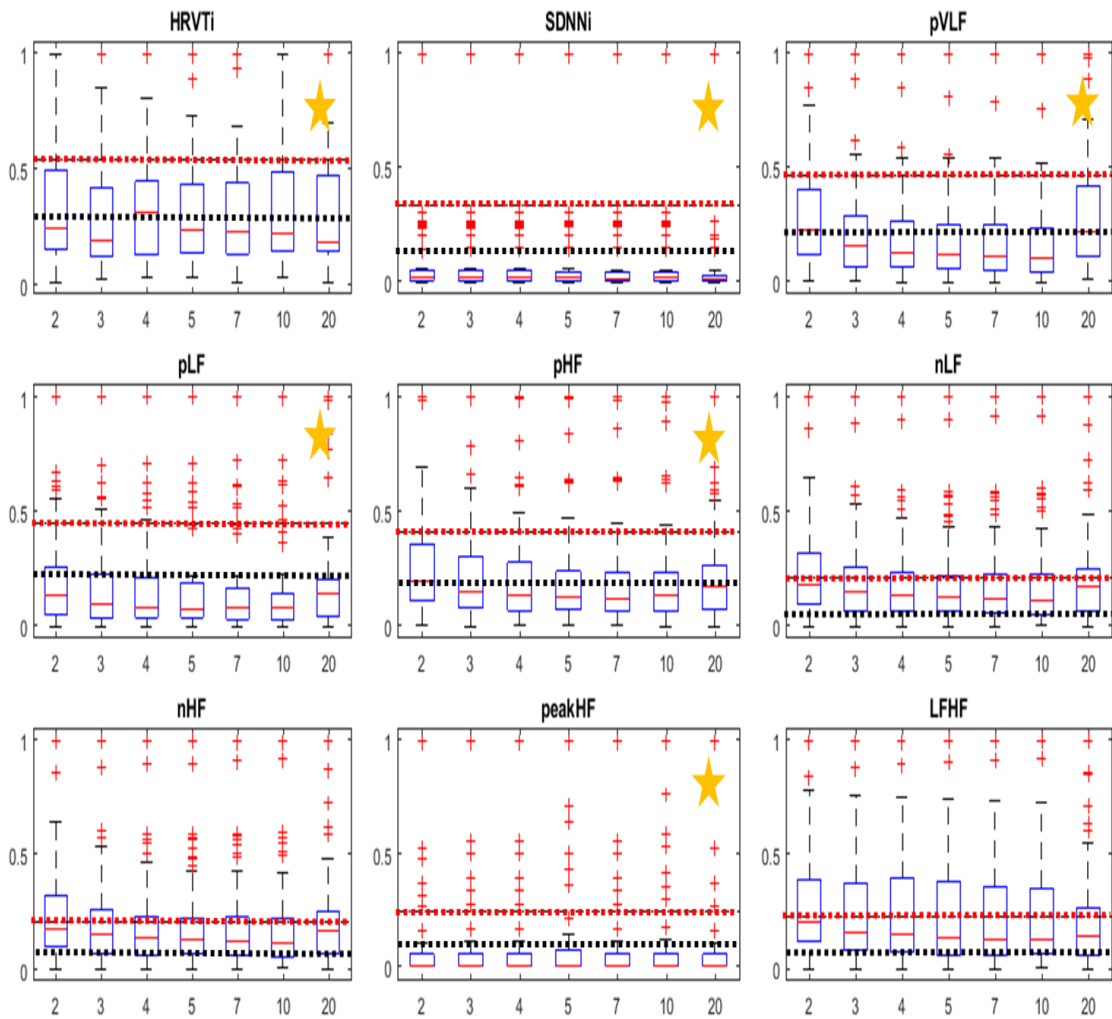


Figure 40: The box and whisker plots of relevant HRV-driven features with the absolute normal difference between the simulated and noise-modulated (respiration noise) signals with the thresholds for each (red and black horizontal dotted line).

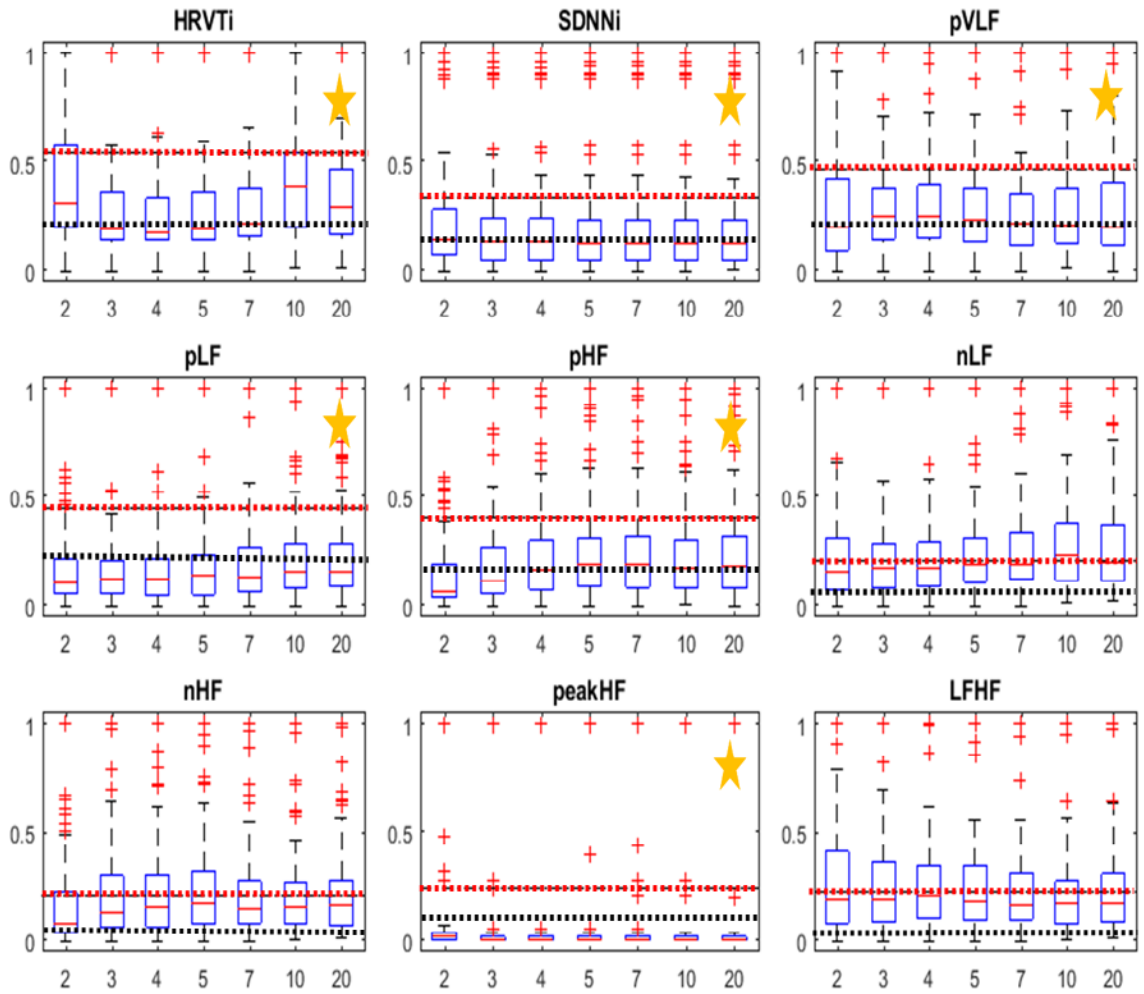


Figure 41: The box and whisker plots of relevant HRV-driven features with the absolute normal difference between the simulated and noise-modulated (flickering noise) signals with the thresholds for each (red and black horizontal dotted line).

Discussion and Conclusions

As stated in literature, the frequency content of a signal changes under the effects of multiplicative noise. Furthermore, our sensitivity analysis employing the Monte Carlo simulations verifies the effect as well. In the range of LNR values in our experimental

data, the simulations showed a minimal effect ($< 0.1\%$) of multiplicative noise on HR and minimal effect (< 1 ms) on signal peak locations (when compared with GT peaks). Overall, our simulation results show that a BW signal would be robust under the effects of multiplicative noise, especially from respiration motion and light flickering.

In terms of the dPTT, our results indicate that it is robust to multiplicative noise. This is in agreement with literature [117], which indicates that in the presence of multiplicative noise, the phase shift between the two signals should not be affected. For both respiration motion and flickering noise, our simulation results show a negligible absolute normal error between the phase shifts of the original and the noise-modulated signals. Therefore, we conclude that the dPTT metric is robust to respiration motion and flickering noise and thus can be used for stress detection with high confidence.

HRV analysis posed an interesting challenge. HRV analysis is the study of small timing differences in subsequent cardiac cycles, and as such can be approximated as a study of phase changes in the signal. In a manner similar to phase modulated signals, we expected at least part of this information to be preserved in the presence of multiplicative noise. However, since HRV analysis makes use of statistical descriptors whose behavior to multiplicative noise is unknown, we opted for studying their robustness using Monte Carlo simulations. These simulations covered LNR values much lower than what we saw in our experimental conditions, and showed that at least six stress significant features under the effects of a strong stimulus and at least two stress significant features under the effects of a mild stimulus, are robust under the presence of both respiration motion and flickering noise.

In this work, we have demonstrated that the BW signal, the dPTT, and a set of stress significant HRV-driven features are robust under the effects of respiration motion and illumination flickering noise. We believe that the HRV-driven features such as pLF, and peakHF, and the dPTT metric can be reliably used for stress detection applications in a remote video-based system.

CHAPTER SEVEN: CONCLUSIONS AND FINAL COMMENTS

Conclusions

Stress is a major health concern that not only compromises our quality of life, but also affects our health and well-being. Despite its importance, our ability to objectively detect and quantify stress in a real-time, non-invasive manner is very limited. Through the means of our dissertation research, we contribute to such a capability, by combining remote heart beat detection through a visual spectrum camera and heart rate variability analysis in order to develop a compact, low-cost and possibly covert system for detecting stress.

The research in this dissertation builds on two well-studied fields: remote detection of the blood wave (BW) signal using skin color variations on visible spectrum video (e.g., (Poh, McDuff, and Picard 2010; Poh, McDuff, and Picard 2011; Couderc et al. 2014)), and stress detection on the basis of heart rate variability (HRV) and pulse transit time (PTT) (e.g., (Chen et al. 2000; Poon and Zhang 2005; Zheng et al. 2013)). In this work, we have demonstrated that it is possible to detect acute stress in a non-contact manner based on remote HRV-driven features and differential pulse transit time (dPTT). The main novelty of our research is that, to the best of our knowledge, this is the first study demonstrating that the variability analysis of cardiac pulse acquired in the visible spectrum can be used for remote stress detection. In order to do so, it was necessary to develop a pipeline of

image and signal processing methods. Therefore, novel contribution was in the development of methods for noise-robust RR-interval extraction, stress detection based on remote HRV-driven features, dPTT measurements based on the difference in arrival of a BW signal at two distal body locations, and stress detection based on dPTT.

The HRV-driven features were acquired from the remotely detected BW signals based on minor intensity fluctuations in facial skin videos. The dPTT measurements were acquired as a difference in arrival time of a BW signal at two distal body locations (forehead and palm) within small ROIs. Generating reliable HRV-driven features and dPTT posed challenges, mainly due to the low SNR of BW signals, different pathways, and multiplicative noise. To overcome these challenges, we designed novel algorithms to reliably detect BW signals, HRV-driven features, and dPTT. In addition, we studied the effects of multiplicative noise introduced by respiration motion and light flickering on BW signals, HRV-driven features, and dPTT.

Remote HRV-driven features required accurate cycle timings of BW signals. Algorithms targeted to determine BW signals with accurate timing required special consideration such as noise removal employing principal component analysis (PCA) and peak detection using blind deconvolution (BDC). We took several steps to accomplish this. First, instead of averaging over a large ROI, we applied PCA to minimize pulse broadening due to phase dispersion, and then, instead of applying a bandpass filter, we applied ICA to determine a BW signal. It was challenging to determine accurate peak locations from the resultant BW signals that still had multiple peaks in each cycle. We solved this challenge by applying BDC algorithm to estimate impulse train as an input to

the human body (transfer function) which after passing through resulted in a given BW signal (output).

Our novel algorithms helped with detecting peaks that were in close proximity to the ECG R-peak locations, with the average normal error of 3.93% and a standard deviation of the normal error of 2.63%. Our methods not only helped with detecting signal peaks with high accuracy, but also helped in estimating subject-specific system responses to their heartbeat signals. The individualized system identification (subject-specific system response) aspect of the developed method can potentially be further studied to understand a human body's system response for various inputs (e.g., respiration), physical (e.g., cough, cold, fever, etc.), and physiological (e.g., happy, sad, etc.) conditions.

Furthermore, we studied the effects of skin locations, skin colors, and multiplicative noise introduced by respiration motion and light flickering on BW signals. Based on our studies, we found that the BW signal SNR values were much lower for the skins with high melanin contents, and that BW signals acquired from the forehead and the palm skin areas have relatively high SNR values as compared to the other visible skin areas. Moreover, our Monte Carlo based sensitivity analysis showed minimal effect of the multiplicative noise on a BW signal's peak locations ($< 1\text{ms}$) and fundamental frequency ($< 0.1\%$).

Further, the BDC algorithm-detected BW signal peaks helped with generating cleaner RR-interval signals, which is the first step for HRV analysis [1]. These RR-intervals generated from the video recordings collected under the two physiological states were used to determine remote HRV-driven features. We demonstrated that at least two

HRV-driven features that were significantly different under the two physiological states were also robust under the effects of multiplicative noise, specifically from respiration motion and light flickering. The identified robust and relevant HRV-driven features were pLF and nHF. Although group analysis is not an optimal solution to the individualized stress detection cases, we demonstrated that remote stress detection using a visible spectrum based camera is possible. Using an LR classifier at a sensitivity level of 90% we were able to achieve specificity, precision, and accuracy of above 82% for the high stress state, and 62% for the mild stress state. Additionally, a likelihood of being correct for stress detection was noted to be above 92% for both high and mild stress levels. We have, for the first time, demonstrated that it is possible to use HRV analysis of remotely detected HR information for physiological stress detection.

A further contribution of this PhD work is the development of a methodology to remotely estimate the differential pulse transit time (dPTT). We defined dPTT as the difference in time of arrival of the BW between two distal body locations. While simple in concept, implementing this measurement was a challenge due to local variations in the time of arrival of the BW, especially in the palm that was chosen as one of our target body areas. Developing a reliable protocol for this measurement involved developing guidelines for choosing small target regions of interest that show sufficient SNR, but also are easy to target in a reproducible fashion; and examining the robustness of our results in the presence of multiplicative noise, introduced either by respiration motion or light flickering. To the best of our knowledge, this is the first time a pulse transit time related metric is measured

in a contactless manner. As a proof of principle, we demonstrated that dPTT changes in response to stressful stimuli.

Since the physiological response decreases due to habituation when a stressor is introduced multiple times, the HRV-driven features and the dPTT from the two physiological states show a significant difference. We noticed this effect in our HRV and dPTT based stress detection studies. In case of HRV based stress detection, the AUC for the mild stress level case (case 2) was noticed to be less than the high stress level case (case 1). In the case of dPTT analysis for stress detection, as compared to the second or third level of stress cases, the dPTT values from the first normal state were significantly different from the first stress state (p-value <0.05).

Despite various challenges, we were able to demonstrate that the HRV and dPTT based analysis of a video-based determination of BW signals can be used for remote stress detection. While further research is needed to improve both acquisition and data processing strategies, we believe that our study shows the potential of a non-contact, possibly covert system for acute stress detection for various medical and security applications.

Impact of Dissertation

Our remote stress detection method will be valuable for many applications for stress detection in a quantifiable manner, without a potential of introducing additional stress due to contact sensors, such as: in the medical field it would help identify stressors in patients with anxiety disorders, supporting diagnosis and treatment; in the security field it could be

the basis of fraud detection; in military applications it could be used for evaluating performance of soldiers during training. The proposed remote stress detection based on visible spectrum recordings enables a solution through the use of a standard day camera which is easy to use, inexpensive, non-invasive, light weight, and accessible.

In addition, these developed methods for remote BW signal detection and peak detection, which are designed for visible spectrum based videos, can potentially be adapted for estimating cardiac or respiration signals from thermal videos (e.g., long-wave infrared (LWIR), mid-wave infrared (MWIR), short-wave infrared (SWIR)).

Since our method for stress detection compares the variability features from time-resolved signals (BW) from two physiological states (normal and stress), the developed algorithms can be applicable to a variety of change detection problems such as wounded-warrior triage, traumatic brain injury (TBI)/ post-traumatic stress disorder (PTSD) diagnosis and therapy, remote triage, long-term monitoring, etc.

Future Research Areas

In order to advance the field of remote physiological human signatures detection, investigation in following research areas would be beneficial:

1. Adapt these developed methodologies and apply them to detect cardiac pulse signals using other sensor modalities (e.g., thermal, LDV, radar).
2. Apply these developed methodologies to numerous applications such as “live or dead” determination on the battlefield or in emergency rescue operations.

3. Using videos from a monochrome digital camera with a single band (green filter), study the limitation of spatial resolution on the SNR of a BW signal.
4. Study the effects of human subject motion (e.g., fidgeting, random motions, etc.) on BW signals, and explore auto-tracking methods and implementation.
5. Study the effects of sensor parameters on the SNR of a BW signal (e.g., focal length, f-number, pixel size, etc.).
6. Study the scope of a real-time stress detection system by merging the research conducted in the areas of stressor detection in ECG recordings (Rafael, 2015) with the remote stress detection in visible spectrum.

Final Remarks

We have provided a proof of principle for a non-contact stress detection system based on variability in remotely acquired BW signals. This system includes one visible camera and a computer system with image processing algorithms for BW signal detection and classification for the stress detection based on variations in BW signals. This video-based stress detection system should help with overcoming the additional (potential) stress introduced by contact sensors, and therefore, should provide a discrete means of monitoring stress in individuals. In addition to facilitating repeatable and reliable measurements for a stimulus response, the developed system provides a potential solution for covert measurements under controlled environment and daylight conditions for many medical and security applications.

REFERENCES

- [1] B. Kaur, S. Moses, M. Luthra, and V. N. Ikonomidou, "Remote stress detection using a visible spectrum camera," in *SPIE Sensing Technology+ Applications*, 2015, pp. 949602–949602.
- [2] J. M. Irvine, B. K. Wiederhold, L. W. Gavshon, S. A. Israel, S. B. McGehee, R. Meyer, and M. D. Wiederhold, "Heart rate variability: a new biometric for human identification," in *Proceedings of the International Conference on Artificial Intelligence (IC-AI'01)*, 2001, pp. 1106–1111.
- [3] M. Sung and A. P. Pentland, "PokerMetrics: Stress and lie detection through non-invasive physiological sensing," Ph. D. thesis, MIT Media Laboratory, 2005.
- [4] G. G. Berntson and J. T. Cacioppo, "Heart Rate Variability: Stress and Psychiatric Conditions," in *Dynamic Electrocardiography*, reklik Ms. FESCessor , MD, DSc, DSc (Med), FACC and A. J. C. Q. CStJessor BSc, MD, FRCP, FESC, FACC, FAHA, FCGC, Eds. Blackwell Publishing, 2004, pp. 57–64.
- [5] S. Boonnithi and S. Phongsuphap, "Comparison of heart rate variability measures for mental stress detection," in *Computing in Cardiology, 2011*, 2011, pp. 85–88.
- [6] S. A. Israel, J. M. Irvine, B. K. Wiederhold, and M. D. Wiederhold, "The Heartbeat: The Living Biometric," in *Biometrics*, N. V. Boulgouris, K. N. Plataniotis, and E. Micheli-Tzanakou, Eds. John Wiley & Sons, Inc., 2009, pp. 429–459.
- [7] Y. Zheng, B. P. Yan, Y. Zhang, C. M. Yu, and C. C. Y. Poon, "Wearable cuff-less PTT-based system for overnight blood pressure monitoring," *Conf. Proc. Annu. Int. Conf. IEEE Eng. Med. Biol. Soc. IEEE Eng. Med. Biol. Soc. Annu. Conf.*, vol. 2013, pp. 6103–6106, 2013.
- [8] E. Gil, R. Bailón, J. M. Vergara, and P. Laguna, "PTT variability for discrimination of sleep apnea related decreases in the amplitude fluctuations of PPG signal in children," *Biomed. Eng. IEEE Trans. On*, vol. 57, no. 5, pp. 1079–1088, 2010.
- [9] C. C. Y. Poon and Y. T. Zhang, "Cuff-less and Noninvasive Measurements of Arterial Blood Pressure by Pulse Transit Time," in *Engineering in Medicine and Biology Society, 2005. IEEE-EMBS 2005. 27th Annual International Conference of the*, 2005, pp. 5877–5880.

- [10] B. Kaur, E. Tarbox, M. Cissel, S. Moses, M. Luthra, M. Vaidya, N. Tran, and V. N. Ikonomidou, "Remotely detected differential pulse transit time as a stress indicator," in *SPIE Sensing Technology+ Applications*, 2015, pp. 949604–949604.
- [11] H. Hotelling, "Analysis of a complex of statistical variables into principal components.," *J. Educ. Psychol.*, vol. 24, no. 6, p. 417, 1933.
- [12] J. Shlens, "A tutorial on principal component analysis," *ArXiv Prepr. ArXiv14041100*, 2014.
- [13] A. Hyvärinen and E. Oja, "Independent component analysis: algorithms and applications," *Neural Netw.*, vol. 13, no. 4, pp. 411–430, 2000.
- [14] J. de Rooi and P. Eilers, "Deconvolution of pulse trains with the L 0 penalty," *Anal. Chim. Acta*, vol. 705, no. 1, pp. 218–226, 2011.
- [15] J. A. Levine, I. T. Pavlidis, L. MacBride, Z. Zhu, and P. Tsiamyrtzis, "Description and clinical studies of a device for the instantaneous detection of office-place stress," *Work*, vol. 34, no. 3, p. 359, 2009.
- [16] J. Healey, R. W. Picard, and others, "Detecting stress during real-world driving tasks using physiological sensors," *Intell. Transp. Syst. IEEE Trans. On*, vol. 6, no. 2, pp. 156–166, 2005.
- [17] R. Misslin, "The defense system of fear: behavior and neurocircuitry," *Neurophysiol. Clin. Neurophysiol.*, vol. 33, no. 2, pp. 55–66, 2003.
- [18] G. E. Prinsloo, H. G. Rauch, and W. E. Derman, "A brief review and clinical application of heart rate variability biofeedback in sports, exercise, and rehabilitation medicine.," *Phys. Sportsmed.*, vol. 42, no. 2, pp. 88–99, 2014.
- [19] B. Kaur, J. J. Durek, B. L. O’Kane, N. Tran, S. Moses, M. Luthra, and V. N. Ikonomidou, "Heart rate variability (HRV): an indicator of stress," in *SPIE Sensing Technology+ Applications*, 2014, p. 91180V–91180V.
- [20] A. Gaggioli, P. Cipresso, S. Serino, D. M. Campanaro, F. Pallavicini, B. K. Wiederhold, and G. Riva, "Positive technology: a free mobile platform for the self-management of psychological stress.," *Stud. Health Technol. Inform.*, vol. 199, pp. 25–29, 2013.
- [21] J. Saalfield and L. Spear, "Developmental differences in the effects of alcohol and stress on heart rate variability," *Physiol. Behav.*, 2014.
- [22] A. Elfering and S. Grebner, "Ambulatory assessment of skin conductivity during first thesis presentation: lower self-confidence predicts prolonged stress response," *Appl. Psychophysiol. Biofeedback*, vol. 36, no. 2, pp. 93–99, Jun. 2011.
- [23] M. Ohmi, M. Tanigawa, Y. Wada, and M. Haruna, "Dynamic analysis for mental sweating of a group of eccrine sweat glands on a human fingertip by optical coherence tomography," *Skin Res. Technol.*, vol. 18, no. 3, pp. 378–383, 2012.

- [24] G. V. Krishnaveni, S. R. Veena, A. Jones, D. S. Bhat, M. P. Malathi, D. Hellhammer, K. Srinivasan, H. Upadya, A. V. Kurpad, and C. H. D. Fall, "Trier social stress test in Indian adolescents," *Indian Pediatr.*, vol. 51, no. 6, pp. 463–467, 2014.
- [25] J. L. Kibler, M. Tursich, M. Ma, L. Malcolm, and R. Greenberg, "Metabolic, autonomic and immune markers for cardiovascular disease in posttraumatic stress disorder," *World J. Cardiol.*, vol. 6, no. 6, p. 455, 2014.
- [26] M. T. Hicken, J. T. Dvovich, A. J. Schulz, G. Mentz, and P. Max, "Fine particulate matter air pollution and blood pressure: The modifying role of psychosocial stress," *Environ. Res.*, vol. 133, pp. 195–203, 2014.
- [27] P. Albert, K. G. Rice, and L. Caffee, "Perfectionism Affects Blood Pressure in Response to Repeated Exposure to Stress," *Stress Health*, 2014.
- [28] A. H. Lewis, A. J. Porcelli, and M. R. Delgado, "The effects of acute stress exposure on striatal activity during Pavlovian conditioning with monetary gains and losses," *Front. Behav. Neurosci.*, vol. 8, 2014.
- [29] C. L. Burton, G. A. Bonanno, and M. L. Hatzenbuehler, "Familial social support predicts a reduced cortisol response to stress in sexual minority young adults," *Psychoneuroendocrinology*, vol. 47, pp. 241–245, Sep. 2014.
- [30] G. Mura, G. Cossu, G. M. Migliaccio, C. Atzori, A. E. Nardi, S. Machado, and M. G. Carta, "Quality of Life, Cortisol Blood Levels and Exercise in Older Adults: Results of a Randomized Controlled Trial," *Clin. Pract. Epidemiol. Ment. Health CP EMH*, vol. 10, p. 67, 2014.
- [31] D. Kim, Y. Seo, and L. Salahudin, "Decreased circadian variations of heart rate variability in subjects with higher self reporting stress scores," *Pervasive Heal. Tamp. Finl.*, 2008.
- [32] X. Xu and Y. Liu, "ECG QRS complex detection using slope vector waveform (SVW) algorithm," in *Engineering in Medicine and Biology Society, 2004. IEMBS'04. 26th Annual International Conference of the IEEE*, 2004, vol. 2, pp. 3597–3600.
- [33] S.-H. Liu, C.-T. Lin, and W.-H. Chao, "The short-time fractal scaling of heart rate variability to estimate the mental stress of driver," in *2004 IEEE International Conference on Networking, Sensing and Control*, 2004, vol. 2, pp. 829–833 Vol.2.
- [34] A. Verma, S. Cabrera, A. Mayorga, and H. Nazeran, "A Robust Algorithm for Derivation of Heart Rate Variability Spectra from ECG and PPG Signals," in *Biomedical Engineering Conference (SBEC), 2013 29th Southern*, 2013, pp. 35–36.
- [35] Y. Leschyshyn, O. Semchyshyn, and V. Dozorsky, "Detection characteristics computation of nonstationarity heart rate variability by Neyman-Pearson

- criterion,” in *2008 International Conference on “ Modern Problems of Radio Engineering, Telecommunications and Computer Science”(TCSET)*, 2008.
- [36] Y. Hsu, Y.-L. Lin, and W. Hsu, “Learning-based heart rate detection from remote photoplethysmography features,” in *2014 IEEE International Conference on Acoustics, Speech and Signal Processing (ICASSP)*, 2014, pp. 4433–4437.
- [37] M.-Z. Poh, D. J. McDuff, and R. W. Picard, “Non-contact, automated cardiac pulse measurements using video imaging and blind source separation,” *Opt. Express*, vol. 18, no. 10, pp. 10762–10774, 2010.
- [38] D. McDuff, S. Gontarek, and R. W. Picard, “Improvements in Remote Cardio-Pulmonary Measurement Using a Five Band Digital Camera,” 2014.
- [39] S. Kwon, H. Kim, and K. S. Park, “Validation of heart rate extraction using video imaging on a built-in camera system of a smartphone,” in *Engineering in Medicine and Biology Society (EMBC), 2012 Annual International Conference of the IEEE*, 2012, pp. 2174–2177.
- [40] S. Lu, H. Zhao, K. Ju, K. Shin, M. Lee, K. Shelley, and K. H. Chon, “Can photoplethysmography variability serve as an alternative approach to obtain heart rate variability information?,” *J. Clin. Monit. Comput.*, vol. 22, no. 1, pp. 23–29, 2008.
- [41] L. Zhu, Y. Zhu, H. Mao, and M. Gu, “A new method for sparse signal denoising based on compressed sensing,” in *Knowledge Acquisition and Modeling, 2009. KAM’09. Second International Symposium on*, 2009, vol. 1, pp. 35–38.
- [42] H. Shaoxiang and Z. Liao, “Signal denoising using wavelet packet hidden Markov model,” in *Communications, Circuits and Systems, 2004. ICCAS 2004. 2004 International Conference on*, 2004, vol. 2, pp. 751–755.
- [43] K. A. Reddy, B. George, and V. J. Kumar, “Motion Artifact Reduction and Data Compression of Photoplethysmographic Signals utilizing Cycle by Cycle Fourier Series Analysis,” in *Instrumentation and Measurement Technology Conference Proceedings, 2008. IMTC 2008. IEEE*, 2008, pp. 176–179.
- [44] S. Durand and J. Froment, “Artifact free signal denoising with wavelets,” in *2001 IEEE International Conference on Acoustics, Speech, and Signal Processing, 2001. Proceedings. (ICASSP ’01)*, 2001, vol. 6, pp. 3685–3688 vol.6.
- [45] R. Yousefi, M. Nourani, S. Ostadabbas, and I. Panahi, “A Motion-Tolerant Adaptive Algorithm for Wearable Photoplethysmographic Biosensors,” *IEEE J. Biomed. Health Inform.*, vol. 18, no. 2, pp. 670–681, Mar. 2014.
- [46] N. Selvaraj, Y. Mendelson, K. H. Shelley, D. G. Silverman, and K. H. Chon, “Statistical approach for the detection of motion/noise artifacts in Photoplethysmogram,” in *Engineering in Medicine and Biology Society, EMBC, 2011 Annual International Conference of the IEEE*, 2011, pp. 4972–4975.

- [47] Y.-K. Lee, O.-W. Kwon, H. S. Shin, J. Jo, and Y. Lee, “Noise reduction of PPG signals using a particle filter for robust emotion recognition,” in *Consumer Electronics-Berlin (ICCE-Berlin), 2011 IEEE International Conference on*, 2011, pp. 202–205.
- [48] X. Luo, F. Miao, and Y. Li, “PPG and ECG feature comparison for healthy people and hypertensive patients,” in *Biomedical and Health Informatics (BHI), 2012 IEEE-EMBS International Conference on*, 2012, pp. 785–787.
- [49] H.-Y. Wu, M. Rubinstein, E. Shih, J. V. Guttag, F. Durand, and W. T. Freeman, “Eulerian video magnification for revealing subtle changes in the world,” *ACM Trans Graph*, vol. 31, no. 4, p. 65, 2012.
- [50] J. Choi, B. Ahmed, and R. Gutierrez-Osuna, “Development and evaluation of an ambulatory stress monitor based on wearable sensors,” *Inf. Technol. Biomed. IEEE Trans. On*, vol. 16, no. 2, pp. 279–286, 2012.
- [51] J. Choi and R. Gutierrez-Osuna, “Using Heart Rate Monitors to Detect Mental Stress,” in *Sixth International Workshop on Wearable and Implantable Body Sensor Networks, 2009. BSN 2009*, 2009, pp. 219–223.
- [52] E. D. Ubeyli, D. Cvetkovic, and I. Cosic, “Eigenvector Methods for Analysis of Human PPG, ECG and EEG Signals,” in *Engineering in Medicine and Biology Society, 2007. EMBS 2007. 29th Annual International Conference of the IEEE*, 2007, pp. 3304–3307.
- [53] C. L. Desjardins, L. T. Antonelli, and E. Soares, “A remote and non-contact method for obtaining the blood-pulse waveform with a laser Doppler vibrometer,” in *Biomedical Optics (BiOS) 2007*, 2007, p. 64301C–64301C.
- [54] K. A. Byrd, B. Kaur, and V. A. Hodgkin, “The use of spectral skin reflectivity and laser doppler vibrometry data to determine the optimal site and wavelength to collect human vital sign signatures,” 2012, p. 83820F–83820F–6.
- [55] M. Garbey, N. Sun, A. Merla, and I. Pavlidis, “Contact-free measurement of cardiac pulse based on the analysis of thermal imagery,” *IEEE Trans. Biomed. Eng.*, vol. 54, no. 8, pp. 1418–1426, Aug. 2007.
- [56] P. Pelegris, K. Banitsas, T. Orbach, and K. Marias, “A novel method to detect heart beat rate using a mobile phone,” in *Engineering in Medicine and Biology Society (EMBC), 2010 Annual International Conference of the IEEE*, 2010, pp. 5488–5491.
- [57] B. Kaur, V. A. Hodgkin, J. K. Nelson, V. N. Ikonomidou, and J. A. Hutchinson, “Hyperspectral waveband group optimization for time-resolved human sensing,” in *SPIE Defense, Security, and Sensing*, 2013, p. 87500J–87500J.
- [58] A. A. R. Kamal, J. B. Harness, G. Irving, and A. J. Mearns, “Skin photoplethysmography — a review,” *Comput. Methods Programs Biomed.*, vol. 28, no. 4, pp. 257–269, Apr. 1989.

- [59] W. K. Purves, G. H. Orians, D. Sadava, and H. C. Heller, *Life: The Science of Biology: Volume III: Plants and Animals*, vol. 3. Macmillan, 2003.
- [60] F.-K. Wang, T.-S. Horng, K.-C. Peng, J.-K. Jau, J.-Y. Li, and C.-C. Chen, "Detection of Concealed Individuals Based on Their Vital Signs by Using a See-Through-Wall Imaging System With a Self-Injection-Locked Radar," *IEEE Trans. Microw. Theory Tech.*, vol. 61, no. 1, pp. 696–704, Jan. 2013.
- [61] S. Winkler, M. Schieber, S. Lücke, P. Heinze, T. Schweizer, D. Wegertseder, M. Scherf, H. Nettelau, S. Henke, M. Braecklein, and others, "A new telemonitoring system intended for chronic heart failure patients using mobile telephone technology—feasibility study," *Int. J. Cardiol.*, vol. 153, no. 1, pp. 55–58, 2011.
- [62] C. G. Scully, J. Lee, J. Meyer, A. M. Gorbach, D. Granquist-Fraser, Y. Mendelson, and K. H. Chon, "Physiological parameter monitoring from optical recordings with a mobile phone," *Biomed. Eng. IEEE Trans. On*, vol. 59, no. 2, pp. 303–306, 2012.
- [63] M.-Z. Poh, D. J. McDuff, and R. W. Picard, "Advancements in noncontact, multiparameter physiological measurements using a webcam," *IEEE Trans. Biomed. Eng.*, vol. 58, no. 1, pp. 7–11, Jan. 2011.
- [64] A. Sahoo, P. Manimegalai, and K. Thanushkodi, "Wavelet based pulse rate and Blood pressure estimation system from ECG and PPG signals," in *Computer, Communication and Electrical Technology (ICCCET), 2011 International Conference on*, 2011, pp. 285–289.
- [65] B. R. TEJA, "Calculation of Blood Pulse Transit Time from PPG," National Institute of Technology, Rourkela, 2012.
- [66] L. A. Geddes, M. H. Voelz, C. F. Babbs, J. D. Bourland, and W. A. Tacker, "Pulse Transit Time as an Indicator of Arterial Blood Pressure," *Psychophysiology*, vol. 18, no. 1, pp. 71–74, 1981.
- [67] P. A. Obrist, K. C. Light, J. A. McCubbin, J. S. Hutcheson, and J. L. Hoffer, "Pulse Transit Time: Relationship to Blood Pressure and Myocardial Performance," *Psychophysiology*, vol. 16, no. 3, pp. 292–301, 1979.
- [68] H. Gesche, D. Grosskurth, G. Küchler, and A. Patzak, "Continuous blood pressure measurement by using the pulse transit time: comparison to a cuff-based method," *Eur. J. Appl. Physiol.*, vol. 112, no. 1, pp. 309–315, Jan. 2012.
- [69] A. Hennig and P. D. A. Patzak, "Continuous blood pressure measurement using pulse transit time," *Somnologie - Schlafforschung Schlafmed.*, vol. 17, no. 2, pp. 104–110, Jun. 2013.
- [70] I. cheol Jeong and J. Finkelstein, "Potential value of electrocardiogram and photoplethysmogram for non-invasive blood pressure estimation during exercise," *Conf. Proc. Annu. Int. Conf. IEEE Eng. Med. Biol. Soc. IEEE Eng. Med. Biol. Soc. Annu. Conf.*, vol. 2013, pp. 2304–2307, 2013.

- [71] B. Gribbin, A. Steptoe, and P. Sleight, "Pulse Wave Velocity as a Measure of Blood Pressure Change," *Psychophysiology*, vol. 13, no. 1, pp. 86–90, Jan. 1976.
- [72] A. Steptoe, H. Smulyan, and B. Gribbin, "Pulse Wave Velocity and Blood Pressure Change: Calibration and Applications," *Psychophysiology*, vol. 13, no. 5, pp. 488–493, Sep. 1976.
- [73] R. a. Allen, J. A. Schneider, D. M. Davidson, M. A. Winchester, and C. B. Taylor, "The Covariation of Blood Pressure and Pulse Transit Time in Hypertensive Patients," *Psychophysiology*, vol. 18, no. 3, pp. 301–306, May 1981.
- [74] H. Schmalgemeier, T. Bitter, S. Bartsch, K. Bullert, T. Fischbach, S. Eckert, D. Horstkotte, and O. Oldenburg, "Pulse transit time: validation of blood pressure measurement under positive airway pressure ventilation," *Sleep Breath. Schlaf Atm.*, vol. 16, no. 4, pp. 1105–1112, Dec. 2012.
- [75] S.-H. Kim, J.-G. Song, J.-H. Park, J.-W. Kim, Y.-S. Park, and G.-S. Hwang, "Beat-to-beat tracking of systolic blood pressure using noninvasive pulse transit time during anesthesia induction in hypertensive patients," *Anesth. Analg.*, vol. 116, no. 1, pp. 94–100, Jan. 2013.
- [76] J. Lass, K. Meigas, D. Karai, R. Kattai, J. Kaik, and M. Rossmann, "Continuous blood pressure monitoring during exercise using pulse wave transit time measurement," *Conf. Proc. Annu. Int. Conf. IEEE Eng. Med. Biol. Soc. IEEE Eng. Med. Biol. Soc. Annu. Conf.*, vol. 3, pp. 2239–2242, 2004.
- [77] Y.-L. Zheng, B. P. Yan, Y.-T. Zhang, and C. C. Y. Poon, "An armband wearable device for overnight and cuff-less blood pressure measurement," *IEEE Trans. Biomed. Eng.*, vol. 61, no. 7, pp. 2179–2186, Jul. 2014.
- [78] P. J. Nestel, "BLOOD-PRESSURE AND CATECHOLAMINE EXCRETION AFTER MENTAL STRESS IN LABILE HYPERTENSION," *The Lancet*, vol. 293, no. 7597, pp. 692–694, Apr. 1969.
- [79] N. Hjortskov, D. Rissén, A. K. Blangsted, N. Fallentin, U. Lundberg, and K. Sjøgaard, "The effect of mental stress on heart rate variability and blood pressure during computer work," *Eur. J. Appl. Physiol.*, vol. 92, no. 1–2, pp. 84–89, Feb. 2004.
- [80] Z. Zhao, W.-H. Lin, P. Yang, and Y.-T. Zhang, "Spectral and coherence analysis of the variabilities of heart rate, stroke volume, and systolic blood pressure in exercise stress tests," in *Biomedical and Health Informatics (BHI), 2012 IEEE-EMBS International Conference on*, 2012, pp. 771–774.
- [81] Q. Liu, C. C. Y. Poon, and Y. T. Zhang, "Time–frequency analysis of variabilities of heart rate, systolic blood pressure and pulse transit time before and after exercise using the recursive autoregressive model," *Biomed. Signal Process. Control*, vol. 6, no. 4, pp. 364–369, 2011.

- [82] H. T. Ma and Y. T. Zhang, "Spectral analysis of pulse transit time variability and its coherence with other cardiovascular variabilities," in *Engineering in Medicine and Biology Society, 2006. EMBS'06. 28th Annual International Conference of the IEEE*, 2006, pp. 6442–6445.
- [83] L. Wang, C. C. Y. Poon, and Y. T. Zhang, "The non-invasive and continuous estimation of cardiac output using a photoplethysmogram and electrocardiogram during incremental exercise," *Physiol. Meas.*, vol. 31, no. 5, p. 715, 2010.
- [84] F. Bousefsaf, C. Maaoui, and A. Pruski, "Remote assessment of the heart rate variability to detect mental stress," in *2013 7th International Conference on Pervasive Computing Technologies for Healthcare (PervasiveHealth)*, 2013, pp. 348–351.
- [85] P. Yuen, K. Hong, T. Chen, A. Tsitiridis, F. Kam, J. Jackman, D. James, M. Richardson, L. Williams, W. Oxford, and others, "Emotional & physical stress detection and classification using thermal imaging technique," 2009.
- [86] F. Mokhayeri, M.-R. Akbarzadeh-T, and S. Toosizadeh, "Mental stress detection using physiological signals based on soft computing techniques," in *Biomedical Engineering (ICBME), 2011 18th Iranian Conference of*, 2011, pp. 232–237.
- [87] P. Ren, A. Barreto, Y. Gao, and M. Adjouadi, "Affective assessment by digital processing of the pupil diameter," *Affect. Comput. IEEE Trans. On*, vol. 4, no. 1, pp. 2–14, 2013.
- [88] M. Soury and L. Devillers, "Stress detection from audio on multiple window analysis size in a public speaking task," in *Affective Computing and Intelligent Interaction (ACII), 2013 Humaine Association Conference on*, 2013, pp. 529–533.
- [89] A. J. Weir, R. Sayer, C.-X. Wang, and S. Parks, "A wall-less poly (vinyl alcohol) cryogel flow phantom with accurate scattering properties for transcranial Doppler ultrasound propagation channels analysis," in *Engineering in Medicine and Biology Society (EMBC), 2015 37th Annual International Conference of the IEEE*, 2015, pp. 2709–2712.
- [90] R. T. Hocter, A. M. Dentinger, and K. E. Thomenius, "Array signal processing approaches to ultrasound-based arterial pulse wave velocity estimation," in *Acoustics, Speech, and Signal Processing, 2005. Proceedings.(ICASSP'05). IEEE International Conference on*, 2005, vol. 5, pp. v–985.
- [91] G. M. London and A. P. Guerin, "Influence of arterial pulse and reflected waves on blood pressure and cardiac function," *Am. Heart J.*, vol. 138, no. 3, pp. S220–S224, 1999.
- [92] G. F. Mitchell, H. Parise, E. J. Benjamin, M. G. Larson, M. J. Keyes, J. A. Vita, R. S. Vasan, and D. Levy, "Changes in arterial stiffness and wave reflection with advancing age in healthy men and women the Framingham Heart Study," *Hypertension*, vol. 43, no. 6, pp. 1239–1245, 2004.

- [93] T. F. Antonios, F. E. Rattray, D. R. Singer, N. D. Markandu, P. S. Mortimer, and G. A. MacGregor, "Maximization of skin capillaries during intravital video-microscopy in essential hypertension: comparison between venous congestion, reactive hyperaemia and core heat load tests," *Clin. Sci. Lond. Engl.* 1979, vol. 97, no. 4, pp. 523–528, Oct. 1999.
- [94] P. G. H. Golub and D. C. Reinsch, "Singular value decomposition and least squares solutions," *Numer. Math.*, vol. 14, no. 5, pp. 403–420, Apr. 1970.
- [95] V. Klema and A. J. Laub, "The singular value decomposition: Its computation and some applications," *Autom. Control IEEE Trans. On*, vol. 25, no. 2, pp. 164–176, 1980.
- [96] A.-J. Van Der Veen, E. F. Deprettere, and A. L. Swindlehurst, "Subspace-based signal analysis using singular value decomposition," *Proc. IEEE*, vol. 81, no. 9, pp. 1277–1308, 1993.
- [97] K. Dabov, A. Foi, V. Katkovnik, and K. Egiazarian, "BM3D Image Denoising with Shape-Adaptive Principal Component Analysis," in *PROC. WORKSHOP ON SIGNAL PROCESSING WITH ADAPTIVE SPARSE STRUCTURED REPRESENTATIONS (SPARS'09)*, 2009.
- [98] T.-W. Lee, *Independent component analysis*. Springer, 1998.
- [99] J. V. Stone, *Independent component analysis*. Wiley Online Library, 2004.
- [100] D. D. Lee and H. S. Seung, "Learning the parts of objects by non-negative matrix factorization," *Nature*, vol. 401, no. 6755, pp. 788–791, 1999.
- [101] P. Comon, "Independent component analysis, a new concept?," *Signal Process.*, vol. 36, no. 3, pp. 287–314, 1994.
- [102] B. Widrow and S. D. Stearns, "Adaptive signal processing," *Englewood Cliffs NJ Prentice-Hall Inc 1985 491 P*, vol. 1, 1985.
- [103] J. Pan and W. J. Tompkins, "A Real-Time QRS Detection Algorithm," *IEEE Trans. Biomed. Eng.*, vol. BME-32, no. 3, pp. 230–236, Mar. 1985.
- [104] K. S. Bersha, "Spectral imaging and analysis of human skin," Master thesis report. University of Eastern Finland, 2010.
- [105] V. A. Hodgkin, B. Kaur, and K. A. Byrd, "Skin Reflectivity as a Target Signature," in *Military Sensing Symposium Parallel*, 2012.
- [106] J. T. Ramshur, "Design, evaluation, and application of heart rate variability software (HRVAS)," Master's thesis, The University of Memphis, Memphis, TN, 2010.
- [107] G. M. Friesen, T. C. Jannett, M. A. Jadallah, S. L. Yates, S. R. Quint, and H. T. Nagle, "A comparison of the noise sensitivity of nine QRS detection algorithms," *IEEE Trans. Biomed. Eng.*, vol. 37, no. 1, pp. 85–98, Jan. 1990.

- [108] A. Rao, Y. Lee, A. Gass, and A. Monsch, "Classification of Alzheimer's Disease from structural MRI using sparse logistic regression with optional spatial regularization," in *Engineering in Medicine and Biology Society, EMBC, 2011 Annual International Conference of the IEEE*, 2011, pp. 4499–4502.
- [109] R. O. Duda, P. E. Hart, and D. G. Stork, *Pattern Classification*, 2 edition. New York: Wiley-Interscience, 2000.
- [110] A. Elisseeff, M. Pontil, and others, "Leave-one-out error and stability of learning algorithms with applications," *NATO Sci. Ser. Sub Ser. Iii Comput. Syst. Sci.*, vol. 190, pp. 111–130, 2003.
- [111] S. Boonnithi and S. Phongsuphap, "Comparison of heart rate variability measures for mental stress detection," in *Computing in Cardiology, 2011*, 2011, pp. 85–88.
- [112] D. R. King, M. P. Ogilvie, B. M. Pereira, Y. Chang, R. J. Manning, J. A. Conner, C. I. Schulman, M. G. McKenney, and K. G. Proctor, "Heart rate variability as a triage tool in patients with trauma during prehospital helicopter transport," *J. Trauma Acute Care Surg.*, vol. 67, no. 3, pp. 436–440, 2009.
- [113] P. Manimegalai, D. Jacob, and K. Thanushkodi, "Estimation of cardiovascular parameters from ECG and PPG signals," in *Bioengineering Conference (NEBEC), 2012 38th Annual Northeast*, 2012, pp. 237–238.
- [114] S. Bang, C. Lee, J. Park, M.-C. Cho, Y.-G. Yoon, and S. Cho, "A pulse transit time measurement method based on electrocardiography and bioimpedance," in *Biomedical Circuits and Systems Conference, 2009. BioCAS 2009. IEEE*, 2009, pp. 153–156.
- [115] L. P. Frater and N. R. Watson, "Light flicker sensitivity of high efficiency compact fluorescent lamps," in *Power Engineering Conference, 2007. AUPEC 2007. Australasian Universities*, 2007, pp. 1–6.
- [116] R. C. Gonzalez, R. E. Woods, and S. L. Eddins, *Digital image processing using MATLAB*. Pearson Education India, 2004.
- [117] O. Baran, M. Kasal, P. Vagner, and T. Urbanec, "Modeling of the phase noise influence in the general M-PSK system," in *2011 5th International Conference on Recent Advances in Space Technologies (RAST)*, 2011, pp. 393–398.

BIOGRAPHY

Balvinder Kaur earned her Bachelor's degree in Electrical Engineering in 1999 from George Mason University (GMU). She worked as an electrical engineer in the defense industry, advancing to her current position at the US Army Night Vision and Electronic Sensors Directorate in 2010. There she researched in the areas of signal/image processing for static and dynamic target detection, recognition, classification, and tracking, and earned her Master's and Doctorate degrees in Electrical Engineering in 2012 and 2016 respectively from GMU to further her research in these areas. She wishes to continue working as a research scientist and contribute to remote sensing and related applications.